Optimum damping of beam vibrations using piezoceramic transducers

Marco Rufinelli

Thesis submitted to the Faculty of the
Virginia Polytechnic Institute and State University
in partial fulfillment of the requirements for the degree of

Master of Science
in
Engineering Mechanics

Romesh C. Batra, Chair
Scott W. Case
Mark Stremler

April 30, 2002
Blacksburg, Virginia

Keywords: Piezoelectric Transducers, Vibrations Control, Piezo-electromechanical coupling, Frequency response function, Modal Testing

Optimum damping of beam vibrations using piezoceramic transducers

Marco Rufinelli

(ABSTRACT)

In this thesis a piezo-electro-mechanical system, constituted of an aluminum beam with five piezoelectric patches glued on it, each of them shunted with an RL electrical circuit, has been numerically and experimentally investigated, in order to determine the optimal electric tuning parameters for vibration damping. A numerical code based upon Galerkin weighted-residual method is developed and the complete piezo-electro-mechanical system is designed, realized and finally tested by a standard modal testing technique. Comparisons between different shunting configurations of the system are given and finally the experimental data are compared with ones obtained by the developed numerical code in order to verify the accuracy of the latter.

To ...my mother and my father.

Contents

List of Figures

List of Tables

Chapter 1

Introduction

It has been more than a century since the discovery of the piezoelectric effect by Pierre and Jaques Curie in 1880. Piezoelectricity is a phenomenon in which certain crystalline substances develop an electric field when subjected to a pressure force, or, conversely, exhibit a mechanical deformation when subjected to an electric field. This reciprocal coupling between mechanical and electrical energy renders piezoelectric materials useful in many applications.

The existence of this effect has been proven in many materials. Only very few, however, have been found suitable for practical applications. Lead-Zirconate-Titanate, usually abbreviated as PZT, is one of the most commonly used piezoelectric ceramics. In addition to its piezoelectric characteristics, PZT exhibits excellent properties under normal working conditions, such as a large range of linearity in piezoelectric effect, long-term temperature stability, and low internal friction loss coefficient. In the manufacture of piezoceramics, a suitable dielectric material is fabricated into the desired shape, and electrodes are applied. The piezoceramic element is then heated to an elevated temperature while in the presence of a strong DC electric field. This polarizes or "poles" the ceramic (aligns the molecular dipoles of the ceramic in the direction of the applied field) and provides it with piezoelectric properties.

Because of its distinct characteristics, PZT ceramics have been widely employed in many scientific and engineering fields for both sensors and actuators, in order to develop adaptive structures or intelligent material systems. Such systems can integrate intelligence into the microstructure of the system to produce adaptive functionality [2]. The emergence of intelligent material systems represents a novel and exciting technology in an interdisciplinary scientific and engineering field involving mathematics, materials, mechanics, dynamics, acoustics, and controls. Research in this area has already produced many prominent applications, such as vibration and acoustic control [4],[3],[5], motion control [6], shape alteration[7], non-destructive evaluation[8][9], failure prevention, and system identification[10].

From the stand point of the system architecture, an adaptive structure is an integration of

host structures (beams, trusses, plates, shells, and complex structures) with guest components (actuators, sensors, and controllers). One of the most important elements in adaptive structures is an actuator, which acts like muscles in a biological system to provide energy input. An actuator is classified as an induced strain actuator if it produces strains in response to external stimuli such as electricity, magnetism, heat actuation, etc. The induced strain actuators can be flexibly fabricated with conventional engineering materials to form unified composite structures. This may be one of the most convincing reasons for the induced strain actuators to be more favored than conventional "point" actuators (shakers etc.) in various applications. The induced strain actuators can be surface-bonded, embedded, or attached to the host structures. Such actuators thus provide a powerful means to realize flexible control strategies and to tune the structural response.

The most commonly used induced strain actuators include piezoelectric actuators (PZT and PVDF), magnetostrictive actuators (Terfenol-D), electrostrictive actuators (PMN) and thermomechanical actuators (shape memory alloys). Among them, piezoelectric (PZT) elements have become increasingly important because piezoelectric elements have demonstrated competitive characteristics such as light weight, compact size, and good dynamic output performance. In addition, the ability of piezoelectric materials to transform mechanical energy to electrical energy and vice-versa makes them well suited to be both actuators and sensors

This thesis will focus on the control of structural vibration by means of PZT actuators. In the last decade many research efforts were devoted to this field, encouraged by significant electromechanical coupling offered by the new generation of piezoelectric ceramics. In this context active and passive techniques have been developed. Active controls use PZT materials as sensors and actuators to apply a feedback control to the structure. They achieve good performance, but they present the disadvantage of high power requirement, stability problems, and the need of a complex central unit for the implementation of the control law. Passive solution suggests the use of piezoelectromechanical coupling to transfer mechanical energy into electrical form and then dissipate it in resistors by the Joule effect.

It has been show that resonant systems are more effective for controling structural vibrations. In analogy to Dynamic Vibration Absorbers ($DVAs$) piezoelectric transducers shunted on an inductance and a resistance can be bonded to a structure to form a coupled, highly dissipative system. Adjusting the electrical parameters, the RLC (resistor (R), inductor (L), and capacitor (C)) circuit can be tuned to a given mechanical mode, thus replacing it with a pair of strongly damped electromechanical modes. This solution with respect to the active ones, presents advantages of construction simplicity, intrinsic stability and total independence from the environment. Indeed, in principle, passive devices not only do not require power to work, but they can even be used to produce small amounts of energy. In practice, the high inductance required to lower the electrical frequencies to the range of mechanical ones are frequently synthesized with an electronic circuit that requires a small amount of power to work. Resonant Shunted Piezoelectrics ($RSPs$) are strongly preferable to the mechanical analog $DVAs$ because of their low cost, low weight, low space requirements and flexibility. In fact, the electrical parameters can be easily adjusted to match characteristics of the

structural mode to be damped. Exploiting this aspect, semi-active systems in which values of the electrical parameters are chosen by a real-time control unit have also been proposed. Industrial applications of $RSPs$ are now available (see, for example, *www.acx.com* where smart skis and smart bikes are illustrated). The greatest disadvantage of these devices is that they are effective only in a narrow band of frequencies because of their one-degree-of-freedom resonant nature. To bypass this problem, a piezoelectric with multiple shunts, each one of which can be matched to a mechanical mode, has been proposed with good results.

An innovative idea presented by dell'Isola and Vidoli consists in establishing a distributed piezoelectric coupling between continuous mechanical and electric media to form a "smart structure" capable of being adjusted for an optimal broadband damping. They proposed to think about controlling a continuous mechanical structure with its electrical analog to enhance a complete communication between the two systems[11].

1.1 Research Objectives

The goal of the research project of which this work is an integrate part is to study and realize electromechanical systems for distributed passive control of vibrations in mechanical structures by piezoelectric transducers and electric networks, following and improving upon what has been done in [11], [12] and [13]. In this context theoretical, numerical and experimental work is required.

The physical idea to be developed is to couple by means of PZT transducers a given mechanical continuum with an electric continuous medium possessing analogous characteristics in order to realize an electromechanical energetic exchange for a wide range of frequencies. Indeed, if waves propagate in the same fashion in the two media and if they have been tuned for a given wavelength, they are tuned for all. In this way one of the crucial issues of collocated passive control, the narrow band behavior, can be solved. The complexity of Piezo-Electro-Mechanical (PEM) structures allows the determination of analytical or semi-analytical solutions only for systems with a simple geometry, while, in the general case, the problem can be solved only by numerical methods. In both cases an experimental test is indispensable in order to validate the obtained results. In this thesis a finite element method based numerical code has been developed to study the behavior of a PEM beam. Subsequently the specimen has been tested in order to compare the obtained results.

1.2 Description of the system

The system we are dealing with is a simply supported beam with five pairs of PZT patches applied on each side of the beam and uniformly spaced, e.g., see Fig 1.1. The actuators

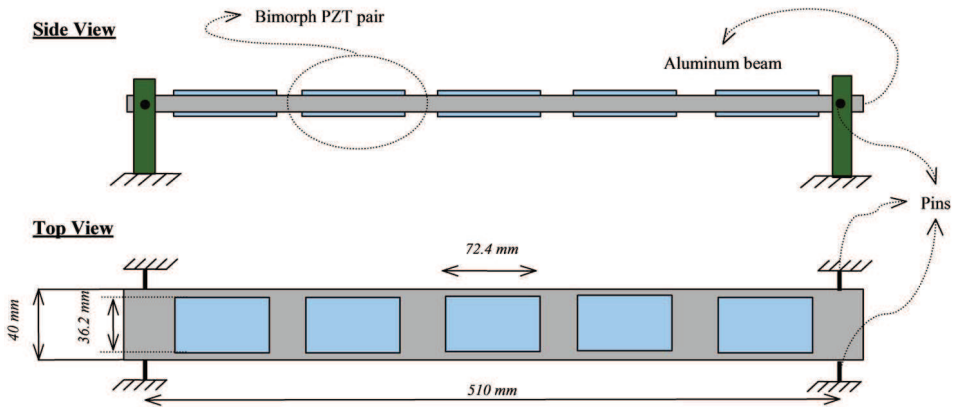

Figure 1.1: Piezomechanical beam.

of each couple are connected in counterphase (Fig 1.2) in order to provide a concentrated bending moment. In this thesis each PZT-actuator will be shunted by means of a suitable

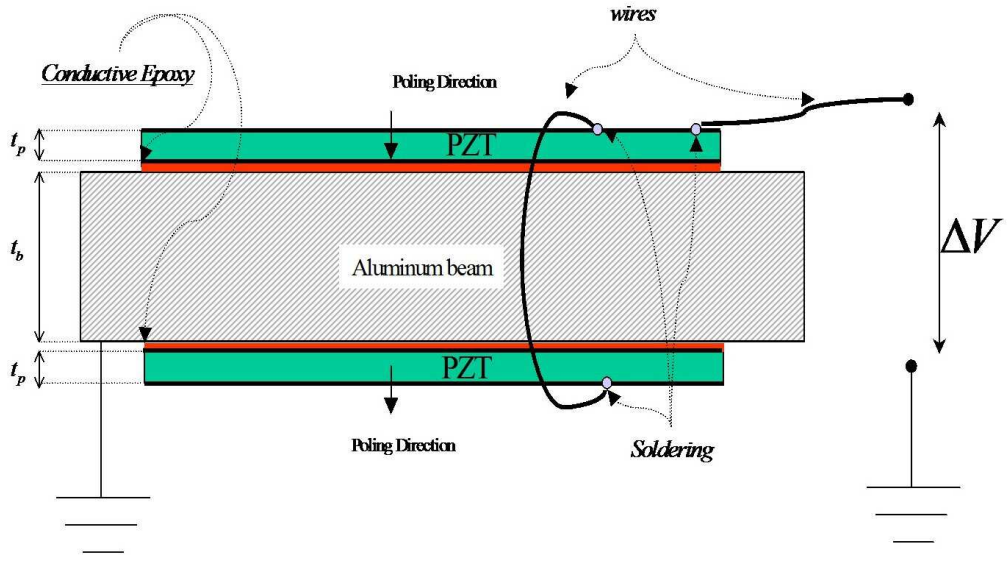

Figure 1.2: Bounded PZT patches in bimorph configuration.

RL circuit(Fig 6.6), and experimentally tested; the experimental results will be compared with those obtained by a numerical analysis of the same system. All devices have been designed in order to be easily used for further experiments, in particular, the realization and testing of a PEM beam with a distributed piezoelectric actuator connected via an electric

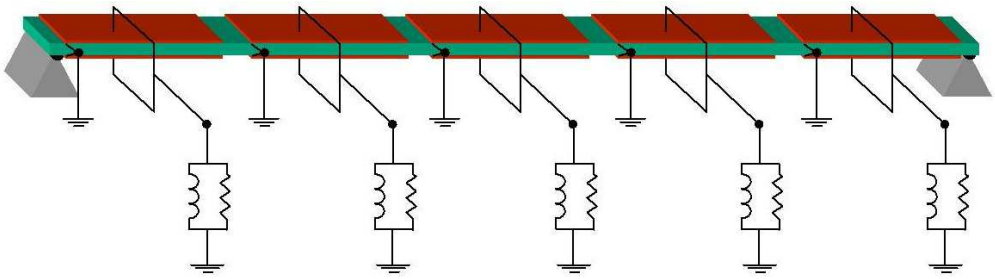

Figure 1.3: Piezoelectromechanical beam, multi-shunt configuration.

transmission line (Fig 1.4), in order to realize a wide frequency damping, as proposed in [12]. For a mathematical description of a single shunted actuator system vast literature is

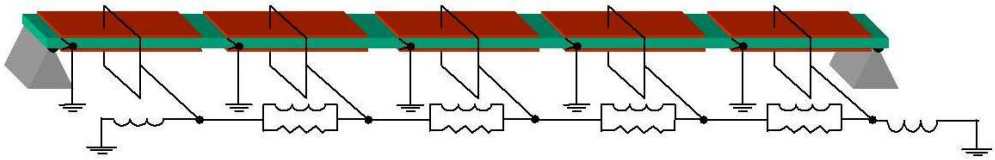

Figure 1.4: Piezoelectromechanical beam,transmission line configuration.

available [16],[17],[18]. Here a finite element method based numerical analysis of a multi-shunted system will be given.

Chapter 2

Numerical model

Piezoelectric materials present the characteristic of being able to transform mechanical energy into electric form, and vice-versa. Due to this property they have been widely used as mechanical sensors and actuators, and thus as elements of systems for the active control of mechanical vibrations. In passive control techniques their two-way transducer behavior is emphasized by using them to realize an electromechanical coupling to dissipate mechanical energy in electric components. Indeed, PZT patches can be bonded to mechanical structures to couple their oscillations with those of dissipative resonant electric networks. The design of this type of controlled system requires one to face two fundamental issues: (i) derive a model of the coupled system, and (ii) optimize the electric circuit to reduce the mechanical vibrations. Models of PZT patches used as actuators or as sensors are not useful in this context because they do not consider the two-way coupling. Indeed, in the first case, the electrical variable is assumed to be imposed and is independent of the mechanical one, the opposite is assumed in the second case. In coupled systems, neither one situation nor the other is dominant and the effective interdependence of mechanical and electrical variables must be considered. In this chapter an energy method based on the Principle of Virtual Power is used to derived an integral formulation of the balance equations of an electromechanical dissipative system with geometric irregularity composed of an elastic beam with bonded shunted PZT patches. The advantage of this approach is emphasized by consideration of a modular system, whose model is derived by studying a basic cell and then assembling the system. The optimal values of the shunting electrical parameters are found following the procedure presented in [14] and [15]. In a numerical application, a simply supported beam with five shunted PZT patches is considered. The optimal values for the electric inductors and resistors in the resonant shunts are found by considering a performance index related to the energy contents of the frequency response around the natural frequency of the coupled PZT-beam system, in particular the first mode will be considered. Numerical simulations on the optimized system are performed and its behavior is compared to those of non-optimal systems. By studying the free and forced oscillations, conclusions and suggestions for pos-

sible improvements are derived. In the present, following [15], a passive damping technique through a resonant shunted piezoelectric transducer will be studied. Here the coupled dynamics of a reduced modal model of the beam and the electric resonant system is presented in the Laplace domain and the impedance of the system is derived in a dimensionless form following previous work by Hagood and von Flotow [17]. An interesting original contribution is the optimization technique presented to choose the electrical parameters of the resonant shunts. For the optimization, the minimization of the cost function

$$J(L,R) = \max_{\omega \in [\omega_{\min}, \omega_{\max}]} abs[H(\omega)]$$

or alternative

$$J(L,R) = \sum_{i=1}^{p} w_i H(\omega_i) \bar{H}(\omega_i)$$

is proposed, where $H(\omega)$ is the mechanical frequency response function (FRF), ω the frequency, $[\omega_{\min}, \omega_{\max}]$ the relevant frequency interval, w_i a weighting factor, L, R the inductance and the resistance in the shunts to be optimized, respectively.

2.1 System description

In this section an electromechanical system is presented and its application for the passive control of mechanical vibrations will be discussed.

Let us consider a modular piezoactuated beam composed of an array of identical cells like that in Figure 2.1. The basic element is a $3-$*layered* beam composed of a central elastic layer with two sheets of PZT material bonded on a part of it. It is supposed that the two PZT layers have plated upper and lower surfaces and that they are electrically connected in parallel and out of phase, in order to realize a coupling between the beam bending mode and the electric potential across them (transducer in *bimorph* configuration). An electric resistor and inductor are connected in parallel to the PZT transducer to compose a parallel RLC resonant network. In general a system with an array of n elementary cells and arbitrary boundary conditions can be considered and modelled using the procedure presented here. However, in the following we will focus our attention on an experimental specimen that is a simply supported electromechanical beam composed of five elements. A sketch of the system is given in Figure 2.2 where the beam is considered to be electrically conductive and connected to ground, while the PZT pairs are connected in bimorph configuration. The mechanical parameters will be supposed fixed while the resistors and inductors in the shunts will be optimized to reduce the vibrations.

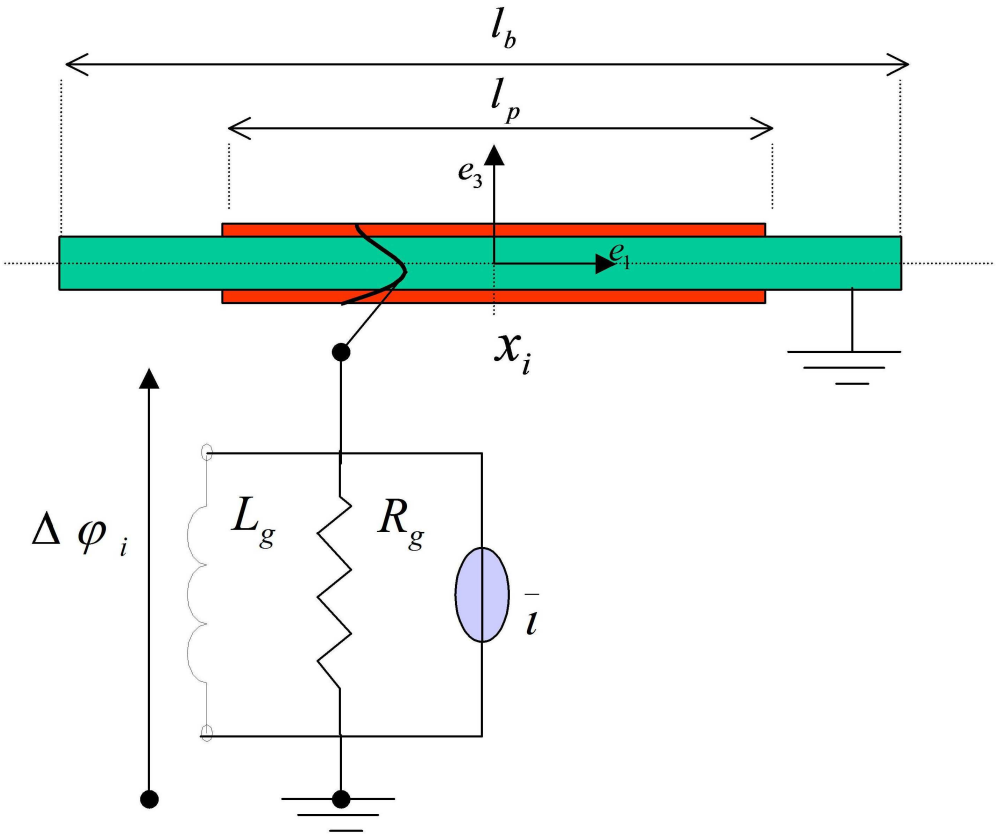

Figure 2.1: Basic Cell.

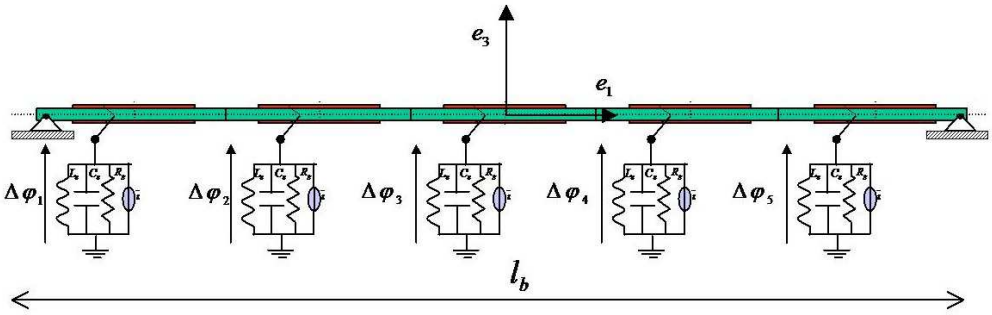

Figure 2.2: Complete system composed of 5 cells.

2.2 Mathematical model

To derive the balance equations for the considered continuum electromechanical dissipative system, the principle of the virtual power will be used. For a continuous body $\mathcal{B}$, this can be stated as follows[1].

Axiom 1. Principle of virtual power. *In a Galilean reference frame, and for an absolute Newtonian chronology, the virtual power of the internal forces of a system $\mathcal{B}$ balances the virtual power of external forces acting on the system, for any smooth virtual velocity field satisfying the homogeneous version of the prescribed essential boundary conditions*

Approaching the problem by the principle of virtual power, the model of the system is given once a kinematics is prescribed on it. The forces are defined by the powers expended on the corresponding virtual velocities. The virtual velocities are elements of the functional space of the time derivatives of the state variables and of their spatial gradients if continuum systems are considered. They must be smooth enough for the integrals involved in the power expressions to be evaluated and they must satisfy the homogeneous version of the prescribed essential boundary conditions; otherwise, they are arbitrary. The term "virtual" underlines that they aren't necessarily the actual velocities experienced by the system during a motion, they can be chosen arbitrarily in the space where they exist[2]. We will differentiate the virtual velocities form the actual ones, by adding a superscript "$*$".

Let $\mathcal{A}$ be the beam central axis. The Cartesian reference frame is chosen as in Figure 2.2

$$\mathcal{A} = \{\mathbf{p} = p_1 \mathbf{e}_1 : p_1 \in [-\frac{l_b}{2}, \frac{l}{2}]\} \tag{2.1}$$

Since parallel RLC circuits are considered, the state of each of these is completely described by the potential difference between their two nodes.

We will choose as state variables the mechanical vertical displacement $u_3(p_1, t)$ of the beam central axis and the time primitives $\{\Delta\phi_i\}_{i=1...n}$ of the electric potentials in the parallel RLC circuits.

The principle of virtual power will lead us to a weak formulation of the problem. The solution will be expressed as the set

$$\{u_3(p_1, t), \Delta\phi_1, ..., \Delta\phi_n\}$$

The scalar valued function $u_3(p_1, t)$ must be an element of the space of smooth functions defined on the one-dimensional domain occupied by the beam central axis that satisfy the prescribed essential boundary conditions (the natural ones are included in the weak formulation). This space is in general not the same as that of the virtual velocities since they

[1] In electromechanical problems the term "velocity" must be interpreted in a generalized sense.

[2] In general it is the Sobolev space H_0^n

must satisfy the homogeneous version of the prescribed essential boundary conditions. However, if a problem with homogeneous essential boundary conditions is considered[3], the two spaces coincide and the weak formulation of the problem will be also a Galerkin formulation[4]. Hence looking for an approximate solution in a finite dimensional subspace (Galerkin Approximation) the problem will be reduced to the solution of a system of ordinary differential equations. Here the beam displacement will be imposed so as to be proportional to the first mode of the purely mechanical, simply supported beam.

In the statement of the power balance the modularity property of the system will be used. Indeed, since the power is additive, the balance for a complex body can be derived from the sum of those of its parts. In particular the power balance for a modular system can be easily written as soon as the generic cell is examined. Hence in the following a detailed model of the basic cell composing the system will be given, then the model for the whole electromechanical beam will be assembled.

2.3 Basic cell

The basic cell in Figure 2.1 can be longitudinally divided into three regular parts: two lateral elastic beams and one central $3-layered$ piezoelectric beam with a resonant shunt. Let us note that the lateral parts are only a particular case of the central one when the piezoelectric layers (and the shunt) are absent. Thus the power expressions for the elastic beam can be easily derived as a special case once we know those of the central section. Finally the power of the whole cell can be written as the sum of those of its parts.

2.4 Kinematics

The following hypotheses are made:

1. The beam cross-sections remain rigid
2. Small deformations and linearized kinematics
3. No shear deformation
4. Perfect bonding between elastic and PZT layers

[3]A problem with non homogeneous boundary conditions can be restated as one with homogeneous boundary conditions with a simple change of variable. In our case of a pinned-pinned beam the essential boundary conditions are homogeneous.

[4]A Galerkin formulation is a weak formulation in which the spaces of the *trial* functions (*actual* velocities) and of the *test* functions (*virtual* velocity) coincide.

5. Constant electric field in the transducers

6. Uniform displacements along the thickness of the transducers equal to that of the surface in contact with the beam. This hypothesis is required for coherence once (5) is assumed.

The above six approximations are acceptable if the thickness of the piezoelectric layers, t_p, of the bonding layer, t_{bond}, and of the beam, t_b, are such that

$$t_{bond} \ll t_p \ll t_b \tag{2.2}$$

as is often the case in applications.

If the generic i^{th} cell is examined, let us denote by $\mathcal{B}_b^{(i)}, \mathcal{B}_{pu}^{(i)}, \mathcal{B}_{pl}^{(i)}$ the portions of the body occupied by the elastic layer, the upper PZT layer and the lower PZT layer, respectively, by $\mathbf{p}, \mathbf{u}(\mathbf{p})$, the position and displacement vectors of a generic point of the body, and by $\mathbf{S}(\mathbf{p})$ the corresponding straining tensor. Moreover let $\phi_i(\mathbf{p})$ be the time primitive of the electric potential in the PZT material, and $\Delta\phi_i$ the time primitive of the potential difference between the two nodes of the RLC parallel circuit. By the above six hypotheses the following kinematics is assumed[5]

- on $\mathcal{B}_b^{(i)}$

$$u(\mathbf{p},t) = \left[\begin{array}{ccc} u_1 - \frac{\partial u_3}{\partial p_1} p_3 & 0 & u_3 \end{array} \right]^T \tag{2.3}$$

$$S(\mathbf{p},t) = \left[\begin{array}{cccccc} \frac{\partial u_1}{\partial p_1} - \frac{\partial^2 u_3}{\partial p_1^2} p_3 & 0 & 0 & 0 & 0 & 0 \end{array} \right]^T \tag{2.4}$$

- on $\mathcal{B}_{pu}^{(i)}$

$$u(\mathbf{p},t) = \left[\begin{array}{ccc} u_1 - \frac{\partial u_3}{\partial p_1} \frac{t_b}{2} & 0 & u_3 \end{array} \right]^T \tag{2.5}$$

$$S(\mathbf{p},t) = \left[\begin{array}{cccccc} \frac{\partial u_1}{\partial p_1} - \frac{\partial^2 u_3}{\partial p_1^2} \frac{t_b}{2} & 0 & 0 & 0 & 0 & 0 \end{array} \right]^T \tag{2.6}$$

$$\phi^{(i)}(\mathbf{p},t) = \frac{\Delta\phi^{(i)}}{t_p}(p_3 - \frac{t_b}{2}) \tag{2.7}$$

$$\nabla\phi^{(i)}(\mathbf{p},t) = \left[\begin{array}{ccc} 0 & 0 & \frac{\Delta\phi^{(i)}}{t_p} \end{array} \right]^T \tag{2.8}$$

[5]All vectorial and tensorial quantitites are denoted with the Voigt notation once a reference $\mathcal{C} = \{\mathbf{o}, \mathbf{e}_1, \mathbf{e}_2, \mathbf{e}_3\}$ with $\mathbf{e}_1$ parallel to the central axis $\mathcal{A}$ and $\mathbf{e}_3$ parallel to polarization direction in the piezoelectric material are fixed. The longitudinal and transverse components of the central axis displacement vector are denoted by u_1 and u_3, respectively. The superimposed denotes the time derivative.

- on $\mathcal{B}_{pl}^{(i)}$

$$
\begin{aligned}
u(\mathbf{p},t) &= \left[\begin{array}{ccc} u_1 + \frac{\partial u_3}{\partial p_1}\frac{t_b}{2} & 0 & u_3 \end{array} \right]^T && (2.9)\\
S(\mathbf{p},t) &= \left[\begin{array}{cccccc} \frac{\partial u_1}{\partial p_1} + \frac{\partial^2 u_3}{\partial p_1^2}\frac{t_b}{2} & 0 & 0 & 0 & 0 & 0 \end{array} \right]^T && (2.10)\\
\phi^{(i)}(\mathbf{p},t) &= \frac{\Delta\phi^{(i)}}{t_p}(p_3 + \frac{t_b}{2}) && (2.11)\\
\nabla\phi^{(i)}(\mathbf{p},t) &= \left[\begin{array}{ccc} 0 & 0 & -\frac{\Delta\phi^{(i)}}{t_p} \end{array} \right]^T && (2.12)
\end{aligned}
$$

2.5 Constitutive relations

The body $\mathcal{B}$ is a composite material where the part $\mathcal{B}_b$ is a linear elastic homogeneous solid, and the parts $\mathcal{B}_{pu},\mathcal{B}_{pl}$ are linear homogeneous piezoelectric continua. Since no forces are applied on the beam lateral surface a uniaxial stress state along the $\mathbf{e}_1 - direction$ is assumed both in the beam and in the transducer. Moreover by the electric kinematic prescribed in (2.5) and in (2.9) an uniaxial electric state along the $\mathbf{e}_3 - direction$ is imposed, so that the reduced unidimensional constitutive equations are considered.

Linear elastic material In the layer $\mathcal{B}_b$ the linear homogeneous elastic constitutive law for a uniaxial tension state is assumed in the form

$$T_1 = c_{11} S_1 \tag{2.13}$$

Example 2. *If an aluminium beam is considered the c_{11} constant is*

$$c_{11} = E_Y = 70GPa$$

Linear piezoelectric material In the piezoelectric layers the linear piezoelectric constitutive equation for a uniaxial tension state and a uniaxial electric state, once the mechanical strain and the time primitive of the electric potential are chosen as state variables, are assumed in the form

$$
\begin{aligned}
T_1 &= c_{11}^E S_1 - e_{31}\frac{\partial\dot{\phi}}{\partial p_3} && (2.14)\\
J_3 &= e_{31}\dot{S}_1 + \epsilon_{33}^S\frac{\partial\ddot{\phi}}{\partial p_3} && (2.15)
\end{aligned}
$$

where the coefficients can be deduced by the material characteristics given in the technical data sheets from

$$
\begin{array}{ll} c_{11}^E = \frac{1}{s_{11}^E} & \epsilon_{11}^S = \frac{-d_{31}^2 + \epsilon_{33}^T s_{11}^E}{s_{11}^E} \\ e_{11} = \frac{d_{31}}{s_{11}^E} & \end{array} \tag{2.16}
$$

Example 3. *For the PZT material used in the transducers* piezo system *(PSI-5H4E Ceramic) the following material constants are given*

$$\begin{aligned} E_Y^E &= 62GPa \\ d_{31} &= -320 * 10^{-12} \frac{\mathrm{m}}{\mathrm{V}} \\ \epsilon_{33}^T &= 3800\epsilon_0 = 3.364\,6 \times 10^{-8} \frac{\mathrm{F}}{\mathrm{m}} \end{aligned}$$

Thus the following numerical values are found

$$c_{11}^E = E_Y^E = 6.2 * 10^{10} \tfrac{\mathrm{N}}{\mathrm{m}^2}, \quad \epsilon_{11}^S = \tfrac{-d_{31}^2 + \epsilon_{33}^T s_{11}^E}{s_{11}^E} = 2.729\,7 \times 10^{-8} \tfrac{\mathrm{F}}{\mathrm{m}}$$
$$e_{11} = \tfrac{d_{31}}{s_{11}^E} = -19.84 \tfrac{\mathrm{N}}{\mathrm{mV}}$$

Circuit elements Electric resistors (R), capacitors (C), and inductors (L) are considered. Their constitutive relations are the expression of the electric current ι flowing through them as a function of the time primitive of the potential $\Delta\phi$ across them[6]. They are

- capacitor
$$\iota = C\ddot{\phi}$$
- resistor
$$\iota = \frac{\dot{\phi}}{R}$$
- inductor
$$\iota = \frac{\phi}{L}$$
where R, L, C are the resistance, the capacitance and the inductance of the components.

2.6 Power expressions

Here the power expressions for the i^{th} cell of the periodic system with its center at the point

$$\mathbf{p}_i = x_i \mathbf{e}_1$$

are given. We will distinguish the virtual power of the external and the internal forces.

[6]Here the relation is stated between the current and the time primitive $\dot{\phi}$ of the electric potential instead of that between the current and the electric potential, as usual, because ϕ was chosen as a state variable.

Internal Powers The internal power $\mathcal{P}_{int}^{(i)}$ in the i^{th} cell in Figure 2.1 is given by

$$\mathcal{P}_{int}^{(i)} = \mathcal{P}_{int,m}^{(i)} + \mathcal{P}_{int,e}^{(i)}$$

where $\mathcal{P}_{int,m}^{(i)}, \mathcal{P}_{int,e}^{(i)}$ are the mechanical and the electric powers, respectively. From the assumed kinematics and constitutive equations, the explicit expressions of the virtual powers can be derived[7]. Considering the i^{th}cell the internal powers are

$$\begin{aligned}
\mathcal{P}_{int,m}^{(i)} &= \left(\begin{array}{c} \mathcal{P}_{int,m}^{(i)}\left(x_i - \frac{l_b}{2}, x_i - \frac{l_p}{2}\right) + \\ +\mathcal{P}_{int,m}^{(i)}\left(x_i - \frac{l_p}{2}, x_i + \frac{l_p}{2}\right) + \\ +\mathcal{P}_{int,m}^{(i)}\left(x_i + \frac{l_b}{2}, x_i + \frac{l_p}{2}\right) \end{array} \right) \\
&= K_f^{(b)} \int_{x_i - \frac{l_b}{2}}^{x_i - \frac{l_p}{2}} \frac{\partial^2 u_3}{\partial p_1^2} \frac{\partial^2 \dot{u}_3^*}{\partial p_1^2} dp_1 \\
&\quad + K_f \int_{x_i - \frac{l_p}{2}}^{x_i + \frac{l_p}{2}} \frac{\partial^2 u_3}{\partial p_1^2} \frac{\partial^2 \dot{u}_3^*}{\partial p_1^2} dp_1 + 2G_f \dot{\phi}_i \left[\frac{\partial \dot{u}_3^*}{\partial p_1} \right]_{x_i - \frac{l_p}{2}}^{x_i + \frac{l_p}{2}} + \\
&\quad + K_f^{(b)} \int_{x_i + \frac{l_b}{2}}^{x_i + \frac{l_p}{2}} \frac{\partial^2 u_3}{\partial p_1^2} \frac{\partial^2 \dot{u}_3^*}{\partial p_1^2} dp_1
\end{aligned}$$

$$\mathcal{P}_{int,e}^{(i)} = \left(-2G_f \left[\frac{\partial \dot{u}_3}{\partial p_1} \right]_{x_i - \frac{l_p}{2}}^{x_i + \frac{l_p}{2}} + 2H\Delta\ddot{\phi} + \frac{\Delta\phi}{L} + \frac{\Delta\dot{\phi}}{R} \right) \Delta\dot{\phi}^*$$

where $K_f^{(b)}, K_f$ are the bending stiffness of the simple and the $3-layered$ sections, respectively, G_f is a coupling constant, H is the capacitance of a piezoelectric patch and L, R are the circuit resistance and inductance, respectively.

External Powers The external power in the i^{th} cell can be split into the electrical and the mechanical contributions as

$$\mathcal{P}_{ext}^{(i)} = \mathcal{P}_{ext,m}^{(i)} + \mathcal{P}_{ext,e}^{(i)} \tag{2.17}$$

If the external actions are

1. A mechanical vertical force per unit length R_3

[7]These expressions can be derived by the power balance of a $3D$ model of the piezoelectric beam imposing on it the postulated electric and mechanical kinematics. The expressions obtained will present an explicit dependence on the variables p_2, p_3, thus they can be integrated on a section. In this way only the dependence on p_1 is left.

Symbol	Expression	S.I. units
$\alpha = \alpha^{(b)} + \alpha^{(p)}$	$\left(\int_{\mathcal{S}_b} \rho p_3^2\right) + 2\frac{t_b^2}{4}\int_{\mathcal{S}_{pu}} \rho$	$kg \;\; m$
$\lambda = \lambda^{(b)} + \lambda^{(p)}$	$\int_{\mathcal{S}_b} \rho + \int_{\mathcal{S}_p} \rho$	$\frac{kg}{m}$
$K_f = K_f^{(b)} + K_f^{(p)}$	$\left(\begin{array}{c}\int_{\mathcal{S}_b} c_{11} p_3^2 + \\ 2\left(\frac{t_b}{2}\right)^2 \int_{\mathcal{S}_{pu}} c_{11}^E\end{array}\right)$	$Nm^2, (kg)\frac{m^3}{s^2}$
$K_l = K_l^{(b)} + K_l^{(p)}$	$\int_{\mathcal{S}_b} c_{11} + 2\int_{\mathcal{S}_{pu}} c_{11}^E$	$N, (kg)\frac{m}{s^2}$
G_f	$\frac{t_b}{2t_p}\int_{\mathcal{S}_{pu}} e_{31}$	C, As
H	$\frac{1}{t_p^2}\int_{\mathcal{S}_{pu}} \epsilon_{33}^S$	$\frac{F}{m}, A^2\frac{s^4}{(kg)m^3}$

Table 2.1: Material characteristics: expressions and physical dimensions

2. A mechanical moment per unit length R_θ
3. An electric current generator $\bar{\iota}$ in the RLC parallel circuit

Then the terms in Eq.(2.17) can be written explicitly as

$$\mathcal{P}_{ext,m}^{(i)} = \left(\begin{array}{c}\mathcal{P}_{int,m}^{(i)}\left(x_i - \frac{l_b}{2}, x_i - \frac{l_p}{2}\right) + \\ + \mathcal{P}_{int,m}^{(i)}\left(x_i - \frac{l_p}{2}, x_i + \frac{l_p}{2}\right) + \\ + \mathcal{P}_{int,m}^{(i)}\left(x_i + \frac{l_b}{2}, x_i + \frac{l_p}{2}\right)\end{array}\right) \tag{2.18}$$

$$= \int_{x_i - \frac{l_b}{2}}^{x_i - \frac{l_p}{2}} \left(-\left(R_\theta + \alpha^{(b)}\frac{\partial \ddot{u}_3}{\partial p_1}\right)\frac{\partial \dot{u}_3^*}{\partial p_1} + \left(R_3 - \lambda^{(b)}\ddot{u}_3\right)\dot{u}_3^*\right) dp_1 \tag{2.19}$$

$$+ \int_{x_i - \frac{l_p}{2}}^{x_i + \frac{l_p}{2}} \left(-\left(R_\theta + \alpha\frac{\partial \ddot{u}_3}{\partial p_1}\right)\frac{\partial \dot{u}_3^*}{\partial p_1} + \left(R_3 - \lambda\ddot{u}_3\right)\dot{u}_3^*\right) dp_1 \tag{2.20}$$

$$+ \int_{x_i + \frac{l_p}{2}}^{x_i + \frac{l_b}{2}} \left(-\left(R_\theta + \alpha^{(b)}\frac{\partial \ddot{u}_3}{\partial p_1}\right)\frac{\partial \dot{u}_3^*}{\partial p_1} + \left(R_3 - \lambda^{(b)}\ddot{u}_3\right)\dot{u}_3^*\right) dp_1 \tag{2.21}$$

$$\mathcal{P}_{ext,e}^{(i)} = \bar{\iota}\Delta\dot{\phi}^*$$

where $\alpha, \alpha^{(b)}$ are the mass per unit length of the central and the lateral parts of the cell, respectively, while $\lambda, \lambda^{(b)}$ are their rotational inertias.

All geometric and material properties introduced in this section are with their physical dimensions and are listed in Table 2.1

2.7 Entire system

A weak formulation for a modular system $\mathcal{S}$ composed of an arbitrary number m of cells $\mathcal{S}_i$ like that in Figure 2.1 can be easily written considering the expressions for the powers of the elementary cell. Indeed the power balance

$$\mathcal{P}_{int}(\mathcal{S}) = \mathcal{P}_{ext}(\mathcal{S})$$

for $\mathcal{S} = \cup_{i=1}^{m} \mathcal{S}_i$ can be expressed as

$$\sum_{i=1}^{m} \mathcal{P}_{int}(\mathcal{S}_i) = \sum_{i=1}^{m} \mathcal{P}_{ext}(\mathcal{S}_i)$$

where $\mathcal{P}_{int}(\mathcal{S}_i)$,$\mathcal{P}_{ext}(\mathcal{S}_i)$ have been derived in the previous section.

By the weak formulation, an approximate model can be derived providing an approximate solution for the beam deflection in the finite dimensional vector space spanned by a set of m independent functions $\{\sigma_h(x)\}_{h=1...m}$ that are sufficiently smooth and that satisfy the homogeneous version of the prescribed essential boundary conditions. With this procedure the beam deflection $u_3(p_1,t)$ and the corresponding virtual velocity $\dot{u}_3^*(p_1,t)$ will be approximated by

$$u_3^m(p_1,t) = \sum_{i=1}^{m} q_i(t)\sigma_i(p_1) \tag{2.22}$$

$$\dot{u}_3^{*m}(p_1,t) = \sum_{i=1}^{m} r_i(t)\sigma_i(p_1) \tag{2.23}$$

and by the arbitrariness of the virtual velocities the problem reduces to a system of $m+n$ linear ordinary differential equations with constant coefficients that can be written in the form

$$M \begin{pmatrix} \ddot{\mathbf{q}} \\ \ddot{\phi} \end{pmatrix} + C \begin{pmatrix} \dot{\mathbf{q}} \\ \dot{\phi} \end{pmatrix} + K \begin{pmatrix} \mathbf{q} \\ \phi \end{pmatrix} = F \tag{2.24}$$

where

$$\mathbf{q} = (q_1(t), ..., q_m(t))^T$$

are the coordinates of the approximate beam deflection in the assumed basis and

$$\dot{\phi} = \left(\dot{\phi}_1(t), ..., \dot{\phi}_n(t)\right)^T$$

are the time primitives of the potential differences in the n shunting circuits. The system (2.24) can be rewritten in a dimensionless form to analyze it and perform numerical simulations. We will denote by a superscript tilde , "˜", dimensionless variables and by M_a, C_a, K_a, F_a the corresponding dimensionless matrices.

A Mathematica code has been written to write the power balance for a complex system once the expressions for powers of its parts are given together with its geometry. Moreover if a basis $\{\sigma_h(x)\}_{h=1..m}$ for the space in which an approximate solution must be found is imposed then the system (2.24) is derived automatically in a dimensionless form. The Mathematica code is reported in the Appendix.

The method will be illustrated with an example where numerical values will be used for the optimization.

2.8 Numerical example

Let us consider a simply supported aluminium beam composed of five modules with a resonant shunted PZT in bimorph configuration as in Figure 2.2. The electrical inductors and resistors have the same values in all the shunting circuits. If we denote by

$$\mathcal{P}_{int}(\mathcal{S}_i), \mathcal{P}_{ext}(\mathcal{S}_i)$$

the internal and the external powers of the ι^{th} cell $\mathcal{S}_i$, the power balance for the whole system can be stated as follows[8]

Hypothesis *The balance*

$$\sum_{i=1}^{5} \mathcal{P}_{int}(\mathcal{S}_i) = \sum_{i=1}^{5} \mathcal{P}_{ext}(\mathcal{S}_i) \tag{2.25}$$

must hold for each set of virtual velocities

$$\{\dot{u}_3^*(p_1,t), \Delta\dot{\phi}_1^*, \Delta\dot{\phi}_2^*, \Delta\dot{\phi}_3^*, \Delta\dot{\phi}_4^*, \Delta\dot{\phi}_5^*\}$$

with

$$\dot{u}_3^*(p_1,t) \in H_0^2(\mathcal{A}), \mathcal{A} = [\,-\frac{l_b}{2}, \frac{l_b}{2}]$$

where $H_0^2(\mathcal{A})$ is the Sobolev space of functions defined on $\mathcal{A}$ vanishing on its boundaries together with their derivatives up until the second order.

Looking for a solution for the beam deflection in the one-dimensional vector space spanned by the first mode of the simply supported beam without PZTs, we will assume

$$\begin{aligned} m &= 1 \\ \sigma_i(p_1) &= \cos(i\pi\frac{p_1}{l}) \end{aligned}$$

[8] If other types of basic elements are also present the power balance can be written in the same fashion adding the virtual powers of those elements.

where the reference in Figure 2.2 is fixed. Hence by the Mathematica program in the Appendix the following dimensionless system of $1+5$ linear ordinary differential equations is obtained:

$$M_a\ddot{z} + C_a\dot{z} + K_a z = F_a \tag{2.26}$$

with

$$z = \begin{pmatrix} \tilde{q}_1 & \tilde{\phi}_1 & \tilde{\phi}_2 & \tilde{\phi}_3 & \tilde{\phi}_4 & \tilde{\phi}_5 \end{pmatrix}^T$$

and

$$M_a = \begin{bmatrix} 1 & 0 & 0 & 0 & 0 & 0 \\ 0 & 1 & 0 & 0 & 0 & 0 \\ 0 & 0 & 1 & 0 & 0 & 0 \\ 0 & 0 & 0 & 1 & 0 & 0 \\ 0 & 0 & 0 & 0 & 1 & 0 \\ 0 & 0 & 0 & 0 & 0 & 1 \end{bmatrix} \tag{2.27}$$

$$C_a = \begin{bmatrix} 0 & \gamma_1 & \gamma_2 & \gamma_3 & \gamma_4 & \gamma_5 \\ -\gamma_1 & 2\zeta\omega & 0 & 0 & 0 & 0 \\ -\gamma_2 & 0 & 2\zeta\omega & 0 & 0 & 0 \\ -\gamma_3 & 0 & 0 & 2\zeta\omega & 0 & 0 \\ -\gamma_4 & 0 & 0 & 0 & 2\zeta\omega & 0 \\ -\gamma_5 & 0 & 0 & 0 & 0 & 2\zeta\omega \end{bmatrix} \tag{2.28}$$

$$K_a = \begin{bmatrix} 1 & 0 & 0 & 0 & 0 & 0 \\ 0 & \omega^2 & 0 & 0 & 0 & 0 \\ 0 & 0 & \omega^2 & 0 & 0 & 0 \\ 0 & 0 & 0 & \omega^2 & 0 & 0 \\ 0 & 0 & 0 & 0 & \omega^2 & 0 \\ 0 & 0 & 0 & 0 & 0 & \omega^2 \end{bmatrix} \tag{2.29}$$

The dimensional analysis was performed with a characteristic length x_0 corresponding to the beam thickness t_b and a characteristic time $t_0 = \frac{1}{\omega_0}$, where ω_0 is the natural frequency of the first mode of the beam without PZTs. Finally the characteristic time primitive ϕ_0 of the electric potential was taken to be

$$\phi_0 = \frac{L}{m} x_0$$

in order to maintain symmetries of the coupling coefficients[9].

Remark 4. *The dimensionless ω is a tuning parameter between the electric and the mechanical systems, while ζ is a damping parameter.*

[9] m is the modal mass obtained by projecting the equation of the electromechanical beam on the first mode of the beam without PZTs, and L is the electric inductance in the shunting circuits.

For the geometric dimensions

$$\begin{array}{cccc} l_b = 0.51\text{m} & l_e = \frac{l_b}{5} = 0.102\text{m} & w_b = 40\text{mm} & t_b = 4\text{mm} \\ l_p = 72.4\text{mm} & w_p = 36.2\text{mm} & t_p = 0.267\text{mm} & \end{array}$$

considering an aluminium beam with

$$E_Y = 70 * 10^9 \frac{\text{N}}{\text{m}^2}$$

and a PZT material for which

$$\begin{array}{c} E_Y^E = 62 * 10^9 \frac{\text{N}}{\text{m}^2} \quad , d_{31} = -320 * 10^{-12} \frac{\text{m}}{\text{V}} \\ \epsilon_{33}^T = 3800\epsilon_0 \end{array}$$

the dimensionless parameters are found to be

$$\begin{array}{ccccc} \gamma_1 = 0.03969, & \gamma_2 = 0.103926, & \gamma_3 = 0.12846, & \gamma_4 = 0.103926, & \gamma_5 = 0.039694, \\ \omega = \sqrt{\frac{38.0994\text{H}}{L}}, & & & \zeta = \frac{8431.731\Omega}{2R\omega}. & \end{array}$$

Considering the system to be forced only by a concentrated vertical force f applied at a generic point

$$\mathbf{p}_f = x_f \mathbf{e}_1$$

the corresponding dimensionless F_a is

$$F_a = \begin{pmatrix} 0.03532 * f & 0 & 0 & 0 & 0 & 0 \end{pmatrix}^T$$

Remark 5. *The stiffness and the mass matrices obtained are symmetric and positive definite as can be expected. Moreover the coupling between the mechanical and the electric parts of the system is in the gyroscopic form. Indeed the matrix C_a is antisymmetric if the dissipative terms due to the electric resistors are absent ($R \to \infty$ since it is a parallel resistance).*

Remark 6. *The coupling coefficients of the side circuits are symmetric with respect to one of the central circuit. This is a consequence of the assumption of a symmetric spatial shape for the mechanical displacement in a geometrically symmetric system.*

2.9 Optimization

In this section values of the electrical components in the shunting circuits will be optimized in order to reduce the mechanical vibrations. In the present case no analytical methods can be applied because a high order system is considered.

For the sake of simplicity and to respect the modularity of the system, it is assumed that the value of the inductors and resistors must be same in all shunts. We will focus our attention on the optimization of the electric resistance R and inductance L with the goal of reducing the free vibrations of the beam in Figure 2.2. The reduced model represented by the system (2.24) of 6 ordinary differential equations is considered.

2.9.1 Performance index (or Evaluation Function)

The performance index of a control technique can be chosen in different ways depending principally on the application considered and on the associated convergence of the optimization method. The principal goals in the vibrations control are the reduction of the Frequency Response Function (FRF) amplitude in a given frequency range and the minimization of the decay time in free oscillations. Despite the fact that the characteristics of the forced and the free systems are closely connected[10] the optimum for one of them does not coincide with the optimum for the other. Here the shunting circuits will be designed for the minimization of the free oscillations decay time. In the following this objective will be formalized and the performance index to be optimized will be written explicitly.

Let us consider the homogeneous version of the dimensionless reduced system (2.26)

$$\ddot{z} + C_a\dot{z} + K_a z = 0 \tag{2.30}$$

where z is a $n = 6$ dimensional vector and C_a, K_a are $n \times n$ matrices[11]. Introducing the new variables

$$y = \begin{pmatrix} y_1 \\ y_2 \end{pmatrix} := \begin{pmatrix} z \\ \dot{z} \end{pmatrix}$$

the system (2.30) can be rewritten as the first order system of $2n = 12$ ODEs

$$\dot{y} = Ay \tag{2.31}$$

where

$$A = \begin{pmatrix} 0 & -I \\ -K_a & -C_a \end{pmatrix}$$

The general solution of the Cauchy problem associated with (2.31) with

$$y|_{t=t_0} = y_o = \begin{pmatrix} z_0 \\ \dot{z}_0 \end{pmatrix}$$

is given by

$$y = e^{A(t-t_0)}y_0. \tag{2.32}$$

However, if $2n$ independent eigenvectors of A

$$\{u^{(i)}\}_{i=1\ldots n}$$

[10]The poles of the transfer function are the eigenvalues of the free system.

[11]For the non-dimensionalization rules used

$$M_a = I.$$

can be found, Eqn.(2.32) can be written in the form

$$y = \sum_{i=1}^{2n=12} c_i u^{(i)} e^{\lambda_i (t-t_0)}$$

and the corresponding z will be given by

$$z = \sum_{i=1}^{2n=12} c_i w^{(i)} e^{\lambda_i (t-t_0)} \tag{2.33}$$

where

$$w^{(i)} = (u_1^{(i)}, ..., u_n^{(i)})^T$$

and the constants $\{c_i\}_{i=1,..,2n}$ can be determined by solving the linear algebraic system

$$\begin{pmatrix} z \\ \dot{z} \end{pmatrix}_{t=t_0} = \begin{pmatrix} z_0 \\ \dot{z}_0 \end{pmatrix}$$

For the particular symmetries of the matrices C_a, K_a, the eigenvalues $\{\lambda_i\}_{i=1...n}$, that are solutions of

$$\det(A - \lambda I) = 0$$

are *complex conjugate* in pairs with a *negative real part*. Looking at Eqn.(2.33), it is easily understood that the decaying part of the solution is given only by the terms $e^{\mathrm{Re}(\lambda_i)(t-t_0)}$. Moreover, since for a generic initial data the solution is a linear combination of all the $2n$ terms in Eqn.(2.33), for sufficiently long times the largest term is that associated with the eigenvalue with the minimum absolute value of the real part. Indeed in order to minimize the decay time of the free oscillations, whose general expression is given by Eqn.(2.33), we will prescribe the maximum of the performance index

$$f(R, L) = \min_{i=1...2n} (Abs(\mathrm{Re}(\lambda_i))) = \max_{i=1...2n} (\mathrm{Re}(\lambda_i)) \tag{2.34}$$

2.10 Results

In the following, numerical simulations of the optimized reduced system are found in order to investigate its behavior and compare its performance in vibration suppression with non-optimized systems.

In Figure 2.3 the time evolution of the mechanical free oscillations for an initial mechanical displacement is plotted, while in Figure 2.4 the corresponding time history of the electric state variable in the RLC shunts is presented.

Looking at Figure 2.4 we note that

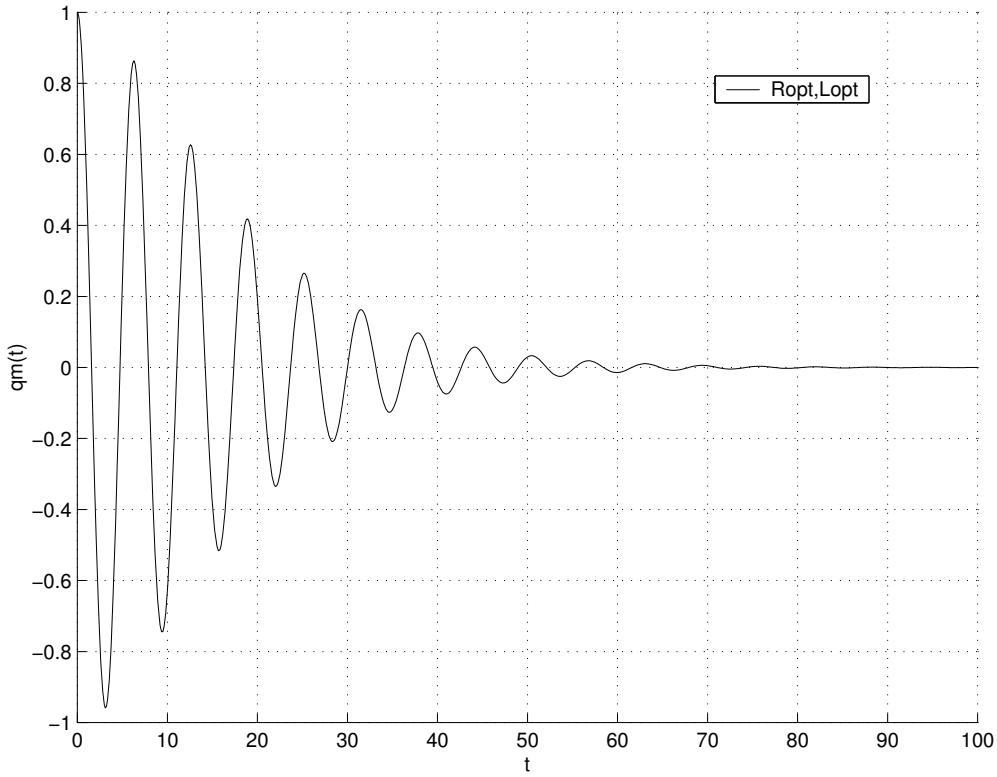

Figure 2.3: Mechanical variable time history for initial mechanical displacement in the optimized system.

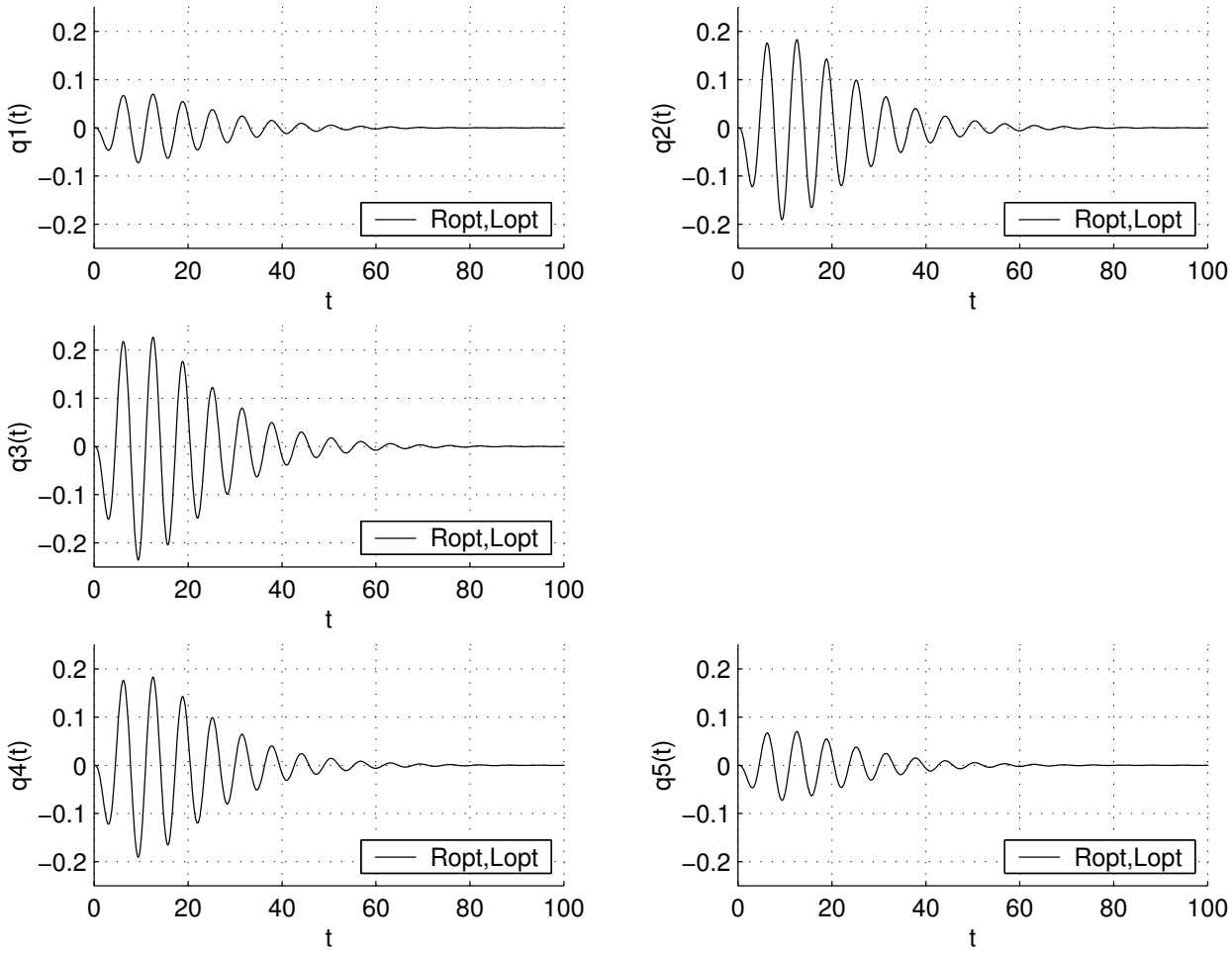

Figure 2.4: Free osclillations for initial mechanical dispalcement with L=Lopt, R=Ropt: time primitive of the electric potential in the five shunts.

1. The behavior of two circuits symmetrical with respect to the central one is identical.
2. The central circuit presents the greatest oscillations (thus the greatest energy dissipation, since the resistance is the same in all shunts).
3. The influence of the circuits near the supports is very weak.

These are a consequence of the spatial shape of the assumed mechanical mode. In particular observation 1 is due to its symmetry in a geometrical symmetric system, observations 2 and 3 to its strain energy distribution. Indeed for the hypothesized modal shape the strain energy density is maximum in the central region, while it is zero at the supports.

We can conclude that, as expected, in applications similar to that proposed here, it is not convenient to tune all shunted PZT's on the same mode since some of them have a low efficiency. For example, the lateral circuits can be coupled with the third or the second mode of the mechanical beam to also add damping to them. The performance on the first mode will remain presumably the same, while new goals will be achieved with no further efforts.

In Figure 2.5 the free vibrations for the optimal system are compared with that of non-optimal situations. We note the presence of beats for $R = 2R_{opt}$. As can be noted by looking at Figure 2.6, the system presents the inconvenience of a high parametric sensitivity.

In Figures 2.6 and 2.7 the modulus of the mechanical frequency response for mechanical forcing is plotted for different values of the electric resistance and inductance. Looking at the plot in Figures 2.6 and 2.7 we note that the optimal resistance for free vibrations do not exactly coincide with that which minimize the frequency response. However the result with $R = R_{opt}$ is very good and differs only slightly from the best one.

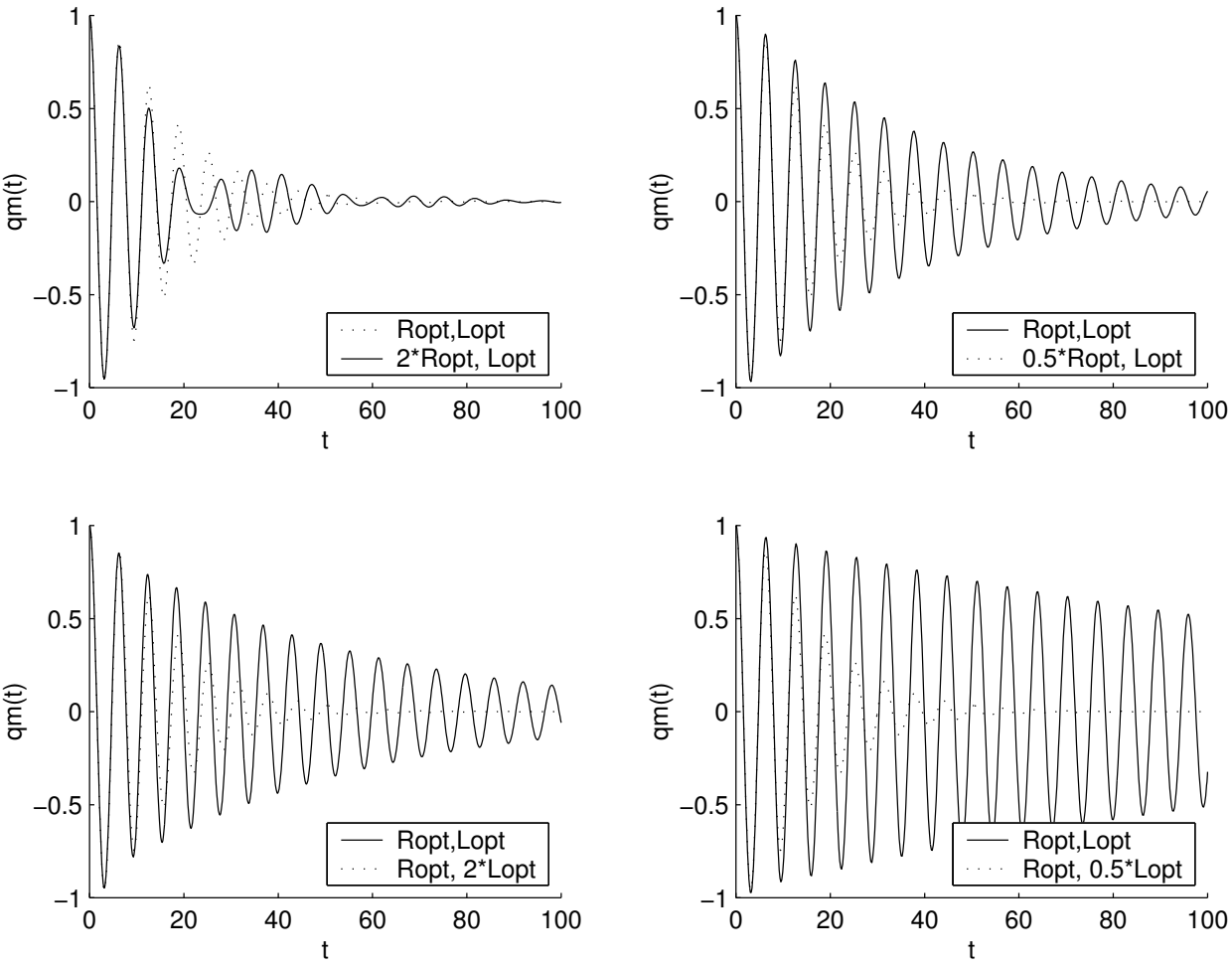

Figure 2.5: Mechanical free oscillation for different values of the electric parameters.

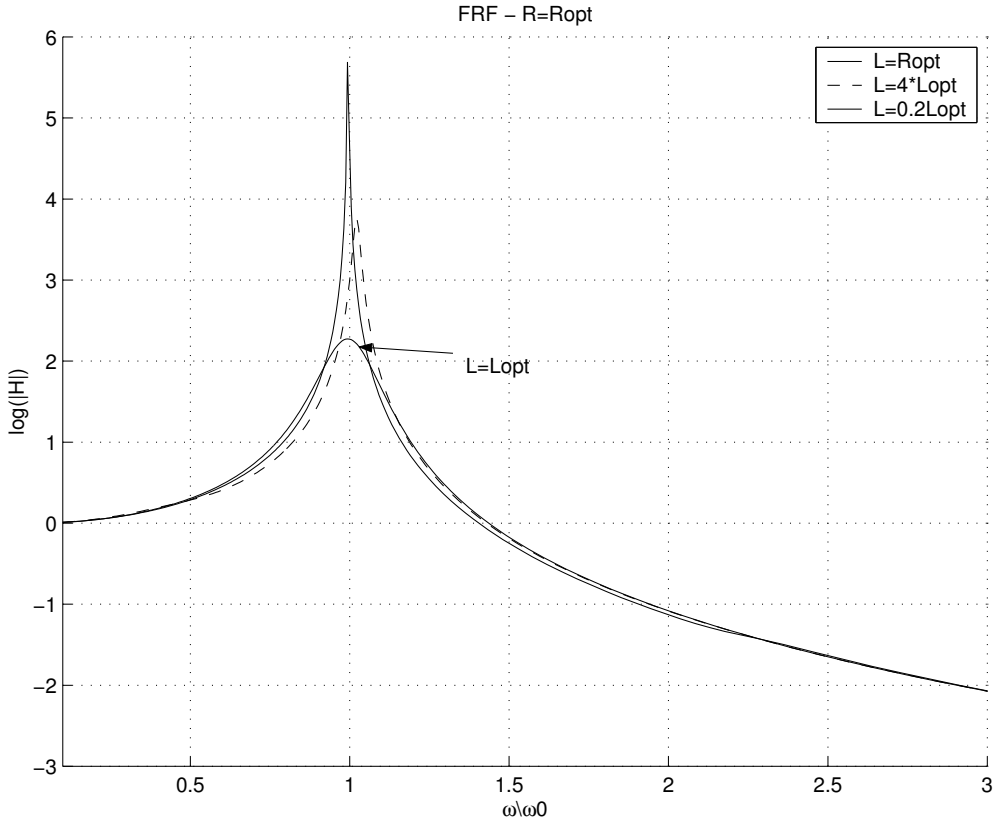

Figure 2.6: Mechanical FRF modulus with R=Ropt and different values of L.

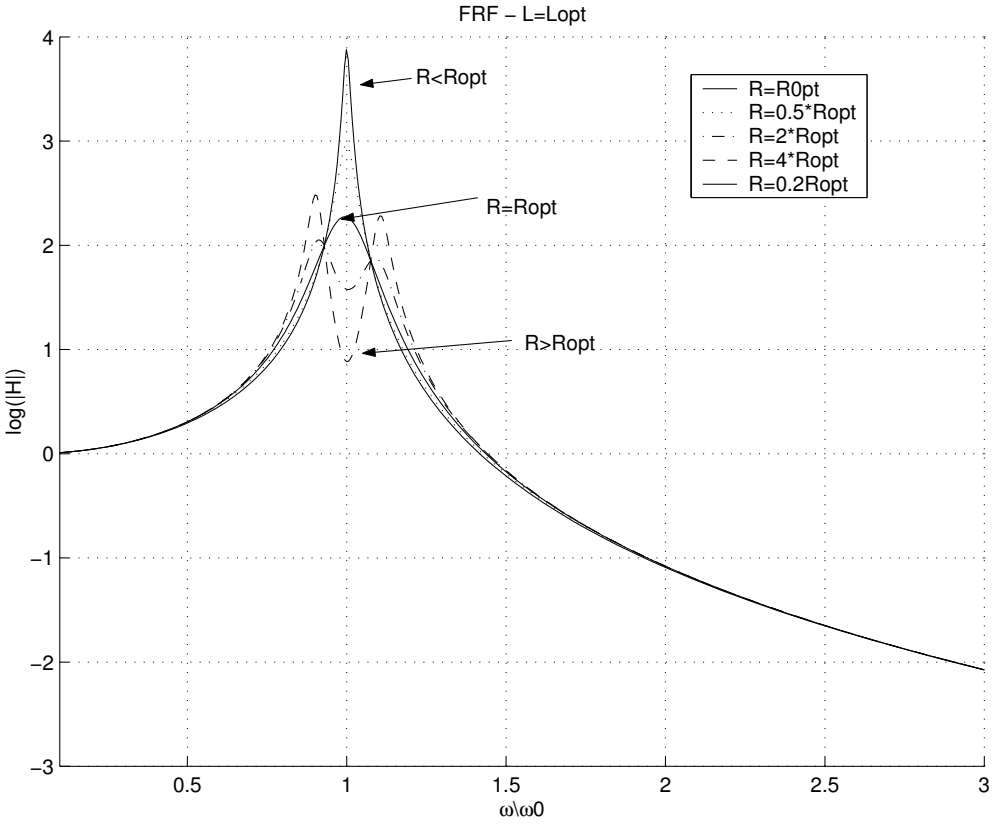

Figure 2.7: Mechanical FRF with L=Lopt and different values of R.

Chapter 3

System Design and Experimental Validation

The experimental apparatus has been designed to facilitate the measurements and to emphasize the relevant physical aspects utilizing materials and geometrical parameters frequently needed in engineering applications. The original idea carried on in this project is employing a distributed piezoelectric coupling between a mechanical and an electrical continuum for vibration damping. As a matter of fact only a lumped version of an electrical continuum effectively coupled with a mechanical structure can be experimentally tested. Hence a modular Piezo-Electro-Mechanical (PEM) beam has been constructed.

Two critical technological problems faced are:

1. Bond the PZT transducers on the beam leaving access to the electrodes.
2. Use large value, adjustable inductors with low parasite resistances.

3.1 Beam with PZT Transducers

The simply supported beam with five pairs of PZT transducers in bimorph configuration in Figure 3.1 has been built. The beam was made of aluminum (Young modulus $E_Y = 70 \times 10^9$Pa, mass density $\rho_b = 2700\frac{\text{kg}}{\text{m}^3}$).

The geometrical dimensions of the beam are:

length $l_b = 51$mm
width $w_b = 40$mm
thickness $t_b = 4$mm

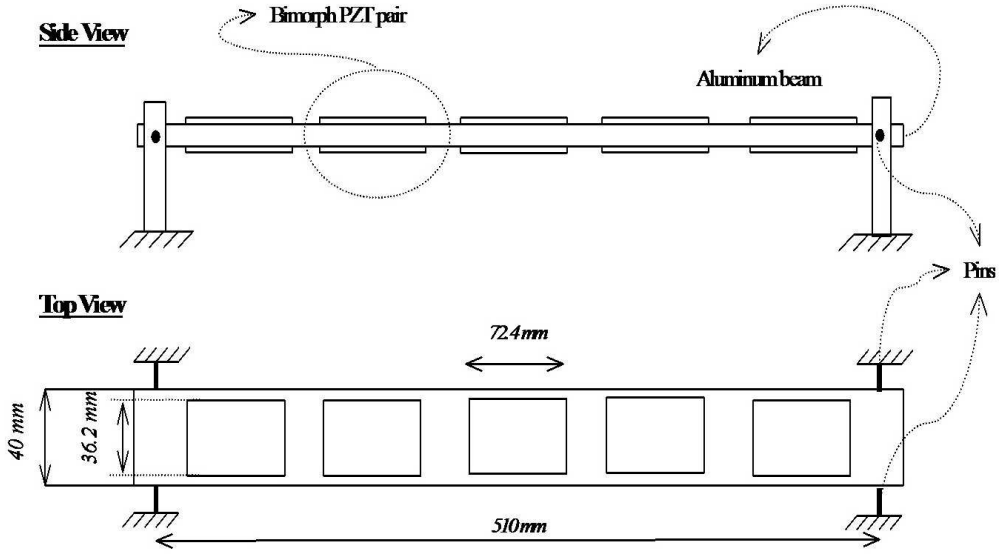

Figure 3.1: Pinned-pinned beam with five bimorph PZT pairs.

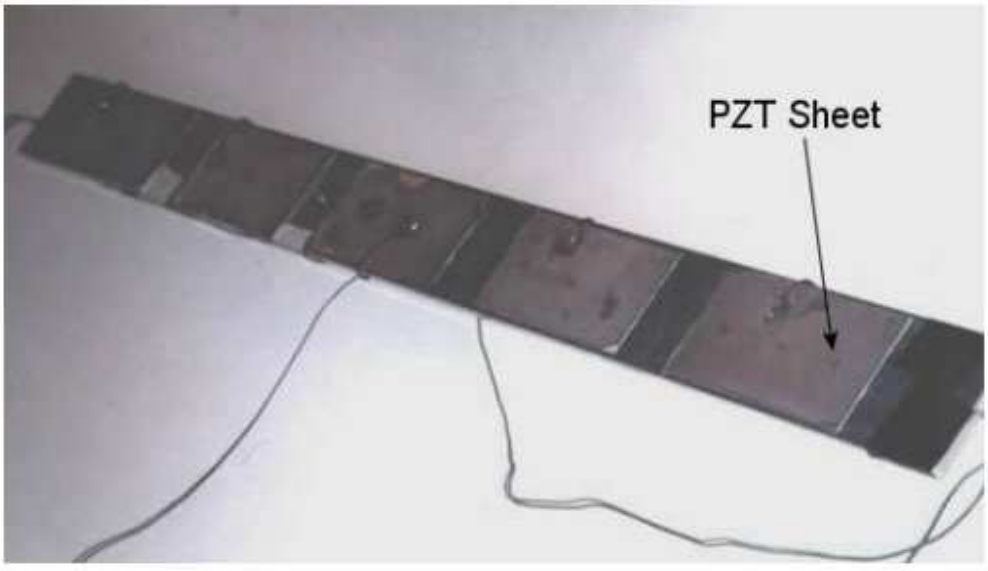

Figure 3.2: Beam with PZT transducers.

These have been chosen to maintain the first natural frequency above 30Hz to avoid difficulties for dynamical measurements.

The system can be interpreted as the assembly of five modules as is evident from Figure 3.1. The number of basic cells has been chosen to realize a modular system that, in the frequency range of interest, can be approximated sufficiently well by an homogenized continuous model. Here we focused on the first mechanical spatial mode of vibration of the simply supported beam.

3.2 Piezoelectric Transducers

The *Piezo System T110-H4E-602* transducers were used. They are composed of a single sheet of PZT *PSI-5H4E Ceramic* material with nickel electroded upper and lower surfaces. The dimension of PZT patch are shown in Figure 3.1, and electro-mechanical properties of the PZT material are listed in Figure 3.4. Each item is sold as a parallelepiped of dimensions $74.2 \times 74.2 \times 0.267$mm.

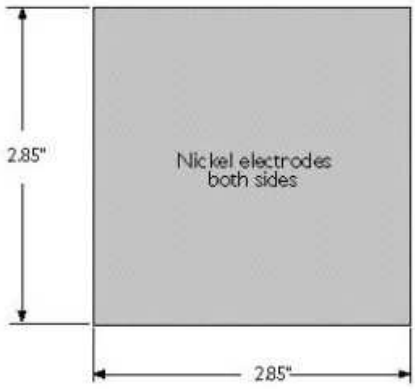

Figure 3.3: Single sheet piezoelectric transducer (dimensions in inches).

The sheet was cut using a diamond edge into two equal parts with

$$\text{length } l_p = 74.2\text{mm}$$
$$\text{width } w_p = 36.1\text{mm}$$
$$\text{thickness } t_p = 0.267\text{mm}$$

The transverse dimensions have been chosen to agree with those of the beam. The transducers have been designed with two contrasting goals: to have a high electromechanical coupling and to limit the voltage across the two electrodes. Indeed, realizing electronic devices for high voltage applications is a technological problem, especially when operational amplifiers are adopted.

The choice of this type of transducers was motivated by the following factors:

PIEZOELECTRIC			
Composition		Lead Zirconate Titanate	
Material Designation		PSI-5H-S4-ENH (Industry Type 5H, Navy Type VI)	
Relative Dielectric Constant (@ 1 KHz)	K^T_3	3800	
Piezoelectric Strain Coefficient	d_{33}	650×10^{-12}	meters/Volt
	d_{31}	-320×10^{-12}	meters/Volt
Piezoelectric Voltage Coefficient	g_{33}	19.0×10^{-3}	Volt meters/Newton
	g_{31}	-9.5×10^{-3}	Volt meters/Newton
Coupling Coefficient	k_{33}	0.75	
	k_{31}	0.44	
Polarization Field	Ep	1.5×10^6	Volts/meter
Initial Depolarization Field	Ec	3.0×10^5	Volts/meter
MECHANICAL			
Density		7800	$Kg/meter^3$
Mechanical Q		30	
Elastic Modulus	Y^E_3	5.0×10^{10}	$Newtons/meter^2$
	Y^E_1	6.2×10^{10}	$Newtons/meter^2$
THERMAL			
Thermal Expansion Coefficient		$\sim 3 \times 10^{-6}$	meters/meter °C
Curie Temperature		250	°C

Figure 3.4: Characteristics of the PZT material.

1. The possibility of cutting a transducer into a desired shape
2. Its constructive simplicity that allows a good understanding of its behavior
3. Good characteristic of the PZT material
4. High quality/price ratio

Each bimorph pair of PZTs has been fabricated as reported in Figure 3.5. The two sheets were connected in *parallel* and *out-of-phase* to obtain a flexural-electric coupling. The electric connections to the electrodes have been realized using a 60/40 solder alloy and a specific flux for nickel electrodes. The PZT sheets were bonded to the aluminum beam using an electrically conductive silver-loaded epoxy resin. Thus the lower electrode of the PZT was electrically accessible by means of the conductive beam that was grounded. The connections were optimized to reduce the number and the length of wires to limit the induced noise.

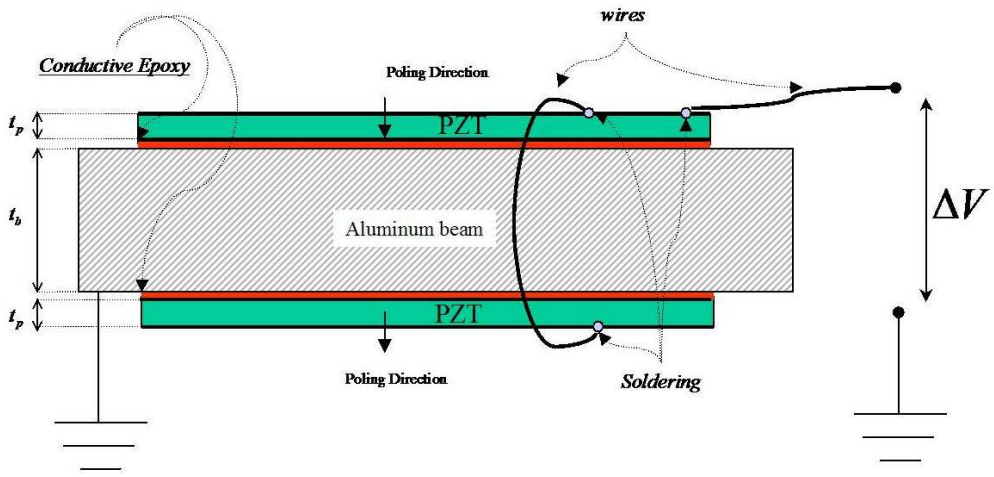

Figure 3.5: PZT pair in bimorph configuration: detailed construction scheme.

3.3 Electric Networks

In principle the electric networks are composed only of elementary components such as resistors, capacitors and inductors. However, as found by theoretical and numerical analyses, large value adjustable inductors with low parasitic resistances are required. Completely passive components with those characteristics are not convenient. Hence synthetic inductors have been used.

3.4 Inductance

The necessity to have high value inductors (up to ten Henries), given by the numerical analysis as well as in theoretical investigations [12], makes it impossible to use passive elements. These elements, in fact, would be too encumbering, and would have too low of a quality ratio with respect to the project restrictions.

In order to overcome this problem, the inductors will be realized by means of RC-active circuits. The available literature about this is vast; since the first papers (Riordan 1969, Antoniou 1970, Orchad and Shean 1970) many different RC-active circuits for inductor simulation have been proposed. Below we describe the circuit chosen for the experiment, specify its features and briefly give various steps.

3.4.1 Grounded inductor

The inductor synthesis is based on GIC (general impedance converters), Figure 3.6. These are two port nets that show, if one of the ports is shunted with an impedance Z_l, we have impedance by the second port that is proportional to Z_l, the constant of proportionality depends upon the particular GIC used.

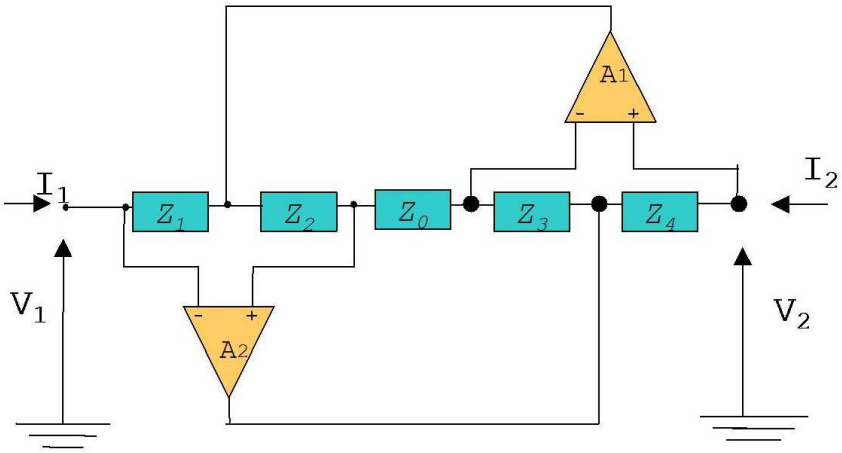

Figure 3.6: Antoniou's GIC.

One of these GIC's proposed by Antoniou is shown in Figure 3.7.

The analysis of the circuit [22], considering the operational amplifiers as ideal elements, gives the impedance of port 1 as:

$$Z_{in} = \frac{Z_1 Z_3}{Z_2 Z_4} Z_l$$

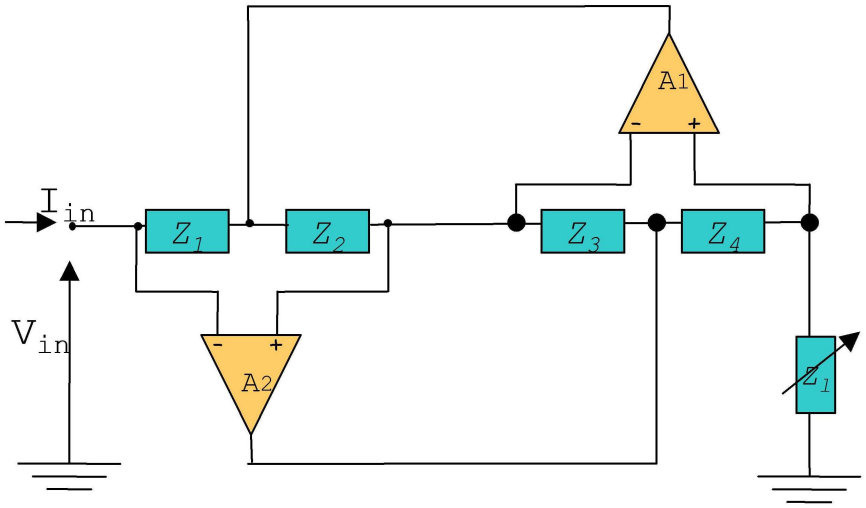

Figure 3.7: Shunted Antoniou's GIC.

It is clear from this formula that, if one of the impedances Z_2 or Z_4 is a capacitor and all others resistors, the circuit becomes an inductor whose value is fixed by the values of all elements of the circuit.

From this analysis it appears that either impedance Z_2 or Z_4, can be chosen as a capacitor (the resulting circuits are shown in Figures 3.8 and 3.9, respectively). By a more exact

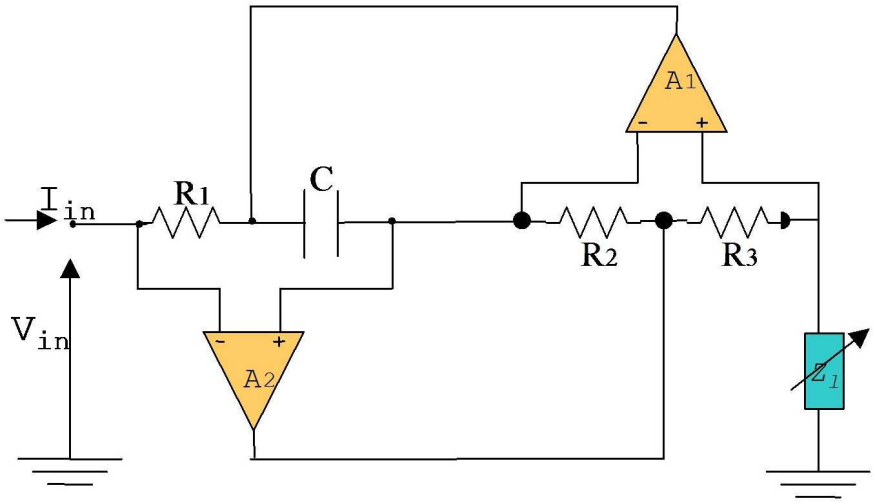

Figure 3.8: Active inductor.

analysis of the circuit [24] made by substituting the operational amplifiers by their equivalent circuit (Figure 3.10), we find that the quality ratio of the circuit is not infinite, but has a finite value depending on the frequency.

This value can be maximized by choosing

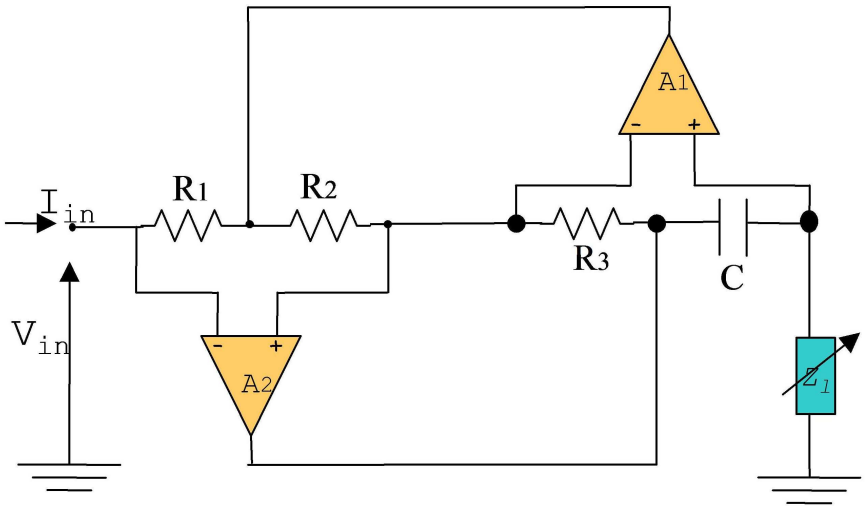

Figure 3.9: Active inductor.

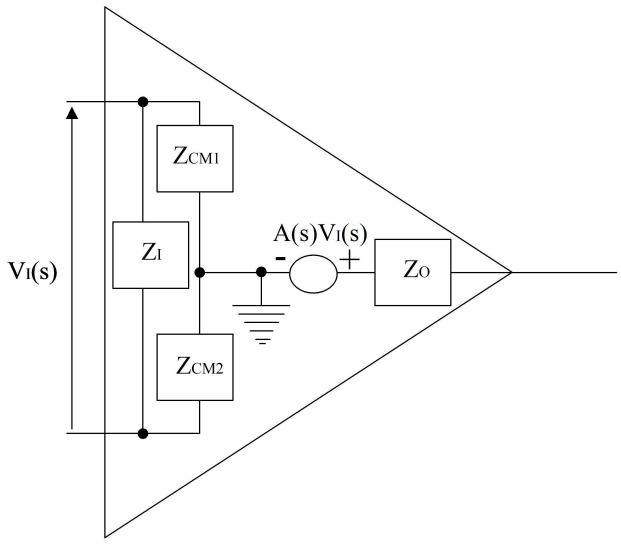

Figure 3.10: Refined model of the operational amplifier.

$\omega_{t1} R_l = \omega_{t2} R_4$

for the circuit in Figure 3.8

or $R_2 = R_3$

for the circuit in Figure 3.9. Also, ω_{t1} and ω_{t2} are the unit gain frequencies of A_1 and A_2, respectively.

The second condition to optimize quality is easier to realize experimentally, and for this reason the second type of GIC has been chosen.

Remembering that the quality ratio is a loss index due to Joule effect, and that it is not infinite, we find that the designed circuit is not an ideal inductor, but is better schematized as an inductor with a resistor connected in series. Below it is shown to be a simple modification of the Antoniou circuit, where the input impedance in the shunt conditions shown in Figure 3.11 becomes:

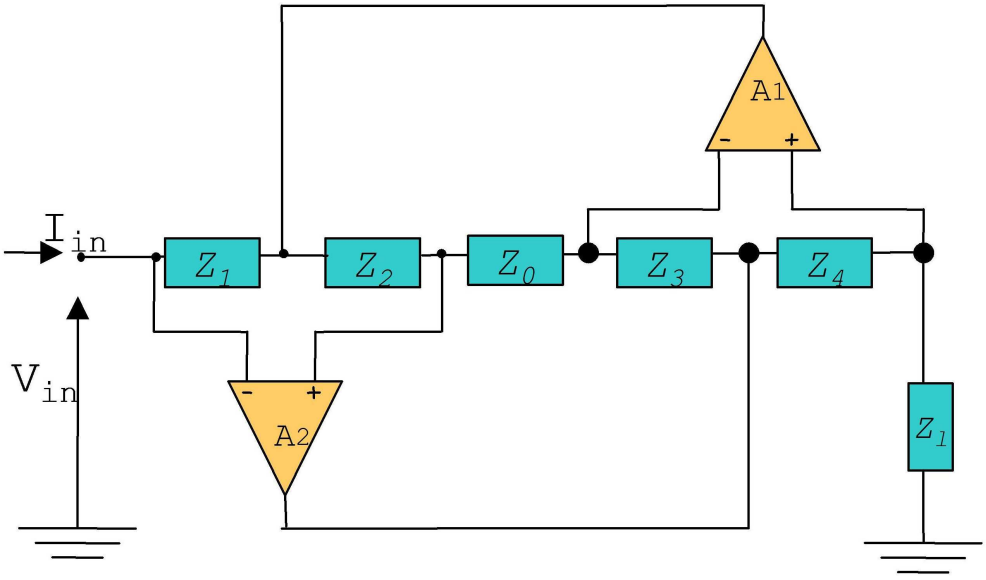

Figure 3.11: Shunted modified Antoniou's GIC.

$$Z_{in} = \frac{Z_1 Z_3}{Z_2 Z_4} Z_l - \frac{Z_3}{Z_2 R_0}$$

The negative resistor can be useful in order to avoid losses, obtaining in that way an inductor with a quality ratio theoretically infinite.

3.4.2 Floating inductor

All inductors shown until now have a common feature, i.e., they have one end grounded. Looking at the electrical topology of the transmission line configuration in Figure 1.4, it is clear that we need to realize a floating inductor.

The synthesis of this new element has been made by a GIC insertion technique based on the work of Bruton[24]. We briefly recall it. Consider the circuit in Figure 3.12:

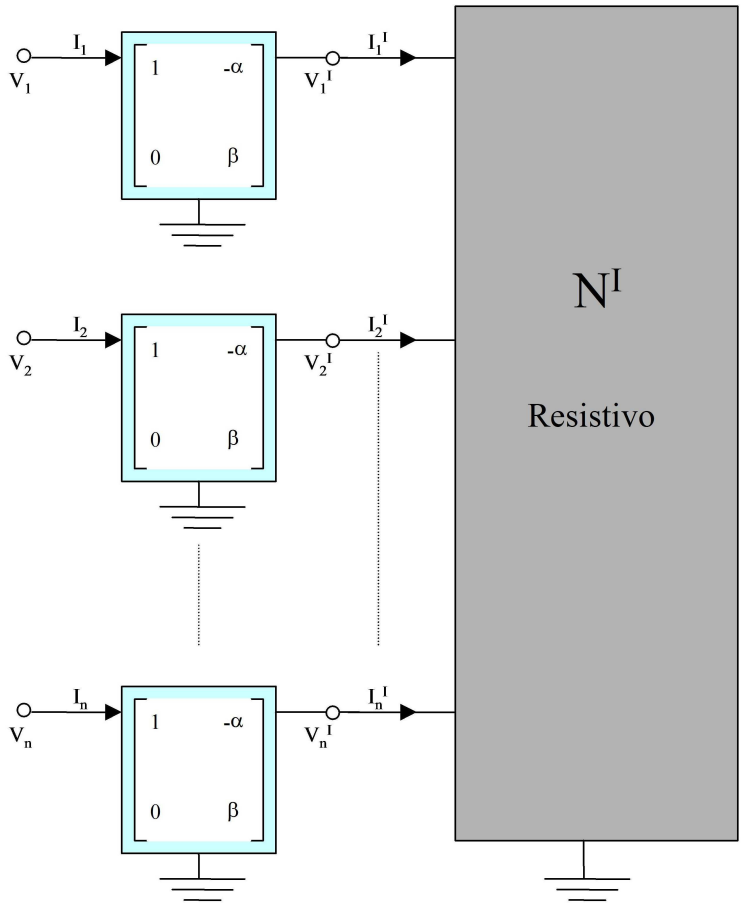

Figure 3.12: Full GIC's connection.

The N^I is a purely resistance n-port net, connected to a GIC net to form the N net. We characterize the N^I by its admittance matrix:

$$I^I = Y^I V^I \tag{3.1}$$

while for the GICs we can use the relation previously found:

$$V = V^I - \alpha I^I \Rightarrow V^I = V + \alpha I^I \tag{3.2}$$

$$I = \beta I^I \Rightarrow I^I = \beta^{-1} I \tag{3.3}$$

with $\alpha = \dfrac{Z_0 Z_4}{Z_3}$ and $\beta = \dfrac{Z_2 Z_4}{Z_1 Z_3}$.
Substituting (3.2) and (3.3) in (3.1) we find:

$$\beta^{-1} I = Y^I V + Y^I \alpha \beta^{-1} I$$

that is

$$I = \left(\beta \left(ID - \alpha Y^I\right)^{-1} Y^I\right) V \tag{3.4}$$

where ID is the identity matrix.

We now analyze, by means of this relation, the circuit shown in Figure 3.13. In order to do

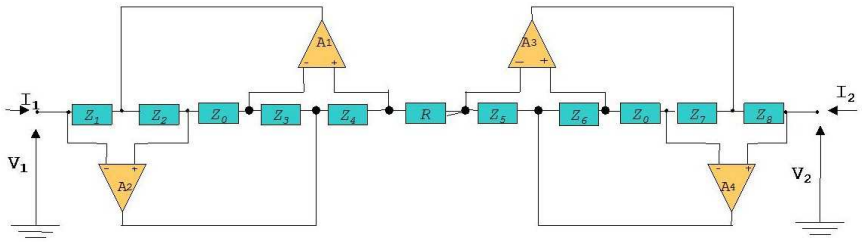

Figure 3.13: GIC series connection circuit.

that we need to find the transmission matrix of the circuit shown in Figure 3.14, that is a modification of Antoniou's GIC, presented in [19].

We have:
$\begin{pmatrix} V_1 \\ V_2 \end{pmatrix} = T \begin{pmatrix} \iota_1 \\ \iota_2 \end{pmatrix}$ with $T = \begin{pmatrix} A & B \\ C & D \end{pmatrix}$

and $A = \dfrac{V_1}{V_2}_{\iota_2=0}$. Considering Figure 3.15 (always regarding the operational amplifiers as ideal elements) we find that current does not flow in Z_4. Then $V_2 = V_6$, but $V_2 = V_5 = V_6$

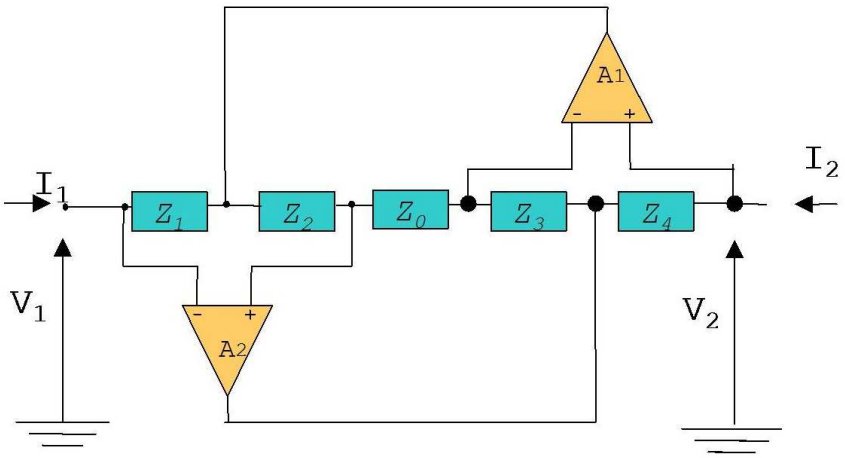

Figure 3.14: Senani's GIC.

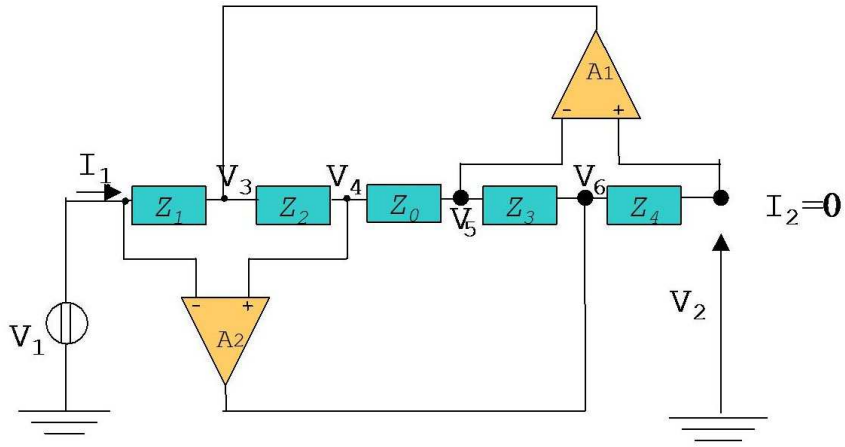

Figure 3.15: Senani's Gic.

also. Thus current does not flow in Z_3, nor, consequently in Z_0, so that $V_5 = V_4$. But $V_1 = V_4 = V_2$ so finally we obtain $A = 1$. Using the same reasoning for values of B, C and D, we obtain for the transmission matrix:

$$T = \begin{pmatrix} 1 & -\dfrac{Z_0 Z_4}{Z_3} \\ 0 & \dfrac{Z_2 Z_4}{Z_1 Z_3} \end{pmatrix}.$$

Now we use the general relation previously found to analyze the circuit in Figure 3.13.

We have for the N^I net:

$$Y^I = \begin{pmatrix} \dfrac{1}{R} & -\dfrac{1}{R} \\ -\dfrac{1}{R} & \dfrac{1}{R} \end{pmatrix}$$

Now, substituting in (3.4), and expanding, we find:

$$I = \begin{pmatrix} \dfrac{1}{R^I} & -\dfrac{1}{R^I} \\ -\dfrac{1}{R^I} & \dfrac{1}{R^I} \end{pmatrix}$$

with

$$Z^I = R\frac{Z_1 Z_3}{Z_2 Z_4} - 2\frac{Z_0 Z_1}{Z_2}, \tag{3.5}$$

The two port net obtained is, therefore, equivalent to the one shown in Figure 3.16. In this way we have realized a floating inductor with a negative resistor in series. This latter circuit, properly tuned, can be used to eliminate the non-ideality of the inductor, obtaining in this way a circuit element with a very high quality factor (theoretically infinite).

A negative aspect of this solution is that operational amplifiers need a dual DC power source to work. Thus, despite our desire for, components of the electric network that are theoretically passive, its actual realization requires a power supply. However the power absorbed by the Op-Amp is very low and it is not comparable with that required in active control techniques. The operational amplifiers $TL-081$ have been used with a voltage of $\pm 12V$ furnished by two batteries connected as shown in Figure 3.17.

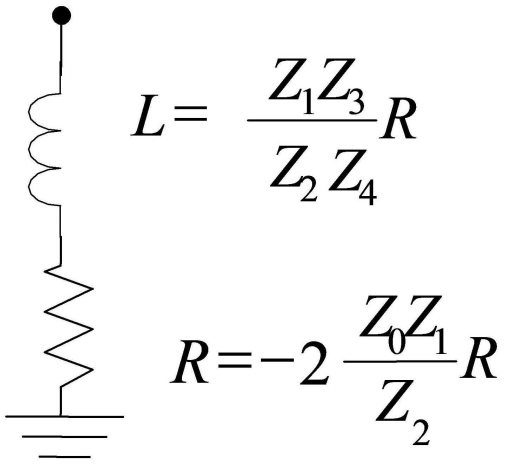

Figure 3.16: Equivalent circuit of the active inductor.

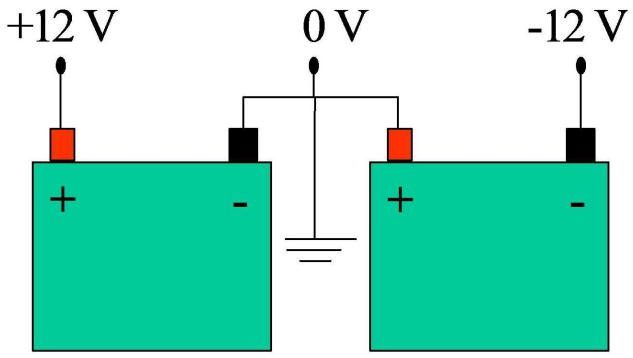

Figure 3.17: Batteries for supply of Op-Amps.

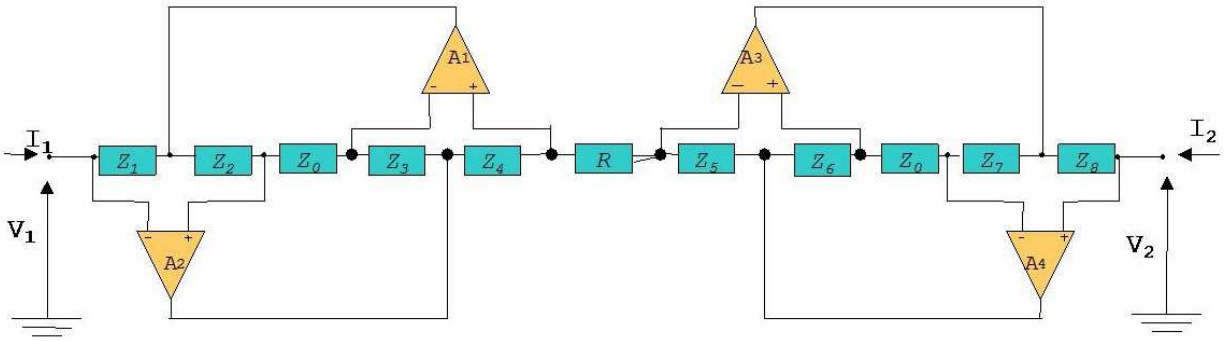

Figure 3.18: GIC series connection.

3.5 Inductance

The experimental synthesis of the circuit started with a prototype realization, made by hand (a picture of this prototype is shown in Figure 3.22). The values of the inductor elements have been chosen in order to obtain an inductance value near the optimal value suggested by the numerical investigation for the multi-shunted system (40-60H). We choose, referring to Figure 3.13,

$$Z_1 = Z_8 = 3\text{k}\Omega, \quad Z_2 = Z_7 = 1\text{k}\Omega,$$
$$Z_3 = Z_6 = 1\text{k}\Omega, \quad Z_4 = Z_5 = 10\mu\text{F}.$$

For Z_0 (the resistor that now provides the negative resistance) we use a potentiometer from 0 to $1k\Omega$, while for R (the resistor that now fixes the inductor value), we realized it as a connection in series of two potentiometers, for the first a 0-10K trimmer has been used, Figure 3.19, while for the second one, a high precision potentiometer of 1kΩ with a variable selector, Figure 3.21, that has a resolution of 1Ω, Figure 3.20. In this way we can obtain

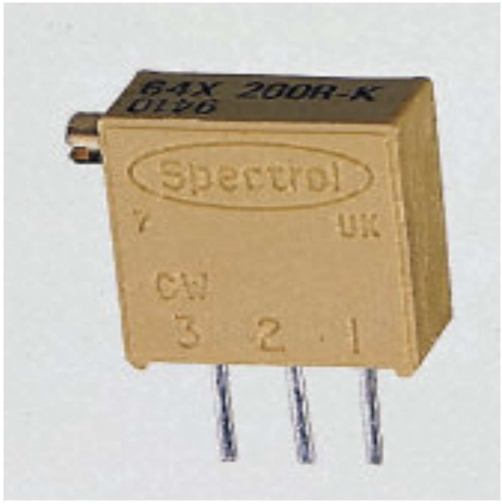

Figure 3.19: Trimmer.

a resolution of 1Ω over the range from 0 up to 11kΩ, that is, recallig Figure 3.5, a tunable inductor form 0 to 330H with a resolution of 0.033H. The circuit prototype has been tested in order to verify its applicability (results will be given in the next section). Once verified that this circuit satisfies the project restrictions, it has been designed with Protel 99 SE and then realized in series. A scheme of the realized circuit is shown in Figure 3.23

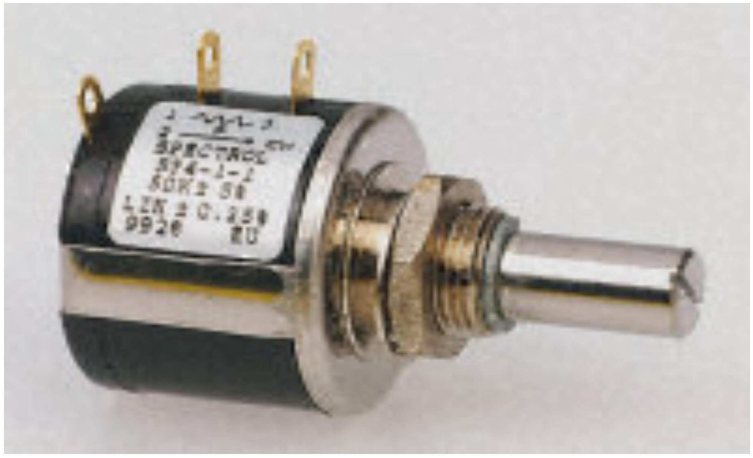

Figure 3.20: Potentiometer.

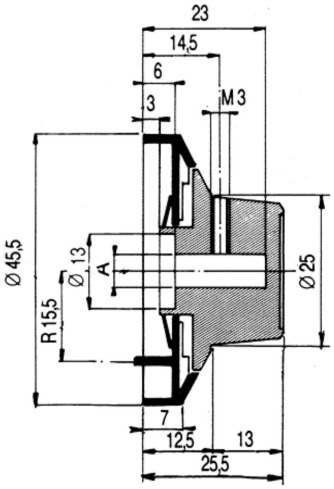

Figure 3.21: Selector.

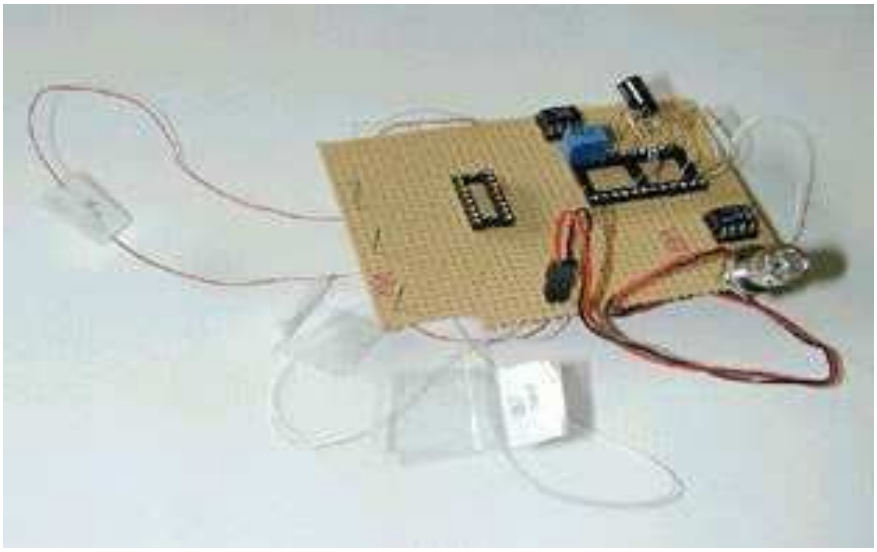

Figure 3.22: First prototype of the circuit.

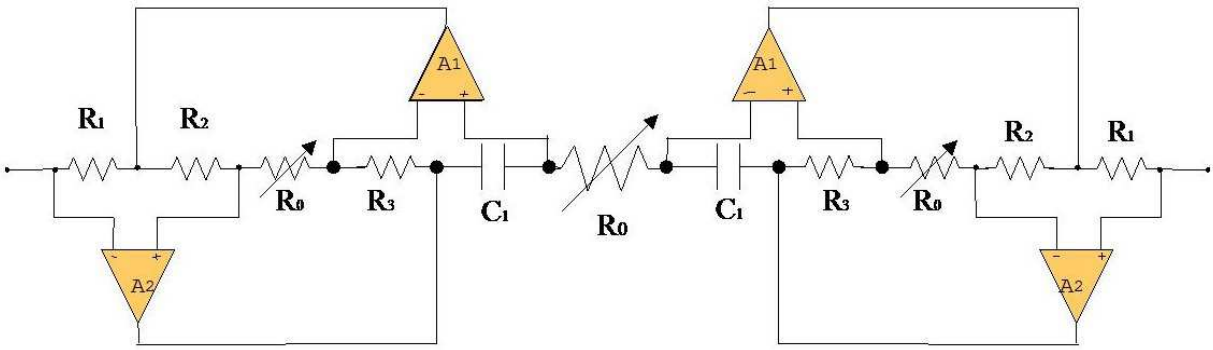

Figure 3.23: Floating inductor scheme.

3.5.1 Synthetic Inductors Characterization

The values of the equivalent resistance and inductance of the synthetic inductor in Figure 3.13 have been extrapolated by frequency response measurements of the assembled resonant circuit once a series connection with a known capacitance and resistor is realized.

The measurements are shown in Figure 3.24.

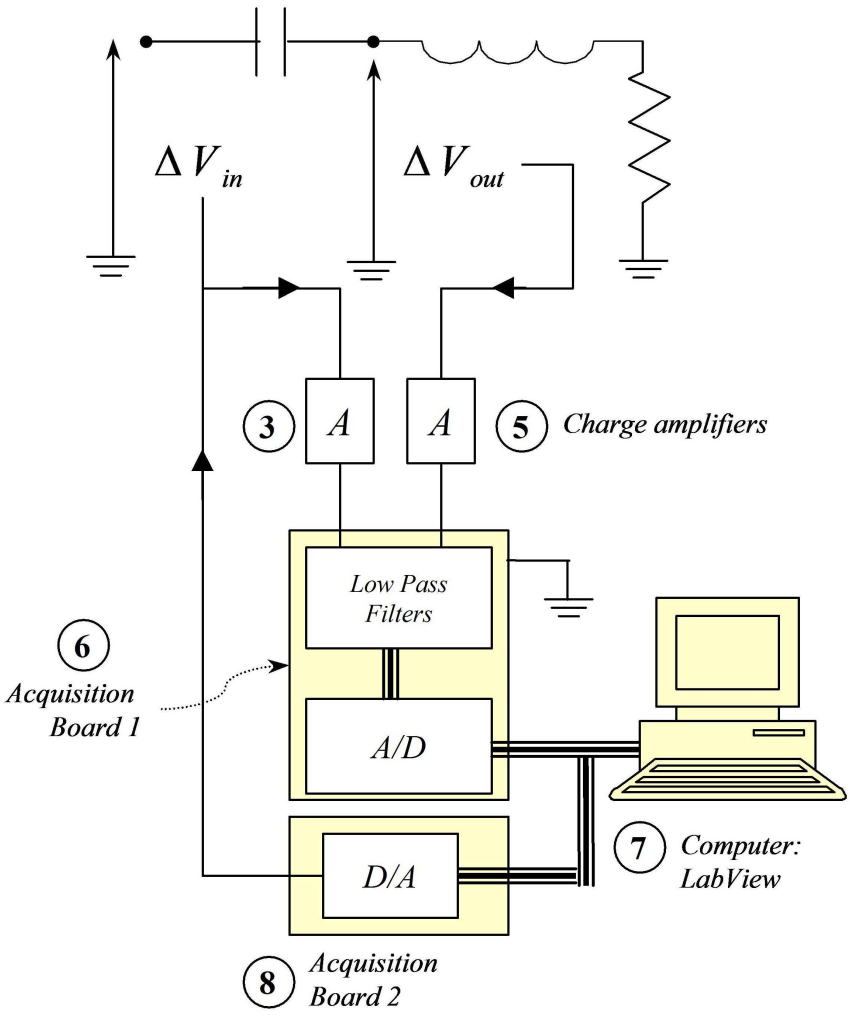

Figure 3.24: Inductor testing setup.

The resonant frequency and damping ratio have been deduced with the same procedure followed for the mechanical beam and will be discussed further. The equivalent inductance and resistance as a function of the variable resistors R and R_0 are reported in Figures 3.25 and 3.26, respectively. A linear interpolation of the experimental data is presented.

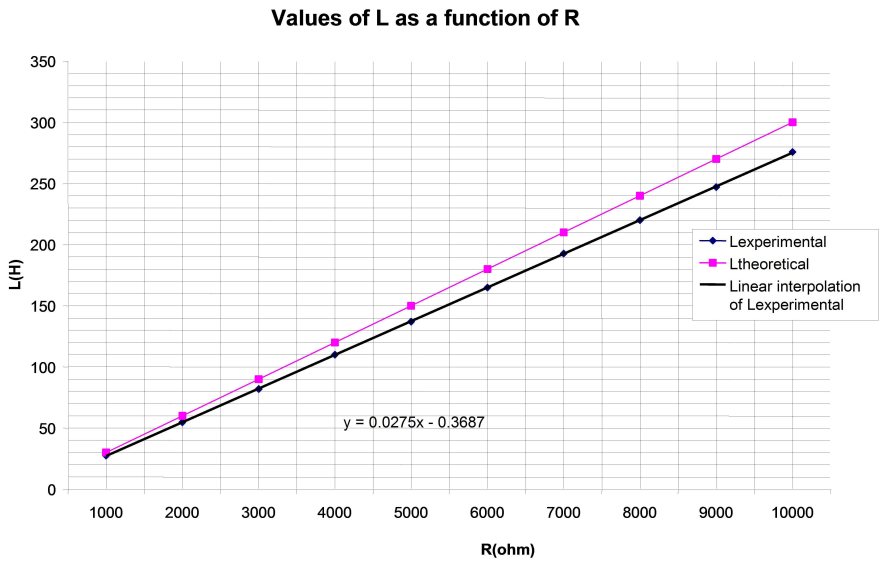

Figure 3.25: Synthetic inductor: experimental and theoretical.

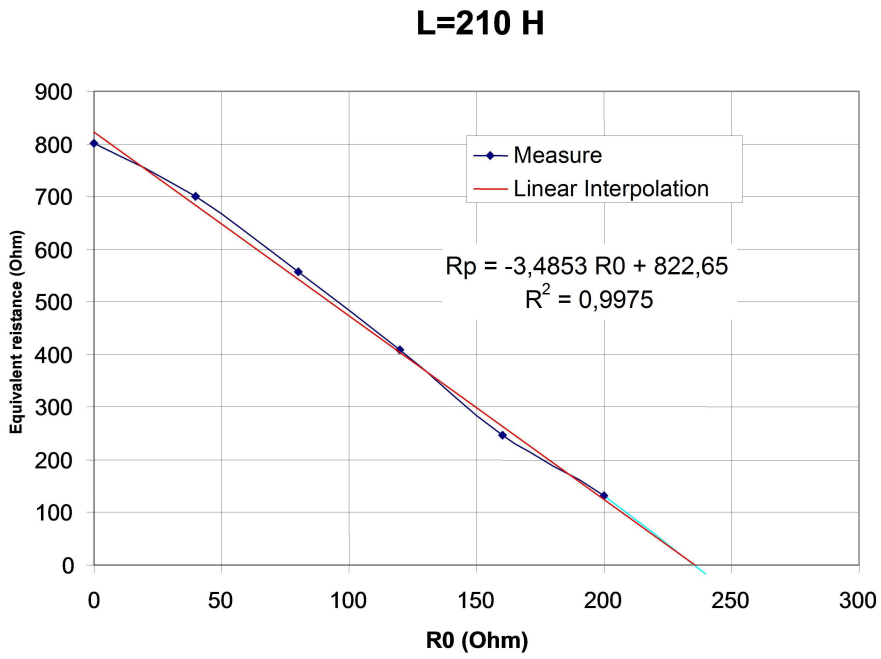

Figure 3.26: Effect of R_0 on the parasitic resistance for a fixed equivalent inductance $L =$ 210H.

3.5.2 Resistor realization

The value of the resistor to be connected in parallel with the inductor has been realized (as for the resistor that fixes the inductor value) with a series connection of a trimmer 0-100kΩ and a high precision potentiometer of 10kΩ that with a variable selector, Figure 3.21, has a resolution of 10Ω. We thus obtain a potentiometer from 0 to 110kΩ with a resolution of 10Ω.

Chapter 4

Experimental validation

The main goal of the experimental work is the validation of the numerical and analytical results obtained about the effectiveness of a distributed piezoelectric coupling between a structure and an electric network for the broadband passive control of mechanical vibrations. The final objective is to build prototypes to experimentally compare the performances of the following systems:

1. A beam coupled with a resonant RLC circuit by means of a PZT transducer
2. A beam coupled with n separated RLC circuits by means of a periodic array of PZT transducers (see Figure 6.6)
3. A beam coupled with the lumped version of a second order transmission line by means of a periodic array of PZT transducers (see Figures 1.4 and 7.2)

Other objectives are:

1. To test technological solutions using PZT materials
2. To develop and test both an experimental setup and an identification procedure for the extraction of the modal parameters of electromechanical systems
3. To build and characterize a pinned-pinned beam with five pairs of PZT transducers in bimorph configuration to be used in a series of future experiments
4. To realize and characterize the electronic devices needed to assemble the electrical networks

4.1 Modal testing

In order to test the system a standard single point excitation method has been used. The instruments used provide, for the particular measurements, high coherence data in an efficient way. The experimental setup has three major items:

i) An excitation mechanism

ii) A transduction system (to measure various parameters of interest)

iii) An analyzer to extract the desired information

Figure 4.1 shows the layout of the measurement system.

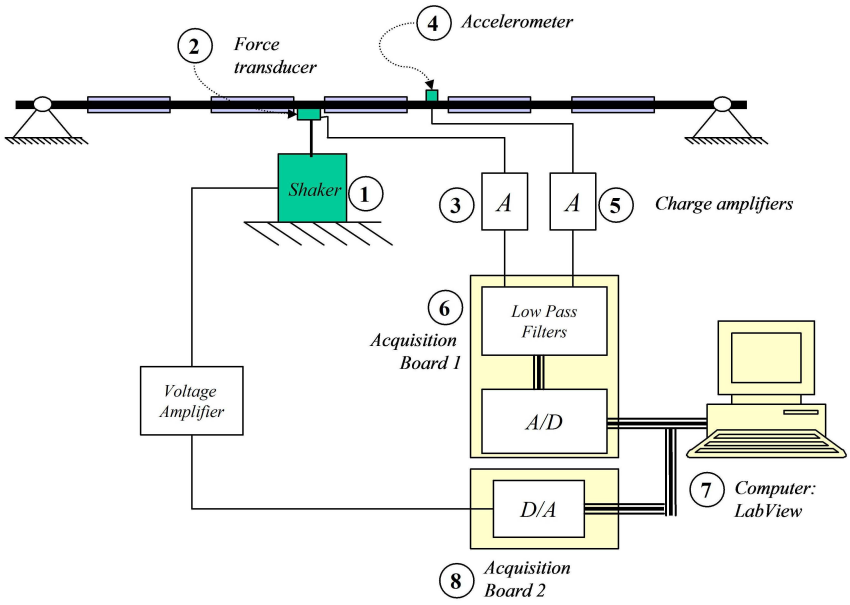

Figure 4.1: FRF measurements setup.

As we can see the items of this system are:

(a) An electric source that provides the excitation signal. The frequency sweep digital signal generated by the computer with a MATLAB tool is driven in a digital-analog converter that produces an analog signal and provides the amplification necessary to drive the actual device used to vibrate the structure.

(b) The exciter is an electromagnetic shaker in which the supplied input signal is converted to an alternating magnetic field in which is placed a coil that is attached to the drive part

of the device, and hence to the structure. It must be noted that it is not appropriate to deduce the excitation force by measuring the current passing through the shaker because this measures the force applied not to the structure itself but to the assembly of the structure and shaker. Although it may appear that the difference between these forces (generated within the shaker and applied to the structure), could be small, it must be noted that near the resonance very little force is required to produce a large response. Thus, near this frequency, there is a marked reduction in the force level. As a result the true force applied to the structure becomes the small difference between the force generated by the exciter and the inertia force required to move the drive rod. So it is necessary to make a direct measurement of the force applied to the structure as close to the surface as possible.

c) The force transducer measures the force applied to the beam. In particular, a piezoelectric force transducer was used. The basic principle of operation is that, by suitable design, the device induces in a piezoelectric crystal, incorporated in it, a stress proportional to the physical quantity to be measured, a force in this case. The piezoelectric crystal then produces an electric current proportional to the stress gradient and the signal that contains the information required is processed.

d) An accelerometer that has the same physical principle as the force transducer. Its function is to measure the acceleration of a certain point of the structure.

e) Frequency filters that remove the part of the signal that is out of the frequency range of interest in order to avoid problems that could invalidate the measurements.

The two signals measured, the excitation by the force transducer and the response by the accelerometer, are input to an analog-digital converter that provides a digital signal subsequently input into the analyzer, that is a PC with MATLAB tools. The PC processes the signal providing the final data such as the FRF response, the coherence matrix and the pole place.

We now state some features of the digital frequency analysis, faced during the experiments, that, if not properly treated can give rise to erroneous results. These are usually the result of the discretization approximation and of the limitation of the finite time history of the signal processed. With the discretization process the existence of very high frequencies in the original signal may well be misinterpreted if the sampling rate is too slow. In fact, such high frequencies will appear as low frequencies or, rather, will be indistinguishable from genuine low frequency components. Figure 4.2 shows how this can happen. The low frequency signal in Figure 4.2(a) produces exactly the same set of discrete values as the higher frequency signal in Figure 4.2(b).

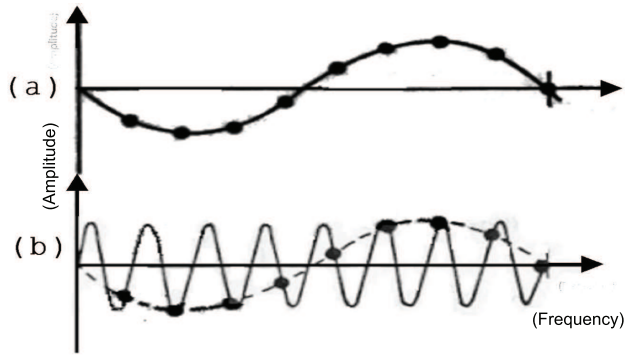

Figure 4.2: The phenomenon of aliassing.

This phenomena causes a distortion of the spectrum measured. In Figure 4.3(a) the true frequency content of the signal is shown, while in Figure 4.3(b), the distorted one. The distortion can be explained by the fact that the part of the signal which has frequency components above $\omega_s/2$ will appear reflected or 'aliased' in the range 0-$\omega_s/2$.

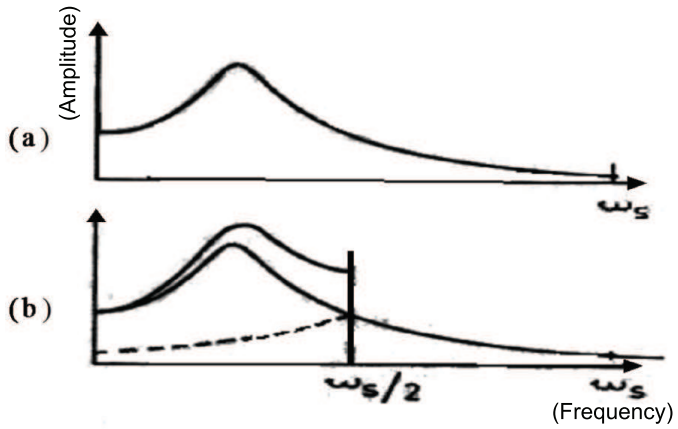

Figure 4.3: Distortion induced by aliassing.

The solution to this problem is to use anti-aliasing filters which subject the original time signal to a low pass filter with the characteristic of the form shown in Figure 4.4.

As we can see, these forms are inevitably less than perfect, and have a finite cut-off rate; for this reason it is necessary to reject the spectral measurements in a frequency range

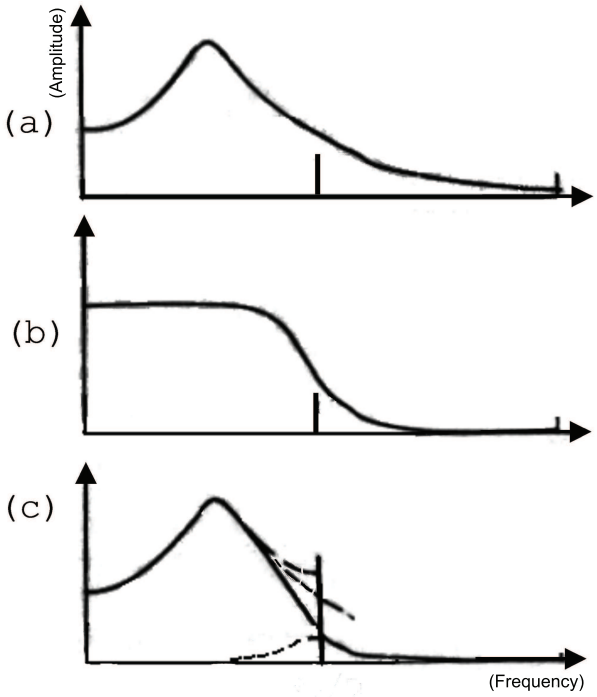

Figure 4.4: Anti-aliassing filter process.

approaching the so called Nyquist frequency[1], $\frac{\omega_s}{2}$. Typical values for this reject range vary from $0.5 - 1.0\frac{\omega_s}{2}$ for a simple filter to $0.8 - 1.0\frac{\omega_s}{2}$ for a more advanced filter design.

Leakage: this is a problem related to the need to take only a finite length of time history of the signal, with the assumption of periodicity in the rest of the history. This problem is illustrated in Figure 4.5. In case (a) the signal is perfectly periodic in the sampling time T, and the resulting spectrum is a simple line. In case (b) instead, the periodicity assumption is not strictly valid and there is a discontinuity implied at each end of the sample. As a result, the spectrum produced for this case does not indicate the single frequency of the original time signal. Energy has been leaked into a number of spectral lines close to the true frequency and the spectrum is spread over several lines. One practical solution to the leakage problem involves the use of windowing. Windowing involves the imposition of a prescribed profile on the time signal prior to performing the Fourier Transform and the profiles or 'windows' are generally depicted as a time function, $W(t)$, as shown in Figure 4.6 . There are different windows for different classes of problems. The Hanning (b) or Cosine Taper (c) windows are typically used for continuous signals, such as produced by steady periodic or random vibrations, while the Exponential window (d) is used for transient vibration applications where much of the important information is concentrated in the initial part of the time

[1]The Nyquist frequency is the lowest sampling frequency that allows the sampled signal to be reconstructed fully. If B is the band of the signal the Nyquist frequency ν=2B.

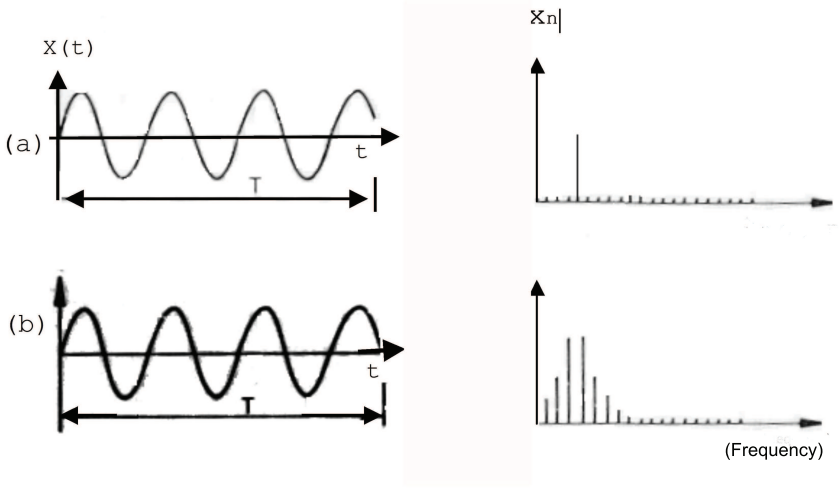

Figure 4.5: Sample length and leakage spectrum.

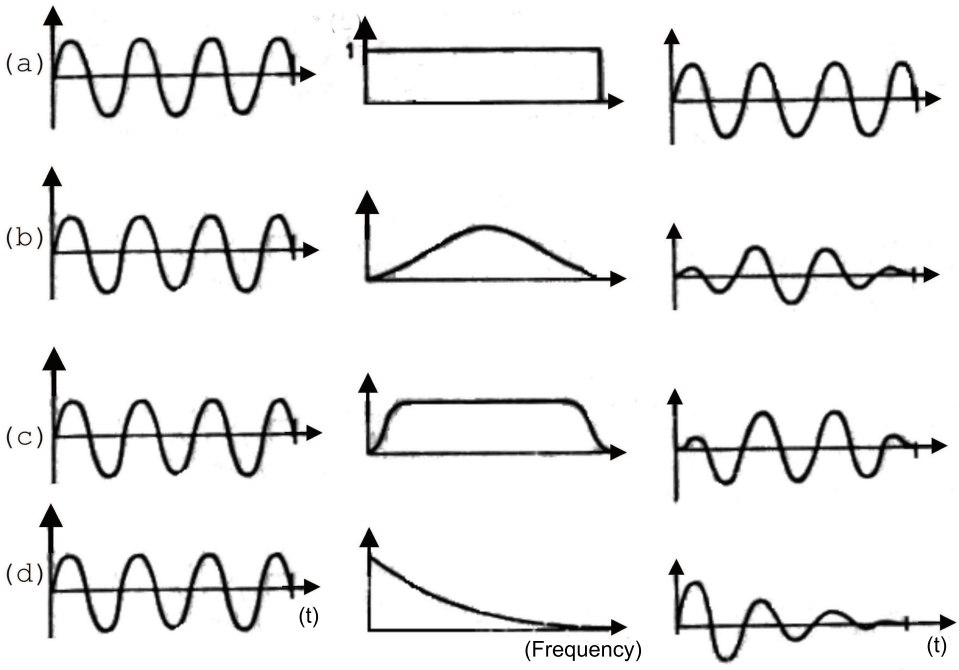

Figure 4.6: Different types of window.

record and would be suppressed by either of the above choices.

4.2 Modal Analysis

Mechanical and electrical dynamical measurements were taken in a frequency range from 25 to $45Hz$ (around the first resonance frequency of the beam, 35Hz) following the standard modal analysis techniques. The modal characteristics of the mechanical and the electrical systems were extrapolated from their frequency response by means of an identification procedure. Here the peculiarities of the experimental apparatus and of the measurement procedure will be emphasized, referring to [20] and [21] for details about the subject.

4.2.1 Instrumentation

4.2.1.1 Hardware

For the dynamical measurements the following instrumentation hardware has been used:

1. Piezoelectric accelerometer *Bruel&Kier* 4393 with charge amplifier *Bruel&Kier* 2635
2. Force transducer *Bruel&Kier* 8200 with charge amplifier *Bruel&Kier* 2635
3. Electromagnetic shaker *Bruel&Kier* 4809 with power amplifier *Bruel&Kier* 2700
4. Analog two channel oscilloscope $Hameg\ 203-5$
5. Personal computer, processor AMD-K6 266 MHz,64 MB Ram, equipped with
   (a) A/D converter National Instruments $PCI-4452$ (Basic technical data in Figure 4.7, more information on *www.ni.com*)
   (b) A/D and D/A converter National Instruments $AT-MIO-16E-10$ (Basic technical data in Figure 4.7, more information on *www.ni.com*)

4.2.1.2 Software

A personal computer has been utilized for the management of the digital input and output and the signal processing. In an unique LabView code the following Virtual Instruments were gathered

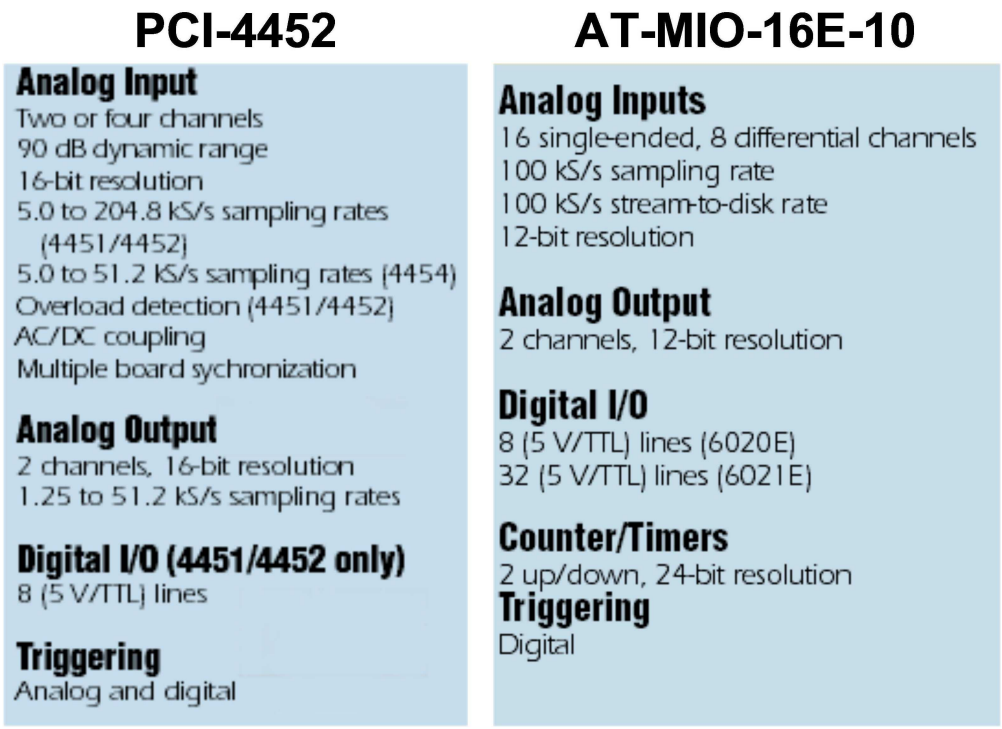

Figure 4.7: Acquisition and generation boards technical datasheets.

1. Sweep[2] generator
2. Anti-leakage windowing on the input and output signals
3. Spectrum analyzer
4. Frequency response analyzer

4.3 Experimental Setup for Mechanical and Electrical FRF Measurements

To get the frequency response of a physical system between an input and an output terminal we followed the procedure represented in Figure 4.8. Three fundamental logical phases can

[2]A sweep is a sinusoidal signal with a frequency linearly dependent on time. Its time representation is of the type

$$f(t) = f_0 \sin\left(\frac{\omega_2 - \omega_1}{T} t^2 + \omega_1 t\right)$$

It spans linearly the frequencies from ω_1 to ω_2 for t between 0 and T. It is a transient excitation signal frequently used in Experimental Modal Analysis to investigate the behavior of the system in an assigned frequency range.

be distinguished:

1. Excitation (input)
2. Measurements of the given input and the consequent output
3. Signal processing

The third is identical for mechanical and electrical systems, the other two are different. Indeed, if a mechanical system is considered, the electrical quantities must be transduced to mechanical ones for the excitation and vice-versa for the measurements[3].

The signal generation and processing has been implemented by means of a personal computer with a LabView code. A transient excitation method has been adopted for generating a digital *sweep* signal. The outputs of each measurement were the digital time signals, their FFTs, and the system FRF. Only the FFTs have been stored to extract from them the modal parameters by an identification procedure. We describe below the details of the mechanical and the electrical experimental setups separately.

4.3.1 Mechanical Experimental Set up

The chain of measurement in Figure 4.9 has been utilized to obtain the frequency response of either a mechanical or an electromechanical beam[4] relative to a force input and an acceleration output. The structure has been excited by a shaker (1)[5] controlled through an amplifier by a digital input generated by the personal computer (7). For the Digital/Analog conversion the board $AT - MIO - 16E - 10$ (8) has been utilized. The shaker has been attached to the structure through a rod to limit the rotational stiffening in correspondence to the attachment point. The force effectively transmitted to the structure has been gauged with a force transducer (2). The output was measured by a piezoelectric accelerometer (4) attached with a thin layer of wax. The locations of the excitation and the response have been optimized to give the best results for the first mode of the simply supported beam, compatibly with the presence of the PZT patches and avoid particular positions for which some fundamental modes are automatically filtered out. Indeed, if one considers the spatial shape of the first mode, the force transducer has been placed where the rotation is the smallest, the accelerometer where the deflection is the greatest[6]. The two measured analog

[3]The signals are intended to be electrical. All physical quantities to be measured must be transduced to electric signals (if they are not) in order to process them.

[4]Indeed the same set up can be used for the beam and the beam coupled to an electric network by means of PZT transducers.

[5]The numbers refer to those in Figure 4.9.

[6]Obeying these criteria, the central position should be chosen. Unfortunately it is occupied by the PZT layers.

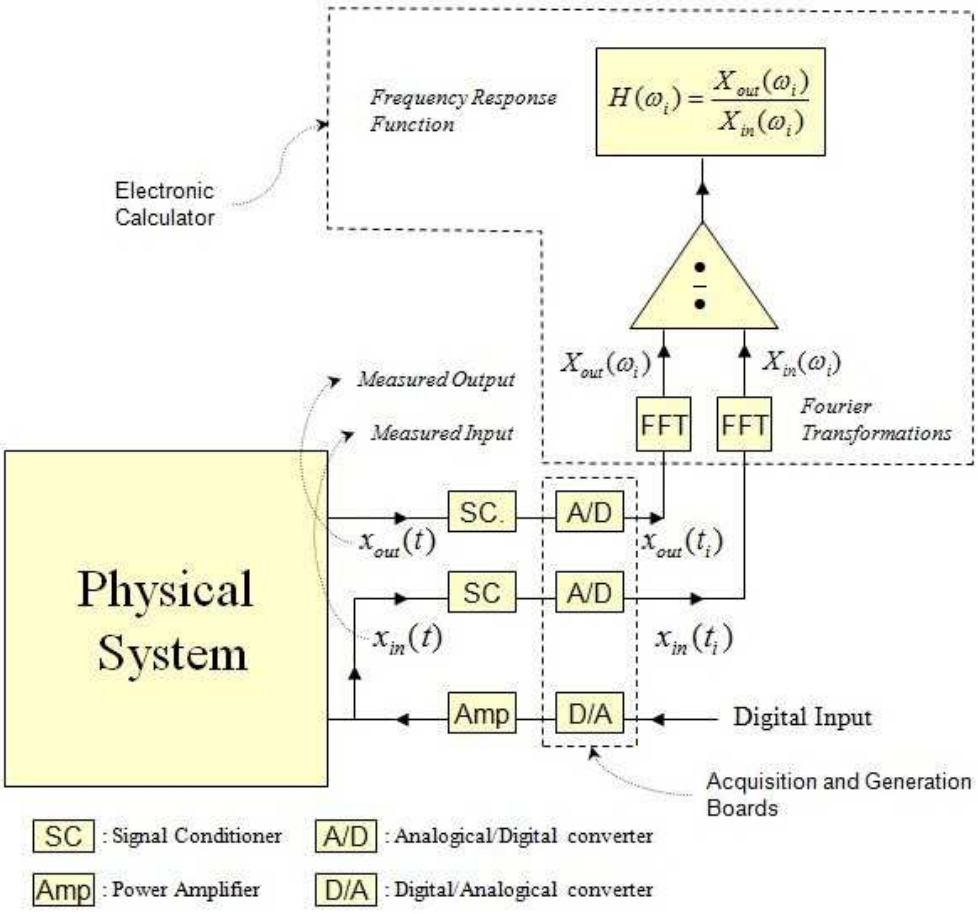

Figure 4.8: Logical scheme for Frequency Response measurements.

signals have been amplified and conditioned by two charge amplifiers (3,5). Then they were sampled using the board $PCI-4452$ in which both analog and real-time digital anti-aliasing filters are incorporated.

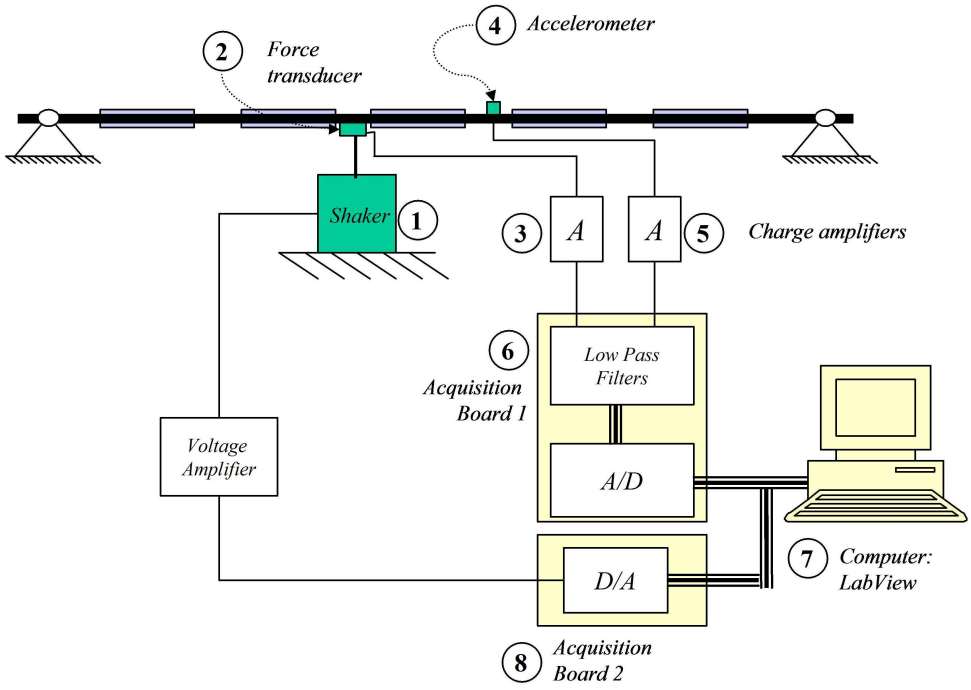

Figure 4.9: Experimental set up for mechanical FRF measurements.

4.3.2 Electrical Experimental set up

The experimental set up for the electrical measurements differs from the previous one only because no transducers are needed since the physical quantities to be measured and to be imposed are voltages. The frequency response of a RLC series circuit has been found as sketched in Figure 4.10.

4.4 Identification Procedure

From the frequency response, given as a complex scalar function defined on the frequency domain, the modal characteristics of the measured systems have been extracted. The averaged resonant frequencies and damping ratios were deduced with the respective confidence intervals from a series of N measurements taken under the same conditions and for the same

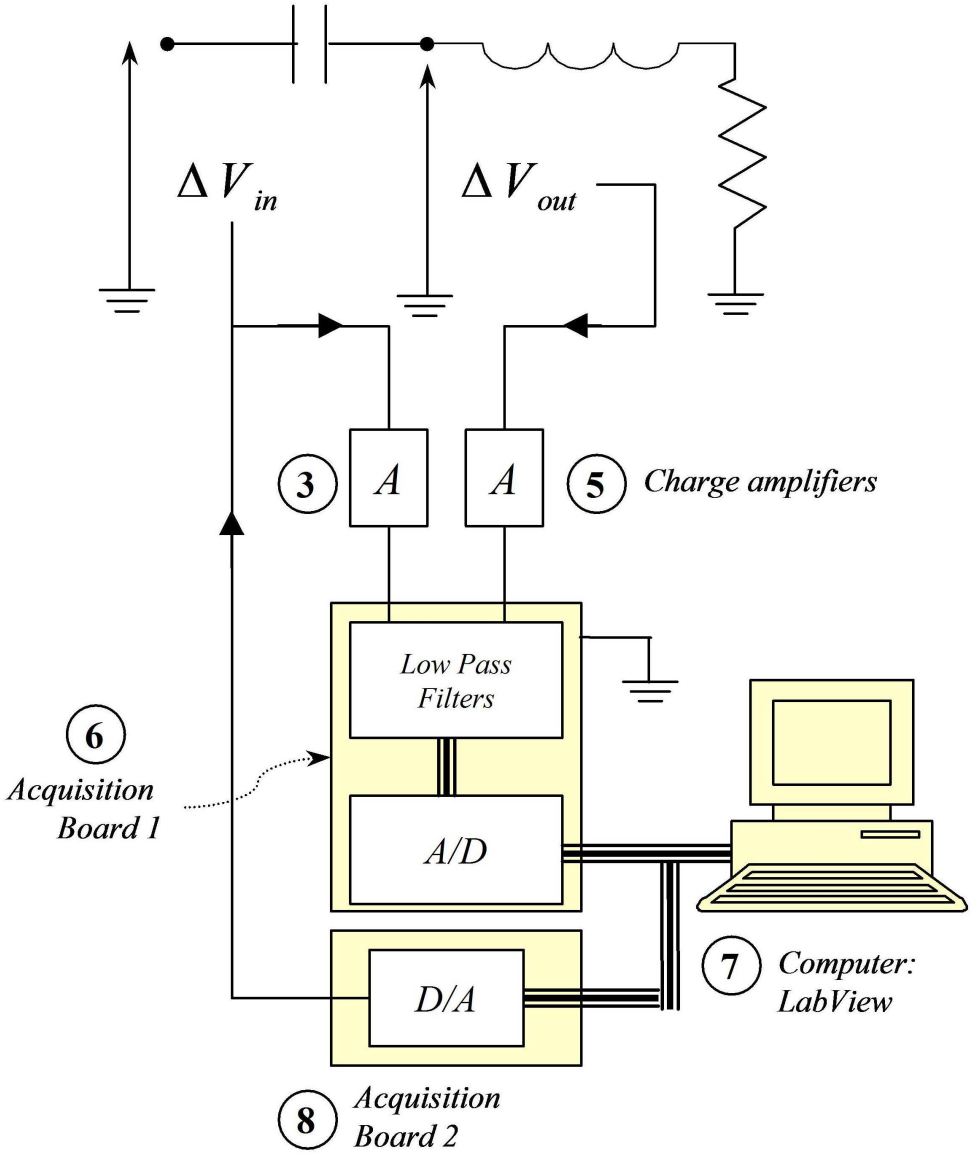

Figure 4.10: Experimental set up for electrical FRF measurements.

values of the acquisition parameters. The procedure followed is outlined in Figure 4.11. The following three main phases can be distinguished:

1. *Synchronization and Statistical Analysis* of the input and the output frequency domain data resulting from a set of N experiments taken with the same conditions. The data have been averaged calculating the empirical variances and input-output covariances. A foregoing synchronization is required to eliminate a residual phase shift between the measurements. This was done by minimizing the weighted phase differences of the complex amplitudes in the frequency domain by introducing a delay. In Figure 6.2 an example of the statistical analysis of the FRF experimental data for a simply supported beam is reported.

2. *Frequency Domain Identification* of each set of data and extraction of the resonant frequencies and damping ratios. This step has been implemented utilizing a MATLAB Toolbox. It requires as input the frequency domain data with an estimate of the variances and input-output covariances and the number of poles and zeros to be assumed for a Laplace domain form of the model in which the system must be identified. As outputs the estimated poles and zeros are given. The real and imaginary parts of each complex conjugate pair of poles can be easily converted to the corresponding natural frequency and damping ratio. This procedure has been repeated for the N sets of measures. An example of the output of the MATLAB code is given in Figure 6.2 and 6.1.

3. *Statistical Analysis of the Modal Parameters* resulting from the N identifications. From the N sets of the extracted resonant frequencies and damping ratios the mean values of the modal parameters have been derived with the respective confidence intervals.

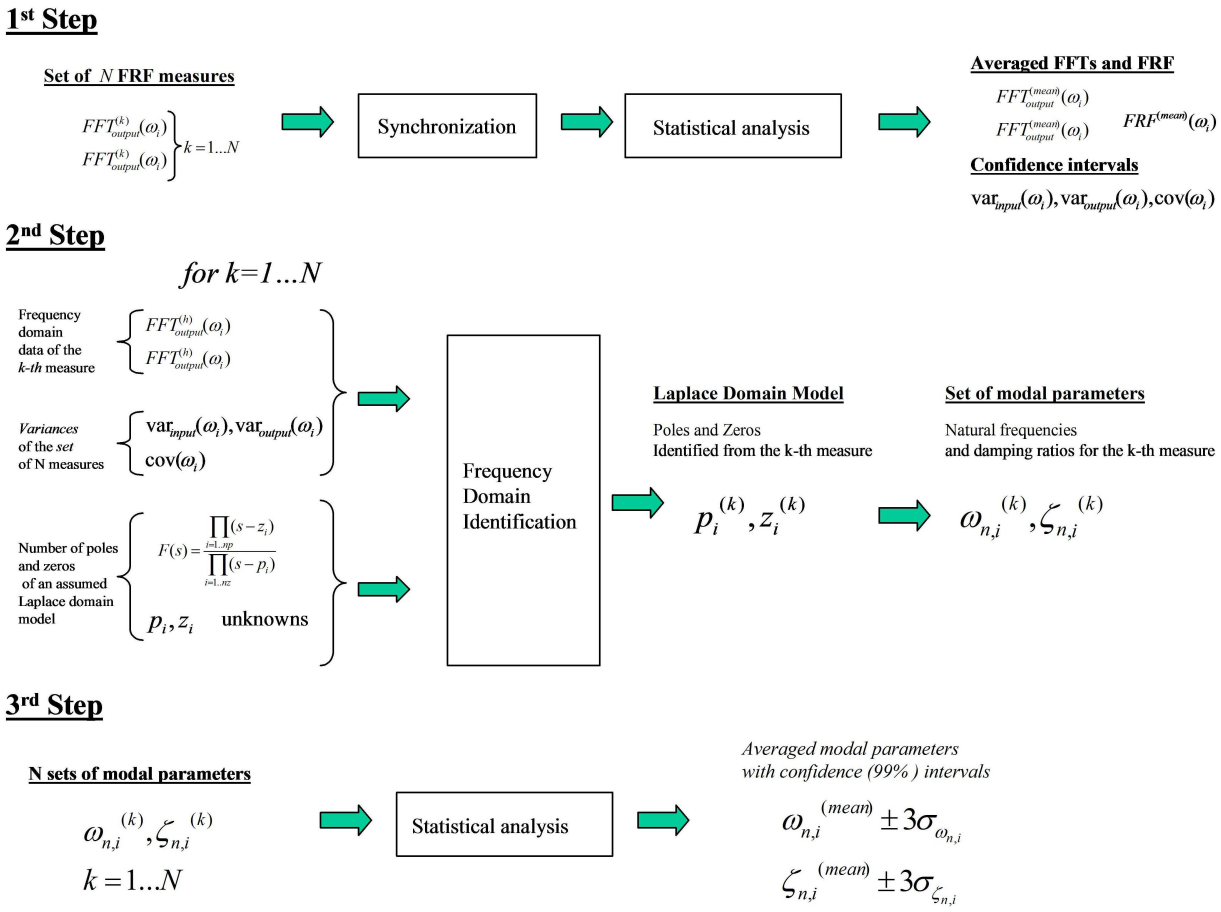

Figure 4.11: Identification procedure.

Chapter 5

Electrical-electrical response

The necessity to verify that the system had been realized accurately required us to measure the electrical-electrical frequency response. This type of measurement is very easy to perform and provides some useful information. Here the system is regarded as a five port electrical system, Figure 5.1, and the goal is to find its admittance matrix. The Y_{ij} element of the

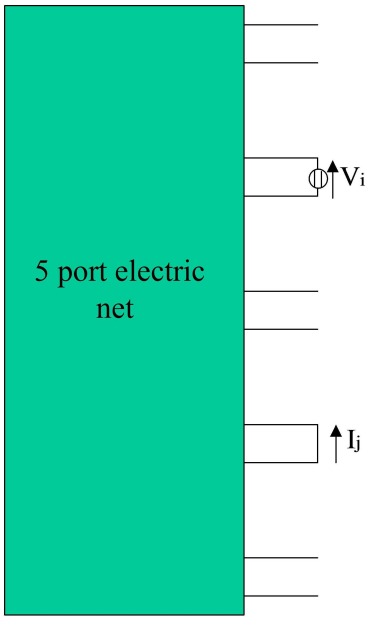

Figure 5.1: Five port electrical system.

admittance matrix is defined as the ratio between the current measured on the j-th port, that is short-circuited, and voltage applied on the i-th port, while the other ports are left open.

The impedance matrix becomes symmetric with respect to the two diagonals. The symmetry of the main diagonal is due to the geometric symmetry around the mid point of the beam, while the symmetry about the other diagonal is due to the reciprocity of the system. If the admittance matrix did not show these properties this would imply that the system is not symmetric as it has been modeled. Obviously this cannot give any information about the asymmetries; it could be related to the patches, a non equispaced placement for example, or to a different adherence of a patch, or perhaps to a damaged patch. It could be related also to the beam, that could be somewhere damaged and so non-homogeneous. In any case if the admittance matrix does not have the above stated symmetry properties, this would suggest to the experimentalist that the system to be tested has problems that need to be solved before proceeding with the experiments.

5.1 Experimental setup

Below we show the complete experimental system in Figure 5.2. An electrical signal, that is

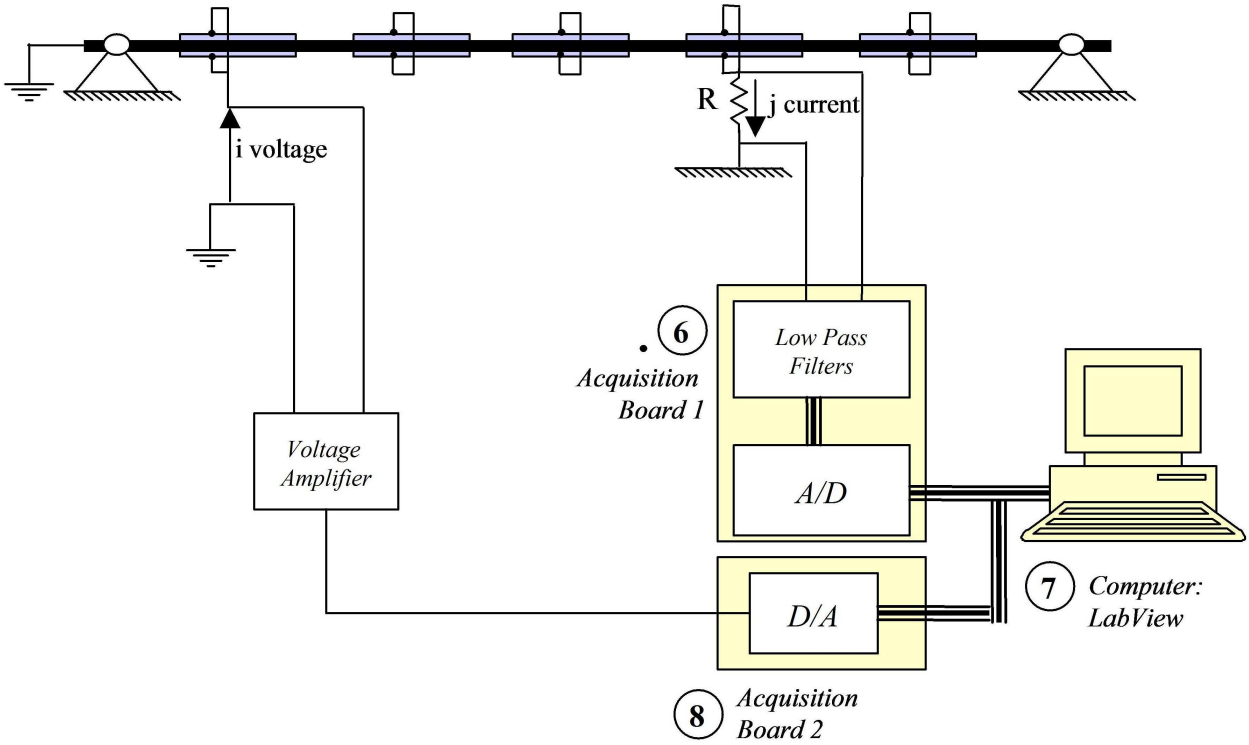

Figure 5.2: Admittance matrix measurement setup.

a frequency sweep from 120 to 1200 rad/s, is applied to a piezoelectric, while the electrical response, is measured by a second one. By this electrical response it is possible to obtain, as shown before (measurement section), the frequency response of the electromechanical system. Recall that in Y_{ij} the first index indicates the piezoelectric transducer where the signal is applied, the second one the transducer where the response is taken. Thus Y_{13} is the ratio between the current flowing in transducer three and the voltage applied on transducer 1, obviously in the frequency domain.

5.2 Results

We first analyze the diagonal element of the admittance matrix, Figures 5.3, 5.4 and 5.5.

As we can observe the agreement between the two measurements is good, but the first

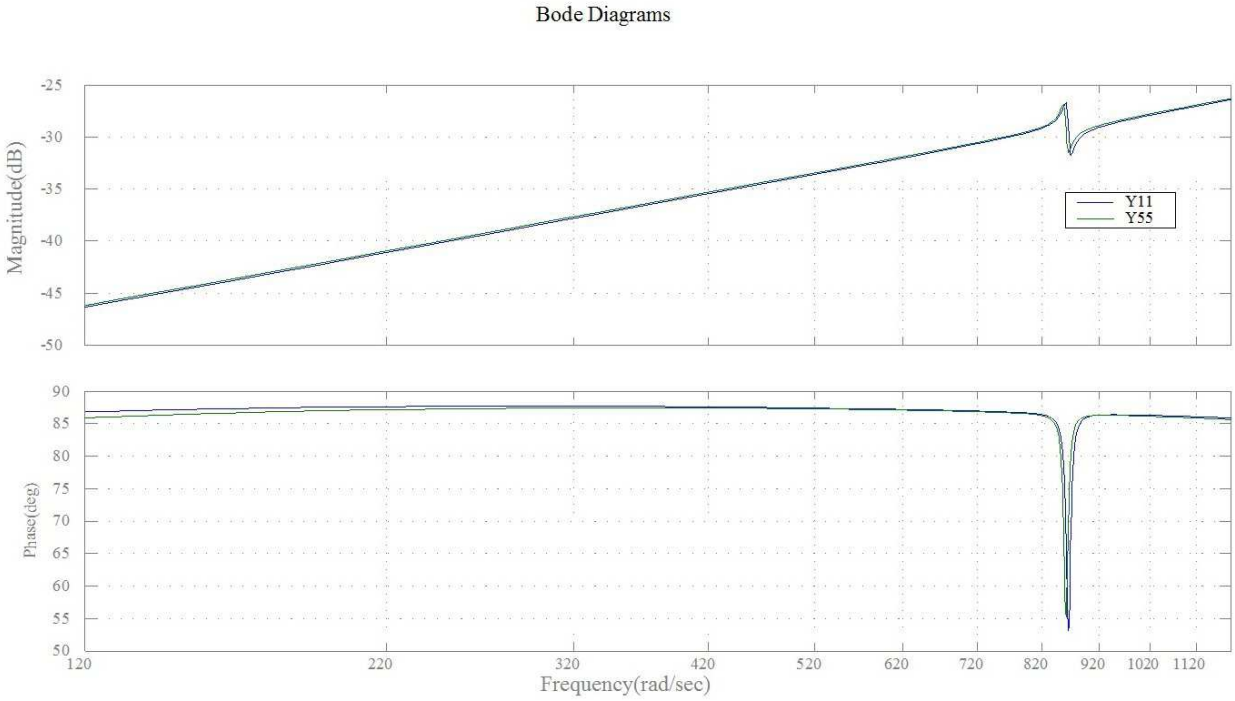

Figure 5.3: Admittance matrix: Y_{11}-Y_{55}.

mode is not observed, and this is strange since the position of transducers one and five are such that the first mode should be both excited and observed. This behavior is probably due to a measurement error. In fact, in order to perform the current measurement, we have modified the electrical circuit, Figure 5.1, with the insertion of a resistor R. Now if the impedance of this resistor is much smaller than that of the PZT circuit module, that is the capacitor in parallel with the controlled current generator, then it becomes negligible, and the current can be measured by the ratio of the voltage drop on this resistor and the resistor

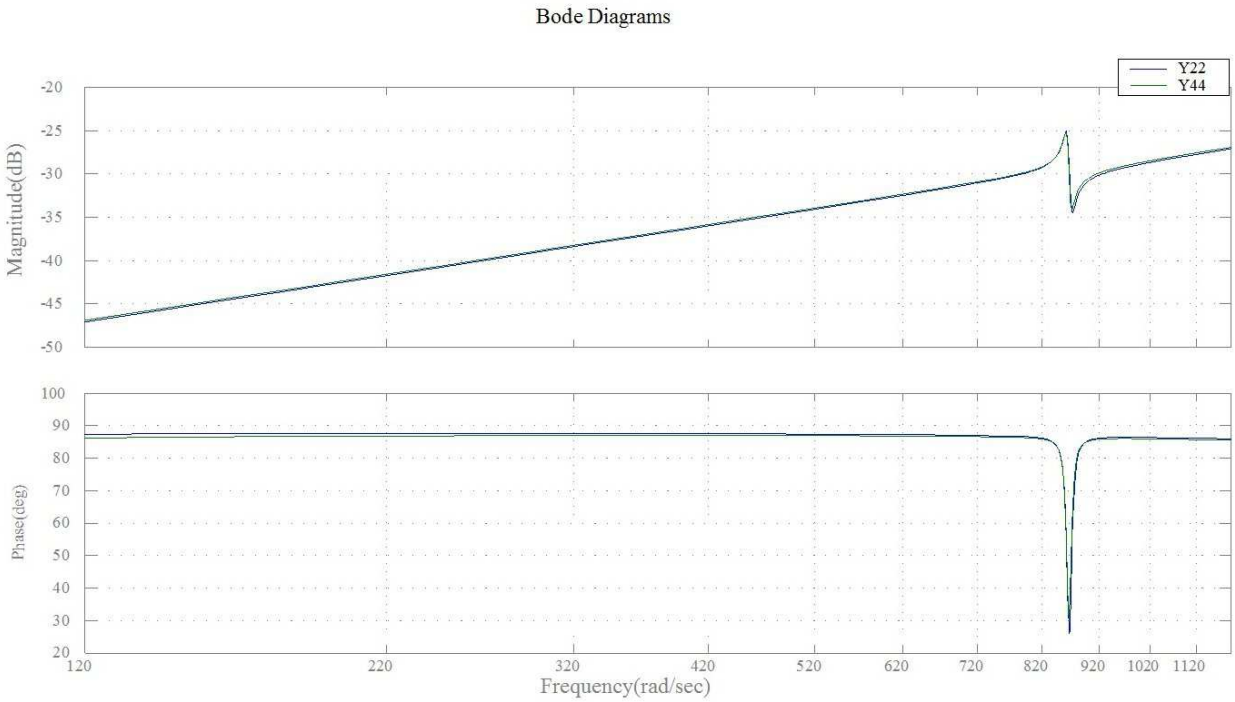

Figure 5.4: Admittance matrix: Y_{22}-Y_{44}.

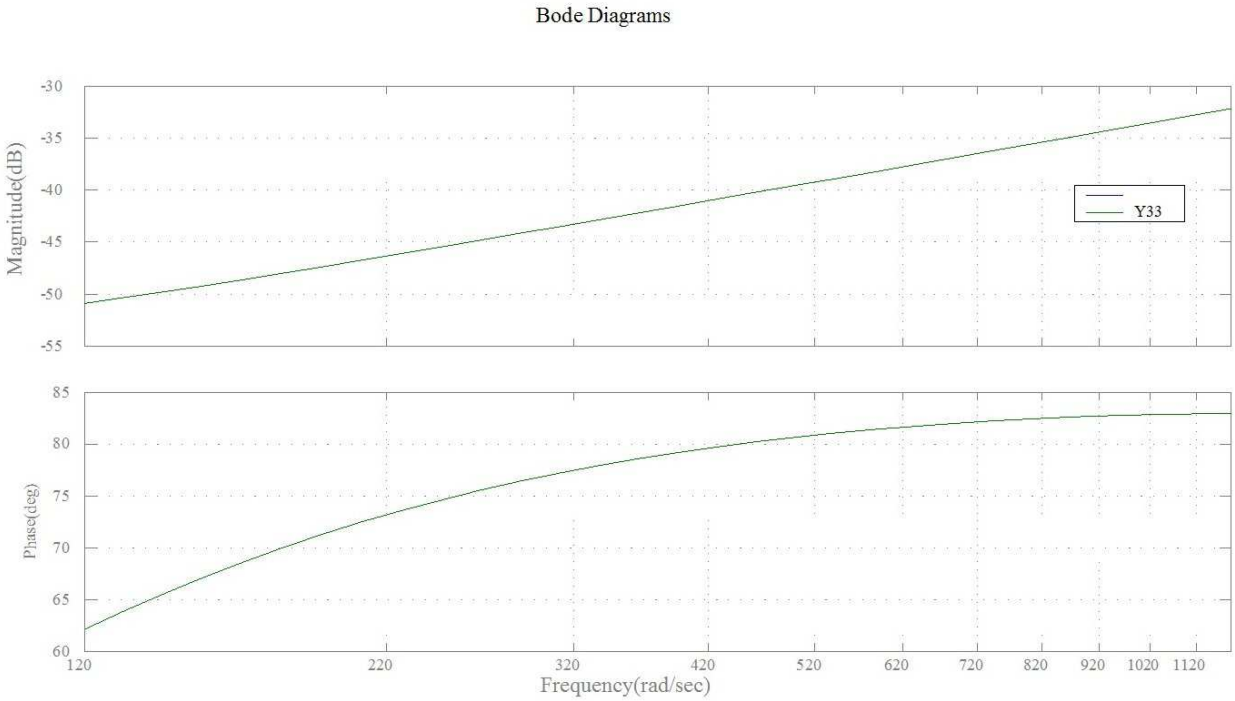

Figure 5.5: Admittance matrix: Y_{33}.

value. Unfortunately, near resonance, the value of the equivalent impedance of the controlled current generator becomes so small (this is feasible since near the resonance a little voltage can produce large deformations and hence large currents) that the resistor R, in order to be negligible, should reach values under the lower limit allowed by the available instruments. In fact, for a resistor smaller than 100Ω, the voltage drop across it becomes so small that the noise of the system significantly affects the measurement. In practice the signal could no longer be distinguished from the noise. In order to perform a correct measurement a better performing measurement system should be used, or, and this probably would be the best solution, the current measurement could be made by means of an amperometric coil, without the insertion of any resistor.

We now analyze the non-diagonal terms, Figure 5.6, 5.7, 5.8, 5.9, 5.10 and 5.11 .

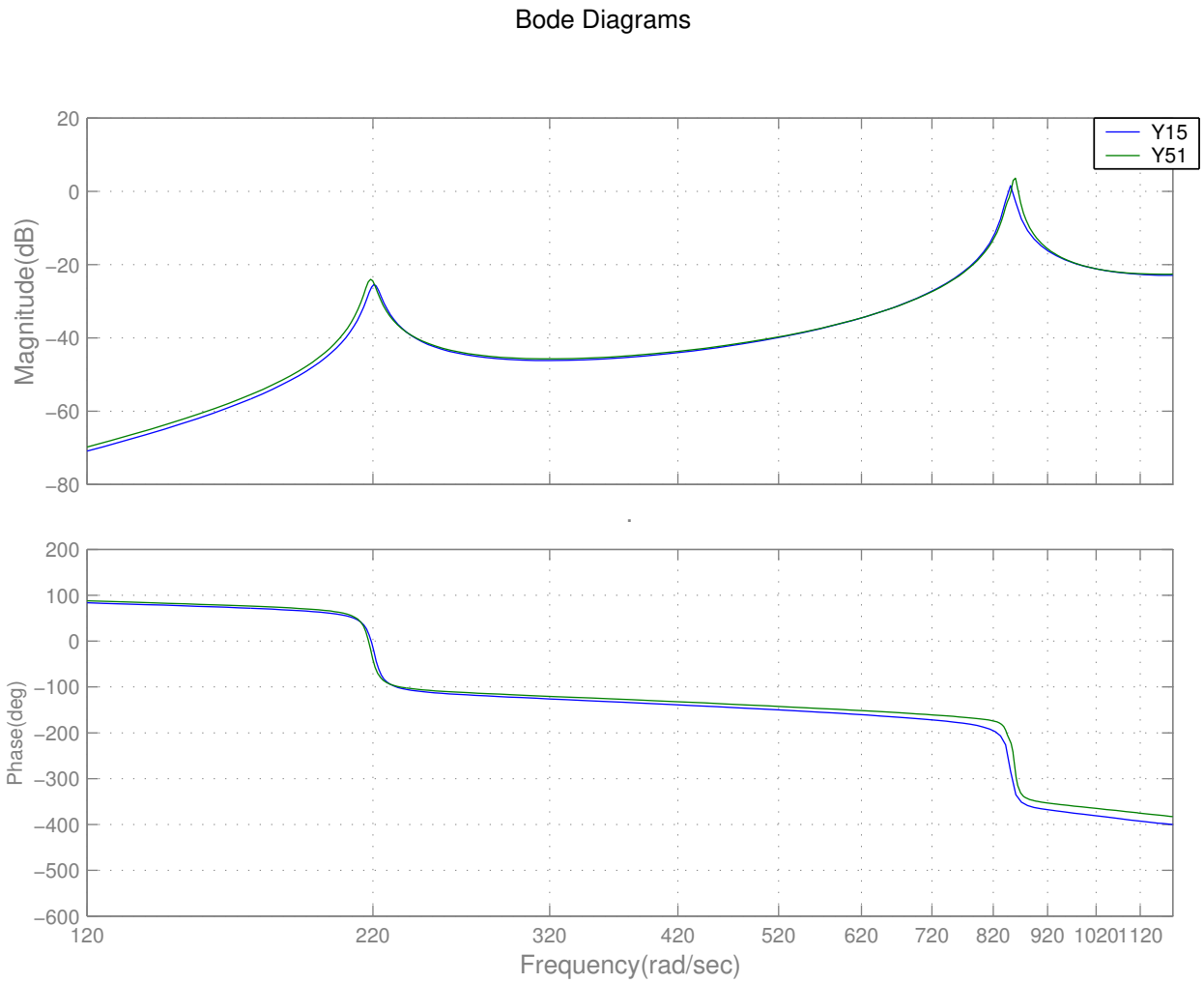

Figure 5.6: Admittance matrix: Y_{15}-Y_{51}.

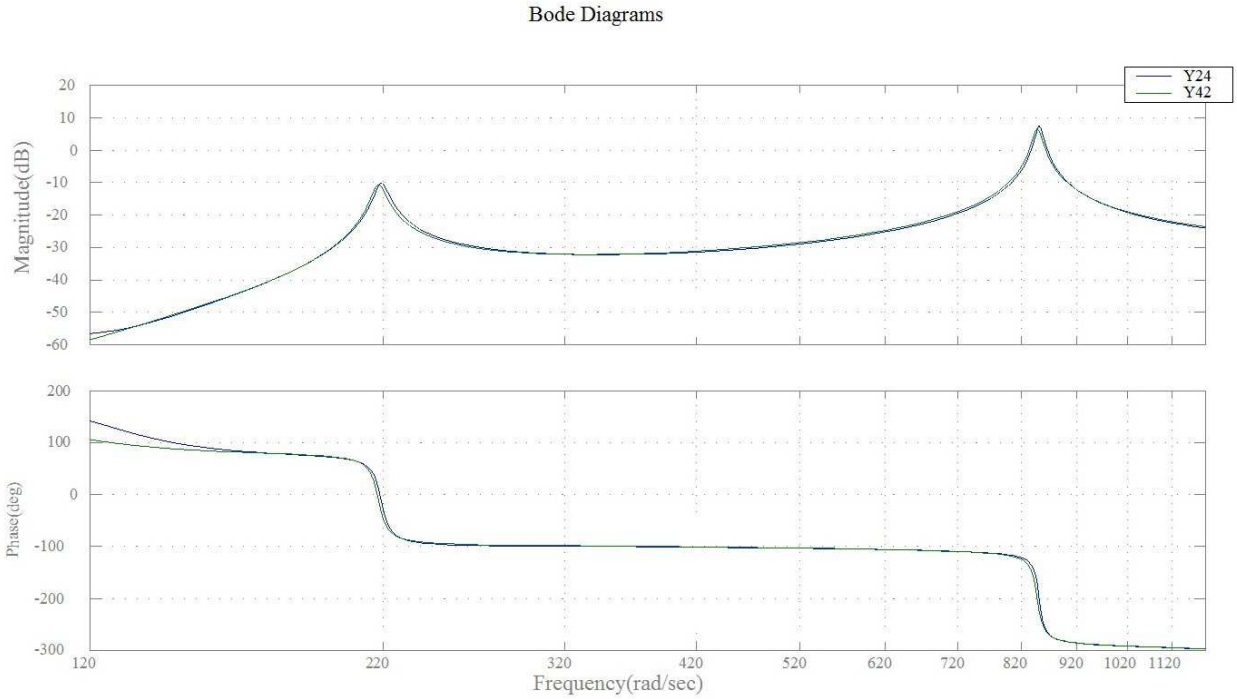

Figure 5.7: Admittance matrix: Y_{24}-Y_{42}.

In all these measurements, the agreement between the curves is fine except for the last two graphs (Figures 5.10 and 5.11) where it can be seen that there is a small difference in correspondence of the second mode. To explain this behavior, it must be noticed that in these the patch number 3 (the one in the middle of the beam) is always involved (once as actuator, once as sensor) and this patch is glued in correspondence with a node of the second mode. This means that theoretically (in the limit of small PZT patches) this mode should become unobservable if patch 3 is used as sensor, or uncontrollable if it is used as actuator [1]. In both cases the impedance should be pure resistive in correspondence to the second mode (smooth curve). In practice, however, the patch has a finite length, it extends over the node, so that the second mode is both controllable and observable, and in the impedance response function, a zero-pole close couple occurs (in the limit of small length they should cancel each other). In particular the reciprocal measurements (Y_{13}-Y_{31}, Y_{35}-Y_{53}, Y_{23}-Y_{32}, Y_{34}-Y_{43}, in Figures 5.10 and 5.11) have the same behavior, and this confirms the reciprocity of the system, while $Y_{13} - Y_{31} \neq Y_{15} - Y_{51}$ and $Y_{23} - Y_{32} \neq Y_{34} - Y_{45}$ means that the system is not geometrically symmetric. We should recall now that these measurements are meant to test the goodness of the system in a qualitative way, and in this sense they were useful to suggest that the experimentalist could proceed to the main experiment with the assurance that the piezomechanical system behaves properly. It must be observed, however, that this kind of measurement is in general a method for structural dynamic analysis. In particular, application of this approach to smart structures is presented in the area of mechanical frequency response function, structural modal analysis,

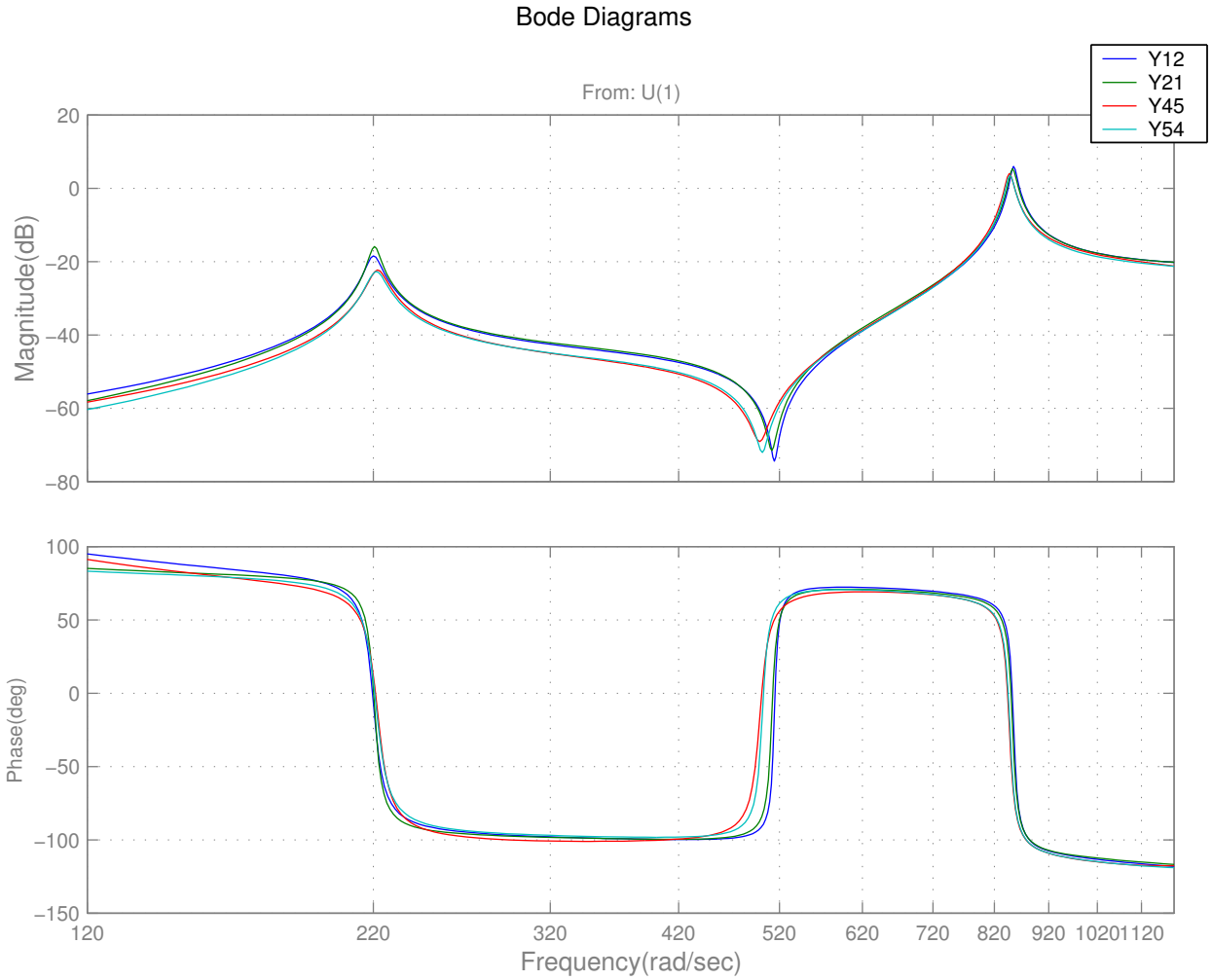

Figure 5.8: Admittance matrix: Y_{12}-Y_{21}-Y_{45}-Y_{54}.

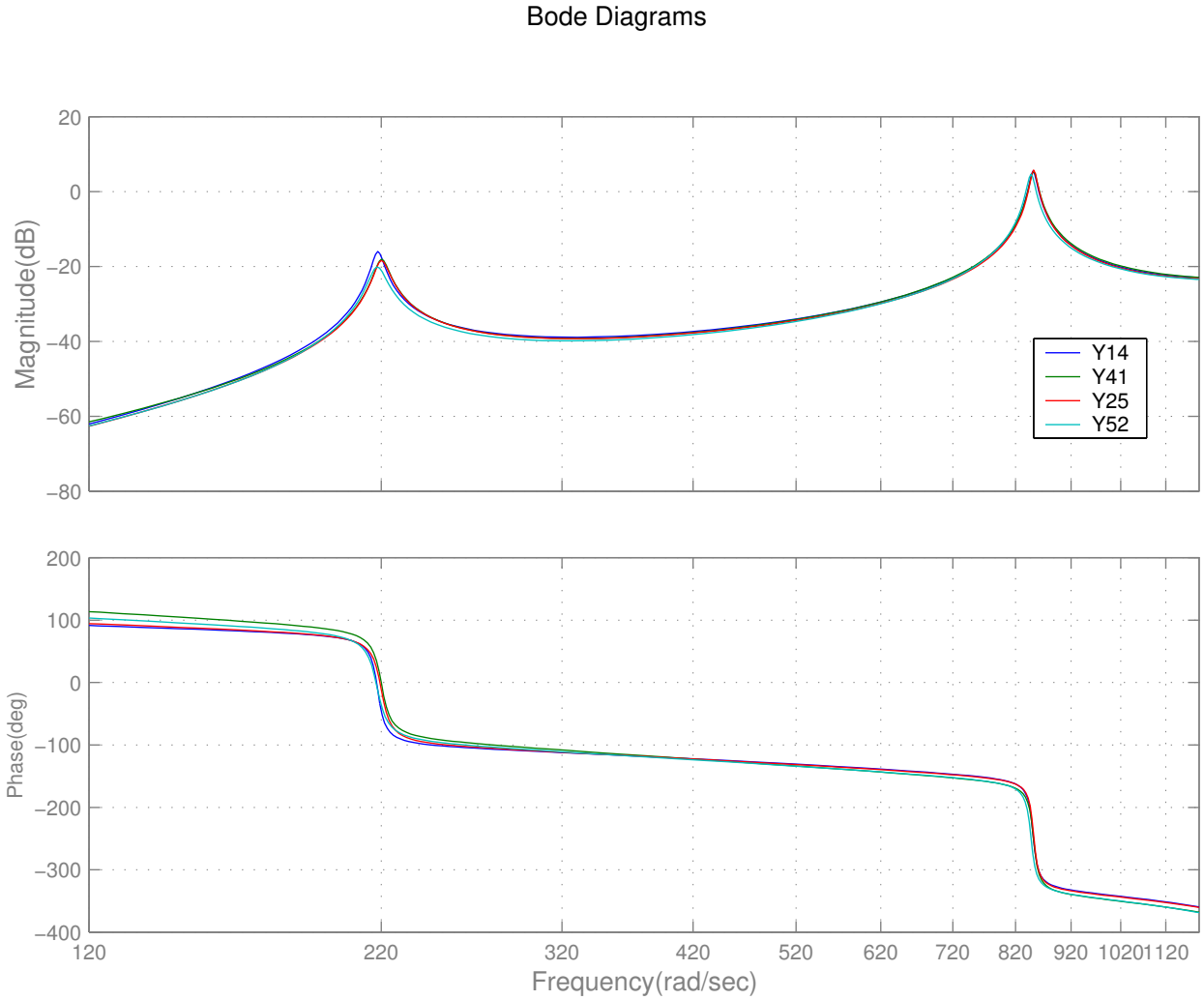

Figure 5.9: Admittance matrix: Y_{14}-Y_{41}-Y_{25}-Y_{52}.

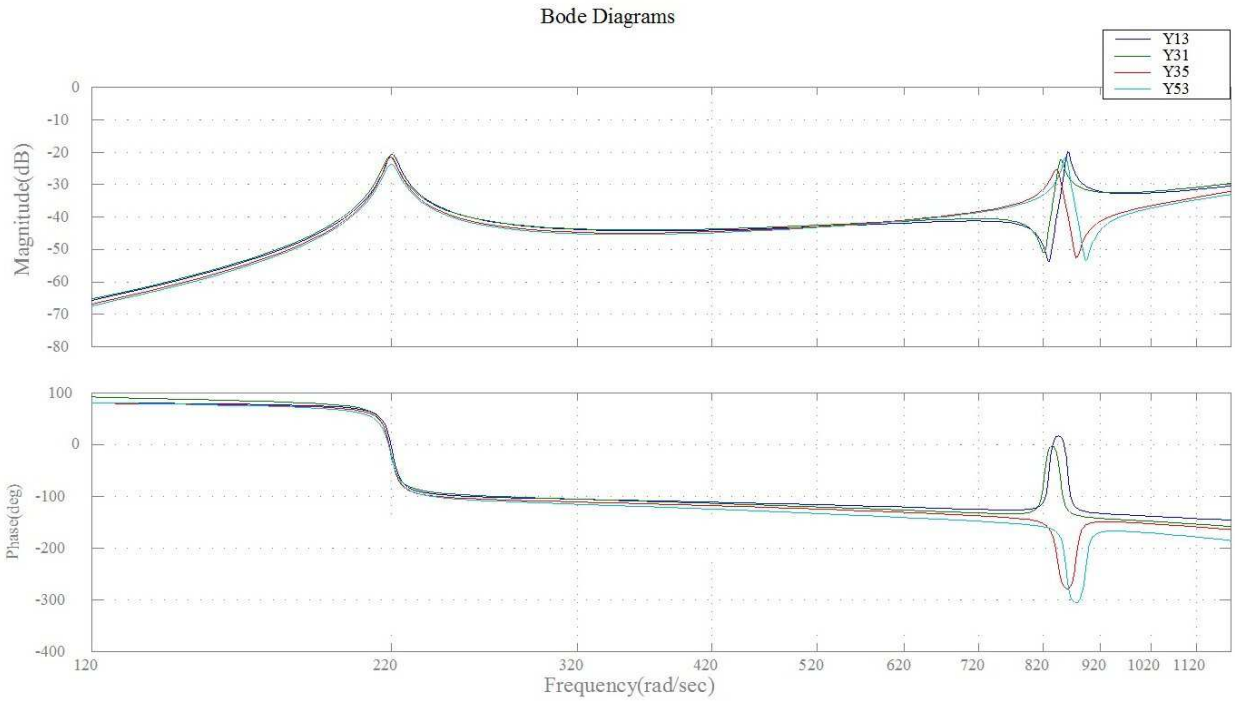

Figure 5.10: Admittance matrix: Y_{13}-Y_{31}-Y_{35}-Y_{53}.

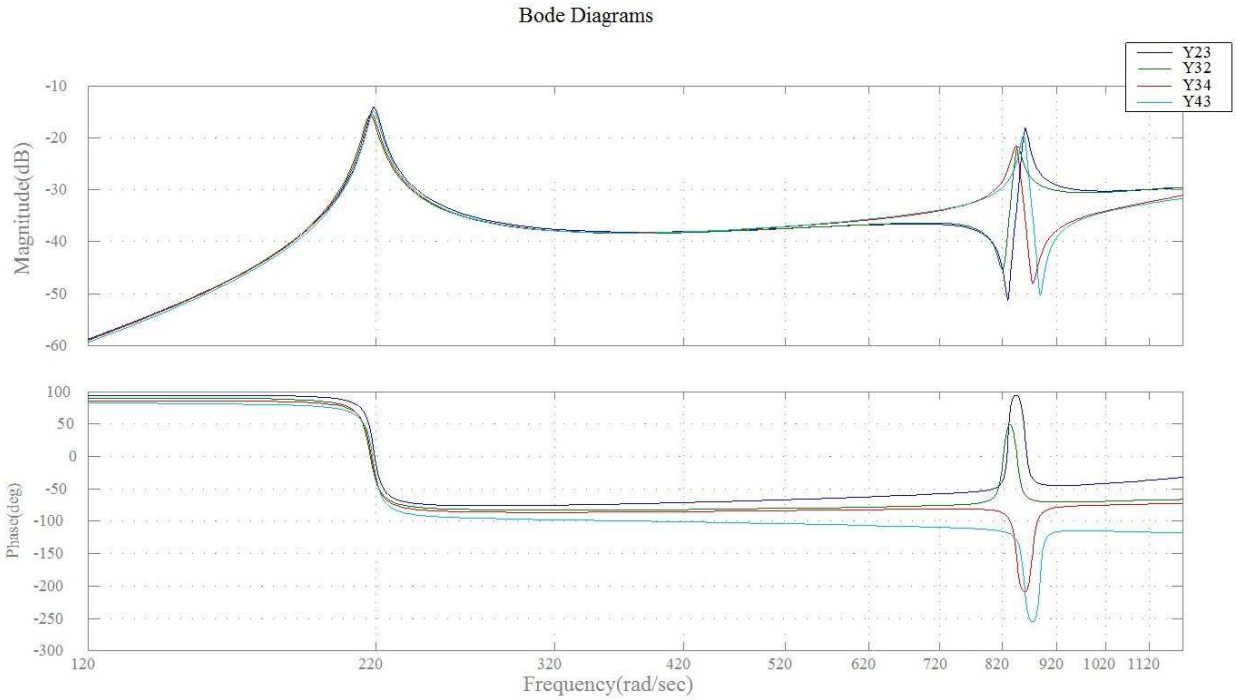

Figure 5.11: Admittance matrix: Y_{23}-Y_{32}-Y_{34}-Y_{43}.

and structural health monitoring.

Chapter 6

Mechanical-mechanical response

In order to test the quality of the measurement system, Figure 4.1, a simple modal test has been performed on the piezoelectromechanical beam with all actuators grounded.

The natural frequencies and damping ratios of the first three modes of the beam in Figure 3.1 without the PZT transducers have been found experimentally following the procedure outlined in previous sections. In particular the experimental setup in Figure 4.9 and the identification procedure in Figure 4.11 have been adopted. The following results have been found:

Mode	Natural Frequency (Hz)	Damping Ratio
1st	34.7414	0.10%
2nd	137.2162	0.26%
3rd	304.4973	0.24%

(6.1)

An example of the identification of experimental frequency response for one of the N measurements in the range from 10 to 400 Hz is presented is Figure 6.1 together with the extracted poles and zeros and the phase error between the measured data and the identified FRF (Figure 6.2).

6.1 Single shunted actuator

The second set of measurements have been performed on a single shunted actuator system. The main idea of coupling the first mode of the beam with the dynamics of a dissipative RLC circuit utilizing the piezoelectric transducer has been developed. Only the PZT four has been used, shunting it with a series connection of a resistor and a synthetic inductor.

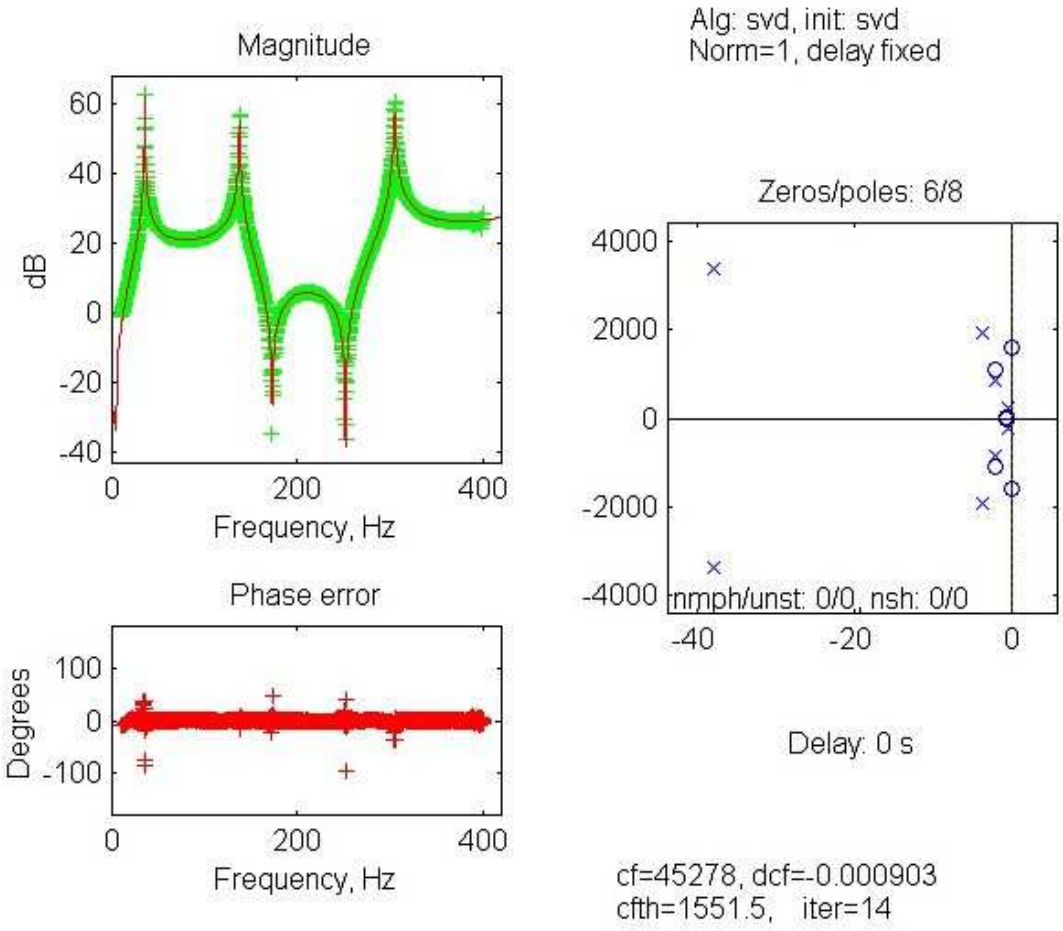

Figure 6.1: Results of the identification of the first three modes of the simply supported aluminum beam.

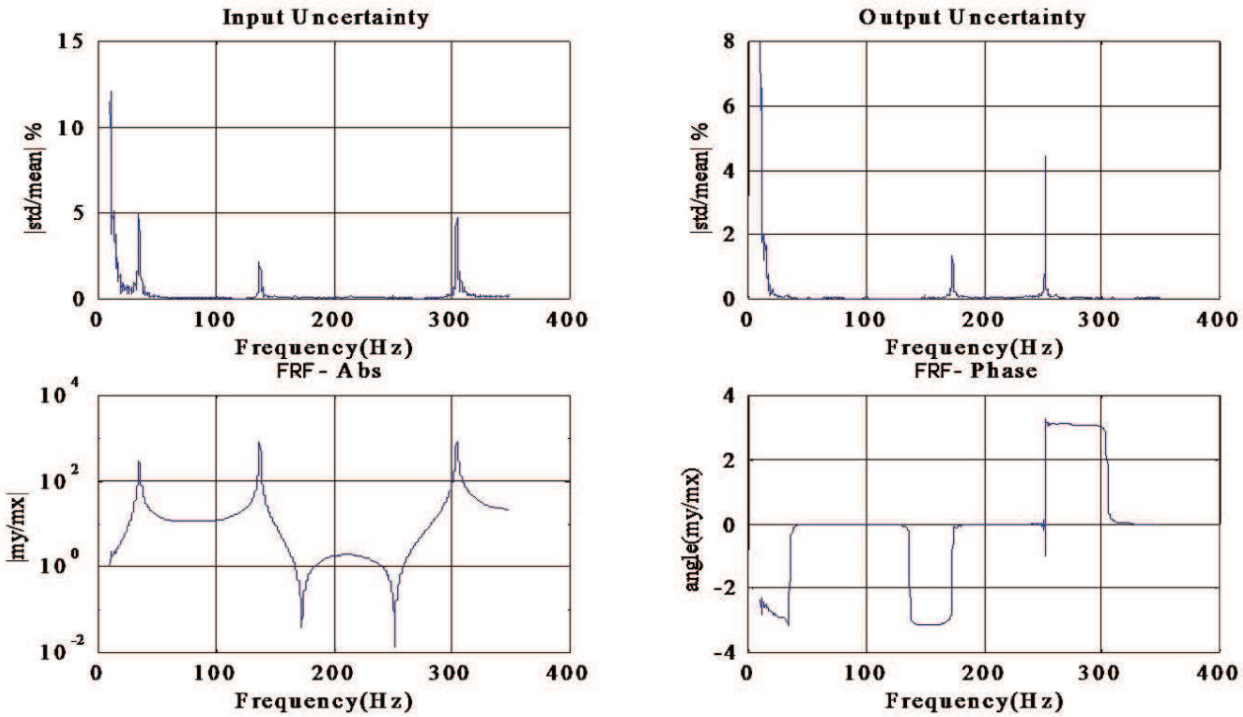

Figure 6.2: Statistical analysis on a set of 15 measurements of the beam FRF: mean values and uncertainties.

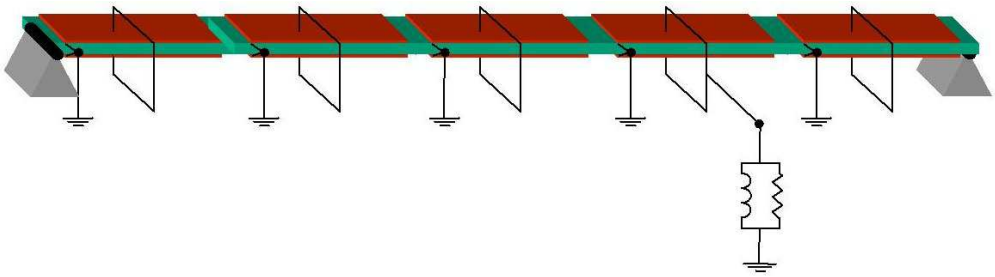

Figure 6.3: Configuration for the resonant shunted PZT experiment.

Inductor value	natural frequency	damping ratio
L=49.6H	34.1406, 38.5658	**0.0117**, 0.0284
L=55H(opt)	34.8402, 36.4853	0.0192, **0.0191**
L=68.9H	31.1746, 35.9474	0.0232, **0.0136**
cc	34.7414	**0.0102**

Table 6.1: Single shunted actuator: natural frequencies and damping ratios for R=0, L changes.

The other transducers have been short-circuited as in Figure 6.3. The first graph, Figure 6.4, is for a non-dissipative shunt, that is the transducers are shunted with an inductor only, for different values of the inductor, while for the second one, Figure 6.5, the inductor is fixed to the optimal tuning value, a resistor is inserted and the curves refer to different values of the resistor.

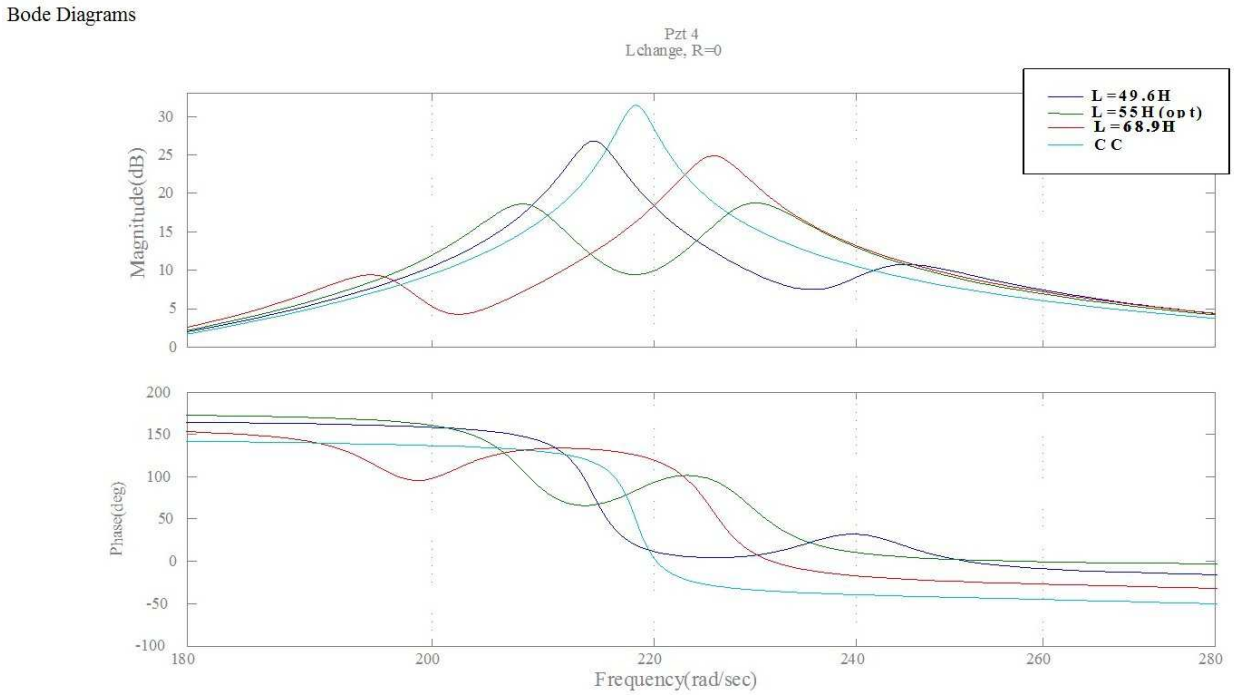

Figure 6.4: Single Shunted actuator FRF. R=0, L changes.

As we can see the insertion of the inductor produces a veering of the mechanical mode into two electromechanical ones. In Table 6.1 are reported the values of the natural frequency and the damping ratio for each of them for different values of the inductor. Now we have two electromechanical modes, each of them with its own natural frequency and damping ratio. Recalling that the damping ratio is related to the exponential decay of the response function in the time domain, we must consider as a performance parameter (in order to compare the

Resistor value	natural frequency	damping ratio
R=1K	34.7900	0.0087
R=50K	34.8936	0.0273
R=70K	34.7715	0.0312
R=100Kopt	34.8324	0.0399
R=300K	33.3496, 36.3660	0.0246, 0.0282
R$\rightarrow\infty$	34.8402, 36.4853	0.0192, 0.0191

Table 6.2: Single shunted actuator: natural frequencies and damping ratios for L=Lopt, R changes.

observed damping) the smaller of the two obtained in each case (for sufficiently long time, the mode related to the larger damping becomes negligible). Looking at Table 6.1, it can be seen that there is an optimal tuning parameter. As we change the tuning away from the optimal value, the damping ratio decreases rapidly.

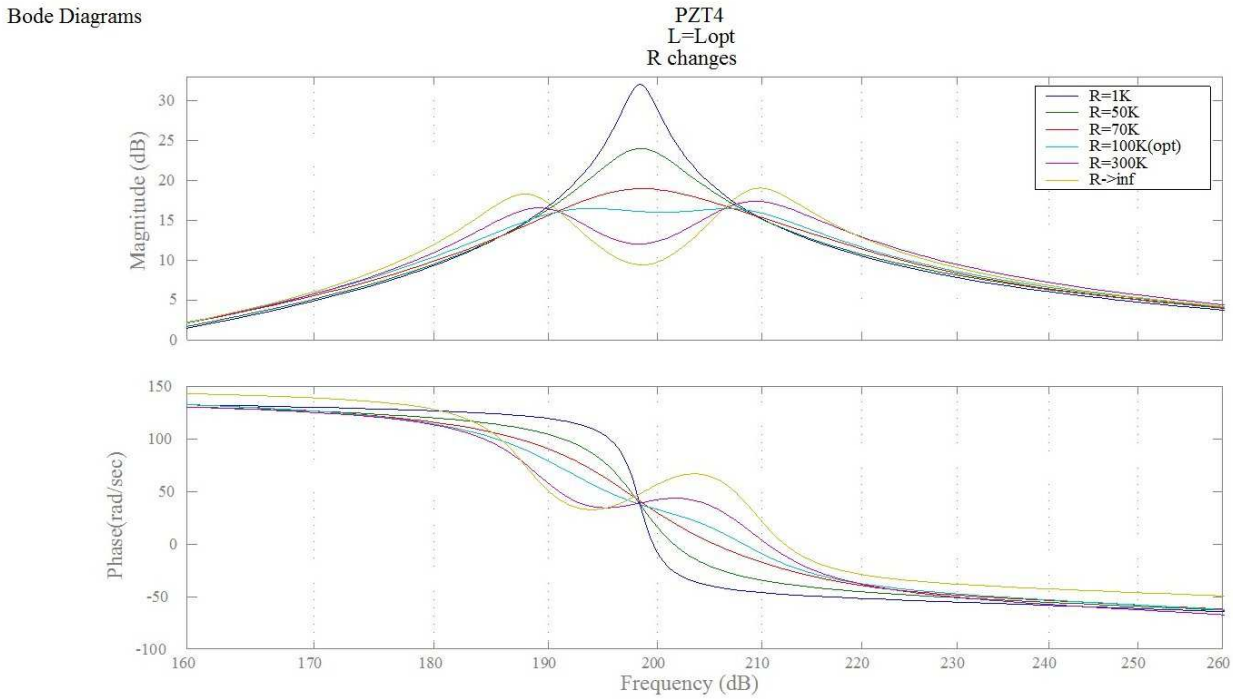

Figure 6.5: Single shunted FRF. L=Lopt, R changes.

Setting the inductor value to the optimal one and inserting a resistor in parallel, the two electromechanical modes approach each other and the maximum of the FRF modulus decreases, becoming at the optimal values flat over a region of 20 rad/s around resonance. What physically happens [25] is that the insertion of the resistor causes an uncoupling of the mechanical and the electrical systems (that is, the energy exchange becomes smaller), but

Inductor value	natural frequency	damping ratio
cc	34.7414	0.0102
L=41.3	34.3783, 42.1826	**0.0136**, 0.0332
L=49.6	33.5248, 39.3266	**0.0120**, 0.0292
L=56.2(opt)	32.5359, 38.0641	0.0194,**0.0192**
L=60.6	31.7881, 37.5419	0.0220,**0.0135**
L=68.9	30.2768, 36.9224	0.0241, **0.0172**

Table 6.3: Multi-shunted actuators: natural frequencies and damping ratios for R=0, L changes.

the energy dissipation increases, due to dissipation by the Joule effect provided by the resistor. If the resistor increases too much, the uncoupling becomes so high that, although that large resistor could dissipate more energy, the energy exchanged between the two systems is so small that the dissipated energy decreases. Setting the resistor to the optimal value, a relevant reduction of the forced response is obtained and the damping ratio is significantly increased (see Table 6.2). However, the reduction of the frequency response is achieved only for a narrow band centered on the resonance frequency. The issue of developing a broadband damping should be solved by the distributed coupling, as we hope to verify with future experiments.

6.2 Multi shunted actuators

The third set of measurements has been performed on a multi-shunted actuator system, Figure 6.6. The coupled mode is, as in the previous case, the first one. We now show the

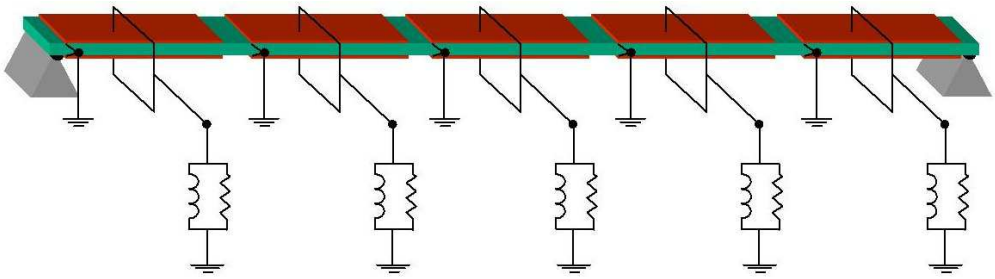

Figure 6.6: Configuration for the resonant multi-shunted PZT experiment.

frequency response functions obtained. In Figure 6.7, the resistor is for a non-dissipative shunt, that is, all transducers are shunted with an inductor only, for different values of the inductor, while in Figure 6.8, each inductor is fixed to the optimal value and a resistor is added in each shunt circuit. The curves refer to different values of the resistor.

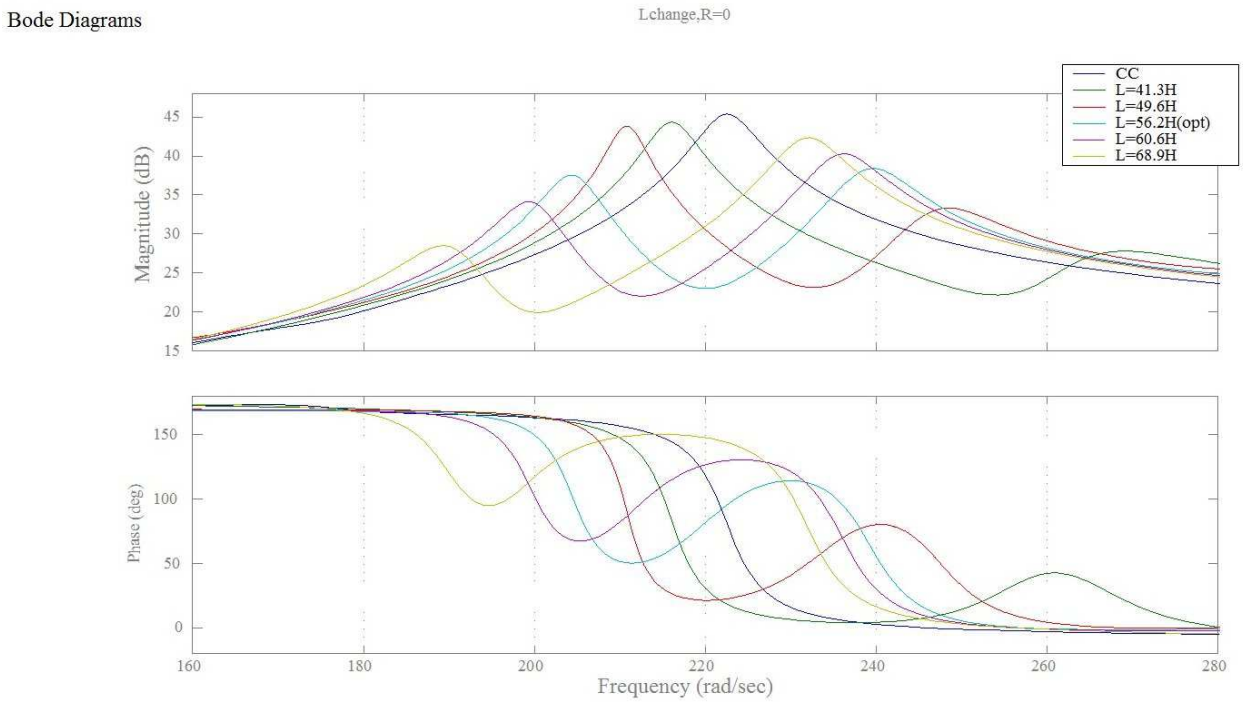

Figure 6.7: Multi-shunted FRF. R=0, L changes.

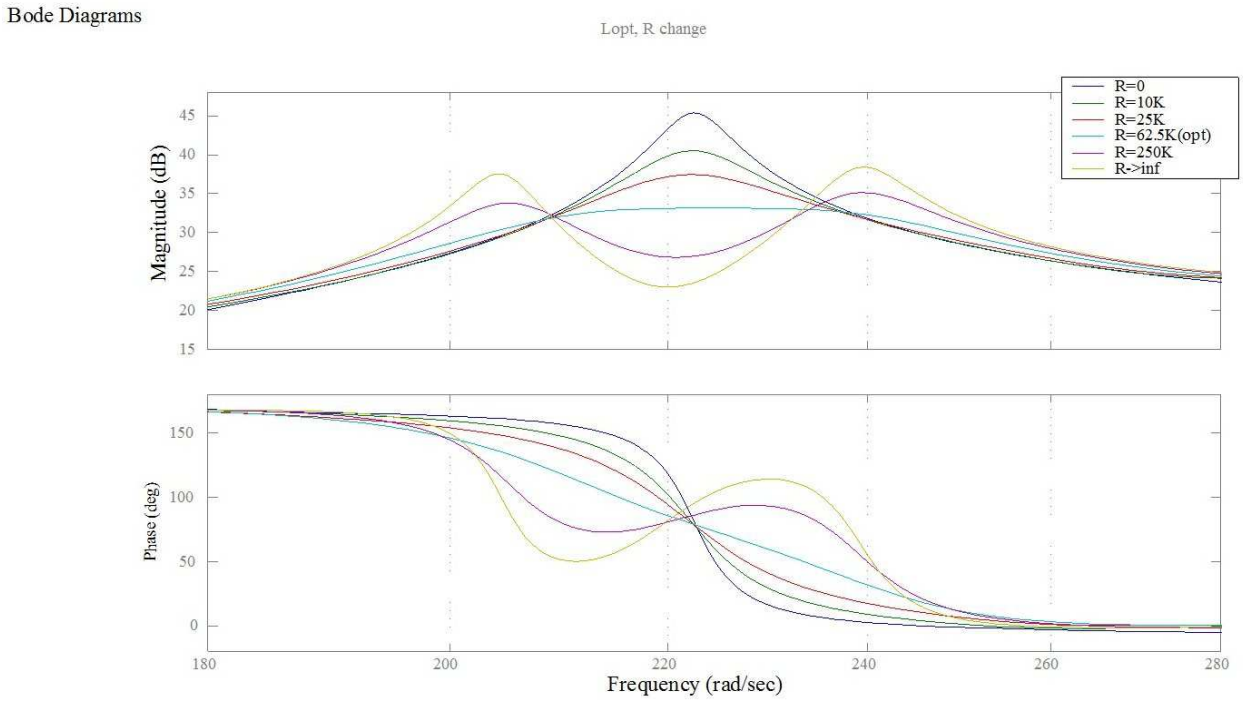

Figure 6.8: Multi-shunted FRF. L=Lopt, R changes.

Resistor value	Natural frequency	Damping ratio
cc	34.7414	0.0102
R=10kΩ	35.3625	**0.0257**
R=25kΩ	35.3483	**0.0397**
R=62.5kΩ(*opt*)	33.7127, 37.9251	0.0721, **0.0676**
R=250kΩ	32.7355, 37.9403	**0.0304**, 0.0312
R→∞	32.5359, 38.0641	0.0194, **0.0192**

Table 6.4: Multi-shunted actuators: natural frequencies and damping ratios for L=Lopt, R changes.

Patch	natural frequency	damping ratio
PZT1	34.7804, 35.9915	**0.0157**, 0.0181
PZT4	33.9013,37.0607	**0.0184**, 0.0193

Table 6.5: Natural frequencies and damping ratios of the system shunted with PZT1 and PZT4. R=0, Lopt.

The behavior of the system with respect to the electrical parameters is the same as in the previous case, but, as we can see in Table 6.4 the damping ratios are significantly increased. The maximum of the FRF decreases, with the insertion of an optimum LR shunting circuits, is about 15 dB, that is, the FRF of the shunted system is about thirty times smaller than that of the free system.

6.3 Comparisons

6.3.1 Single shunted: experimental comparison

The location of the piezoelectric patches is one of the most critical issues of both active and passive control techniques. In this section we compare results obtained with two different actuators (in particular PZT1 and PZT4). The first comparison, Figure 6.9, is made for a non-dissipative shunt of the two patches (that is, they are shunted by means of an inductor only), while the second one, Figure 6.10, is for a dissipative shunt (that is a resistor is applied in parallel with the inductor); in all these comparisons the electric parameters are fixed at the optimal value. As we can see (Tables 6.5 and 6.6) in both cases the 4 PZT patch is more efficient in damping the first mode. This result is feasible since patch one is nearer the first mode node than the patch four, so it is subjected to a lower deformation gradient that induces less energy exchange and so less damping (in the limit of a small actuator applied exactly at a node of the mode, the actuator would provide zero damping [1]).

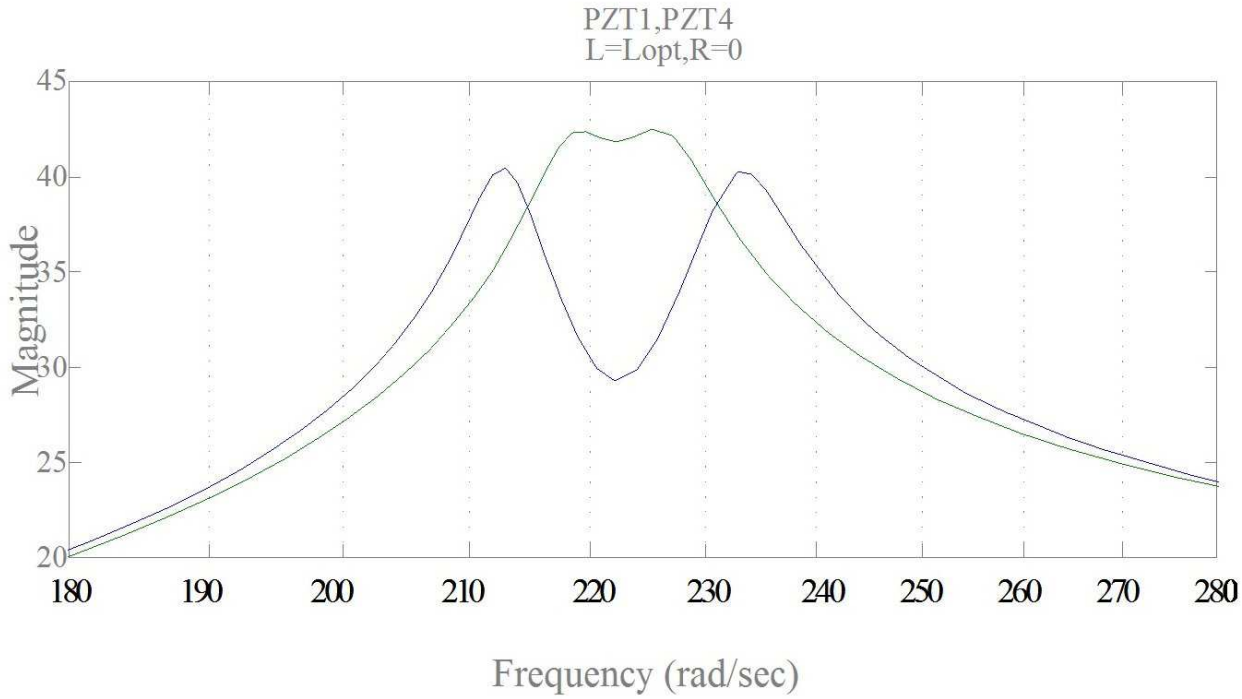

Figure 6.9: Comparison between the single shunted FRFs of PZT1 and PZT4. R=0, L=Lopt.

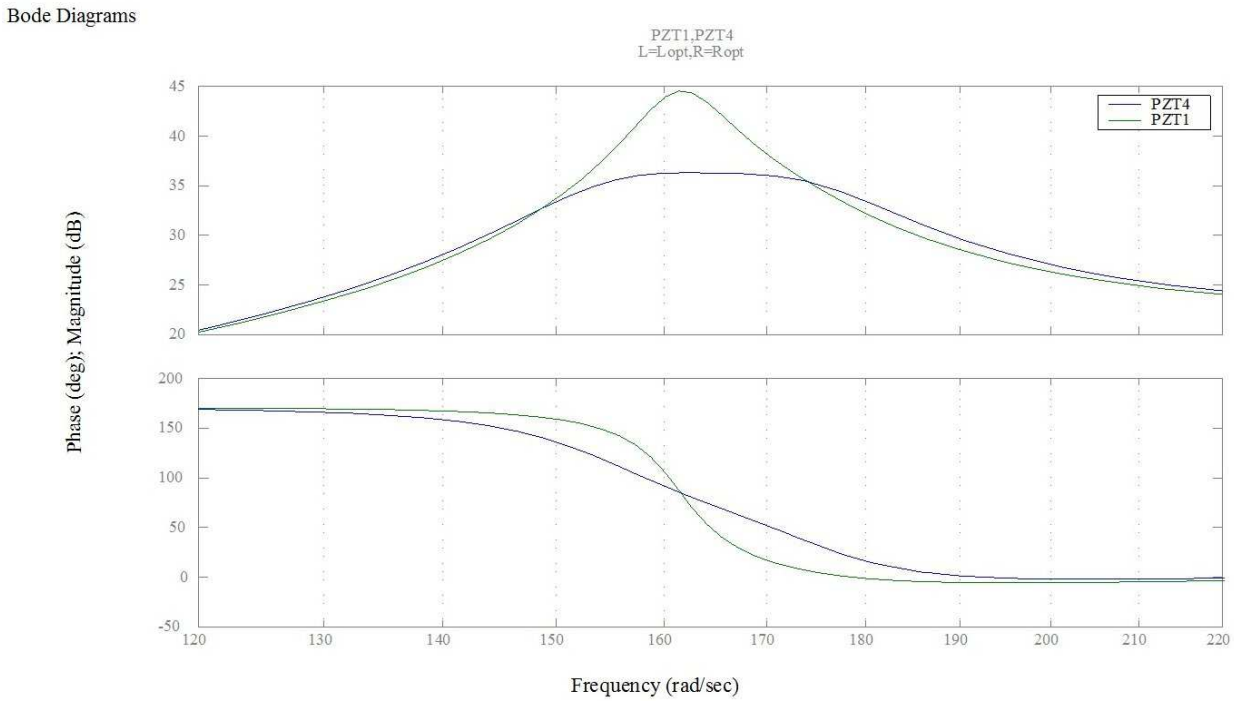

Figure 6.10: Comparison between the single shunted FRFs of PZT1 and PZT4. R=Ropt, L=Lopt.

Patch	natural frequency	damping ratio
PZT1	35.1067, 36.0875	**0.0194**, 0.0286
PZT4	34.3845, 37.2267	0.0513, **0.0505**

Table 6.6: Natural frequencies and damping ratios of the system shunted with PZT1 and PZT4. Ropt, Lopt.

6.3.2 Single-shunted/multi-shunted: experimental comparison

It is interesting to compare the shunting effect of a single actuator to that of the multi-shunted system in order to verify if increasing the number of the shunting actuators produces any advantage. We give now (Figure 6.11) a comparison between the single-shunted system (shunted with the actuator four only) and the multi-shunted system, each of them tuned to the optimal shunting configuration (RL shunt).

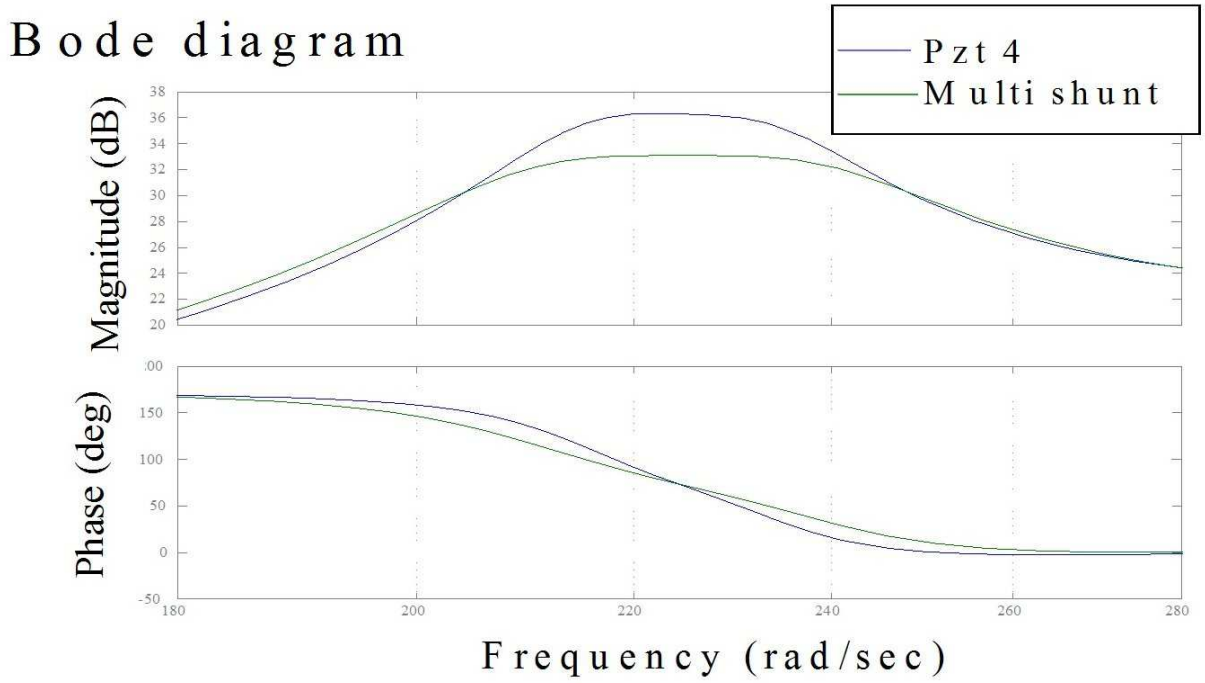

Figure 6.11: Comparison between single-shunted and multi-shunted FRFs. R=Ropt, L=Lopt.

As we can see in Figure 6.7, for a multi-shunted system, we obtain a damping ratio larger than the one obtained with one patch alone. The difference of the maximum value of the FRF in the two cases is 2dB, that is, the FRF of the multishunted system is 1.5 times smaller than that of the singleshunted one.

	natural frequency	damping ratio
Multi-shunt	33.7127, 37.9251	0.0721, **0.0676**
PZT4	34.3845, 37.2267	0.0513, **0.0505**

Table 6.7: Comparison between the natural frequencies and the damping ratios of the single shunted system (PZT4) and the multi-shunted system. R=Ropt, L=Lopt.

	Optimum inductor value	Optimum resistor value
Numerical	70.96H	62.5kΩ
Experimental	56.2H	62.5kΩ

Table 6.8: Comparison between the numerical and the experimental optimal tuning electric parameters.

6.3.3 Multi-shunted system: numerical and experimental comparisons

Here (Table 6.8) we compare results obtained with the numerical code with those from the experimental investigation, for the multishunted system.

The value of the optimal tuning inductance obtained by the numerical simulation is found to be larger than the experimental one. Since the optimum inductor value is related [12] to the natural frequency and to the PZT capacitance by

$$L = \frac{1}{\omega^2 C},$$

and there is a good agreement between the experimental and the numerical natural frequencies, probably the reason for this difference is related to the value of the PZT patches capacitance. The numerical code values, in fact, are based on the PZT data sheet, while a more accurate simulation could be performed if the actual values would be provided by direct measurements made on the patches. In any case, the optimal resistor values have an excellent agreement. In Figure 6.12, the experimental and the numerical FRF are compared. The values of the electric elements are those in Table 6.8.

As we can see in Table 6.9, once the optimal electrical tuning parameter has been fixed the numerical code shows a good agreement with the experimental data. In particular, the

	natural frequency	damping ratio
Experimental	33.7127, 37.9251	0.0721, **0.0676**
Numerical	33.855, 39.0966	**0.069272**, 0.0799693

Table 6.9: Comparison between the numerical and the experimental natural frequencies and damping ratios.

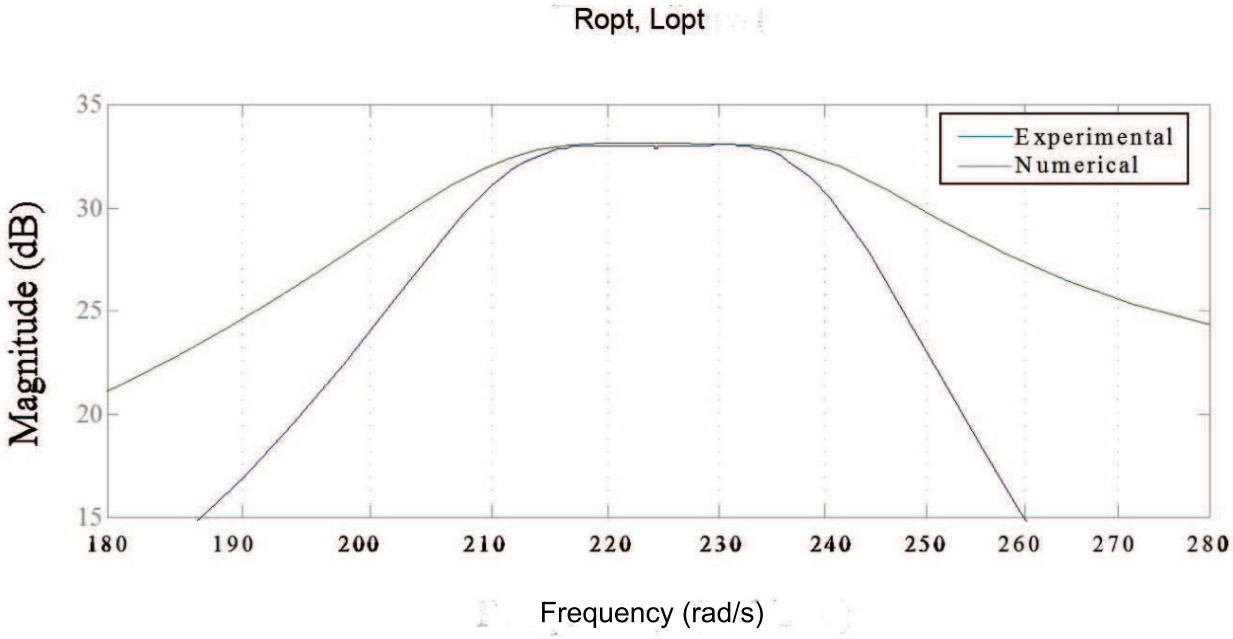

Figure 6.12: Multi-shunted system: numerical and experimental comparison.

errors in both the natural frequency and the damping ratio are around three percent of the experimental values.

Chapter 7

Conclusions and further development

In this thesis a numerical model to study the behavior of a piezoelectromechanical beam for vibration damping has been developed. The system has been designed, constructed and experimentally investigated by a standard modal testing analysis to obtain the FRF for different system configurations. In particular, the behavior with respect to the electrical shunting parameters has been studied. Moreover, the FRF obtained by shunting different patches has been compared in order to verify the importance of patch positioning, and the FRF for a single shunted and a multi shunted system have been compared in order to point out if and how increasing the number of the patches aids in the damping of the system. The numerical and experimental results have been compared in order to validate the numerical code. They show, except for the value of the optimal shunting inductor, a good agreement. The entire experimental system has been designed and constructed in order to be easily used in further experiments by this research group, whose final goal is to validate the viability of the wide frequency range distributed coupling technique [12].

The future experiments should deal with the following systems:

1. A beam coupled with the lumped version of an electric transmission line with line resistances and inductances

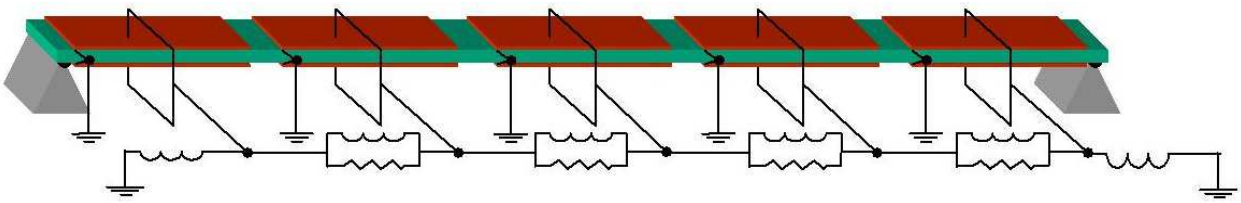

Figure 7.1: Piezoelectromechanical beam: transmission line configuration.

2. A beam coupled with the lumped version of an electric transmission line with line inductances and ground resistances

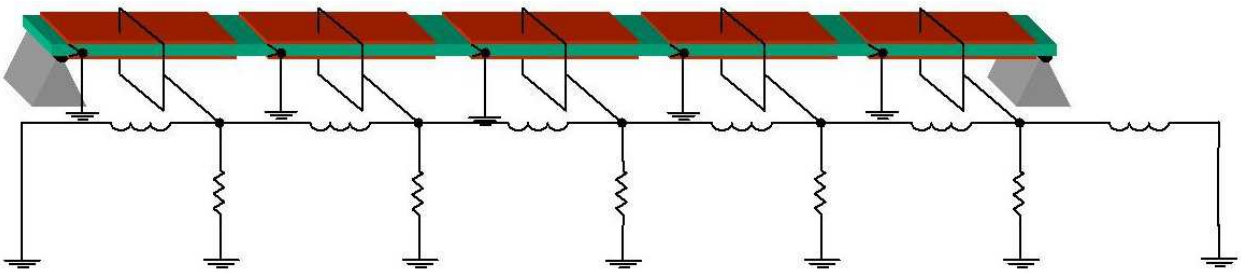

Figure 7.2: Piezoelectromechanical beam: transmission line with line configuration inductances and ground resistances.

Their performances in the suppression of mechanical vibrations should be investigated as a function of the values of the electrical parameters to validate the theoretical results obtained in [12].

Bibliography

[1] D. K. Miu, "*Physical interpretation of transfer function zeros for simple control systems with mechanical flexibilities*", Journal of Dynamic Systems, Measuraments, and Control, september 1991, Vol113/419.

[2] Rogers, C.A., 1993, *"Intelligent Material Systems: The Dawn of a New Materials Age"*, Journal of Inteligent Material Systems and Structures, Vol. 4, No. 1, pp. 4-14.

[3] Rogers, C.A., 1990 *"Active Vibration and Structural Acoustic Control of Shape Memory Alloy Hybrid Composites: Experimental Results"*, Proceedings of International Congress on Recent Developments in Air- and Structure-Borne Sound and Vibration, Auburn University, March 6-8, 1990; pp. 695-708.

[4] Baley, T. and J.E. Hubbard, Jr., 1985, *"Distributed Piezoelectric-Polymer Active Vibration Control of a Cantilever Beam"*, Journal of Guidance, Control and Dynamics, Vol 8, No. 5; pp. 605-611.

[5] Zhou, S.W., 1991, *"Active Magnetostrictive Mounts for Base Vibration Isolation Systems"*, Research Report, Center for Intelligent Material Systems an Structures, Virginia Polytechnic Institute and State University, January 3, 1991; pp. 1-25.

[6] Garcia, E. and D. Inman, 1990, *"Advantages of Slewing an Active Structure"*, Journal of Intelligent Material Systems and Structures, Vol. 1, No. 3; pp. 261-272.

[7] Chaudhry, Z. and Rogers, C.A., 1991, *"Bending and Shape Control of Beams Using SMA Actuators"*, Journal of Intelligent Material Systems and Structures, Vol. 2, No. 4; pp. 581-602.

[8] Hickman, G.A., Gerardi, J.J., and Feng, Y., 1990, *" Application of Smart Structures to Aircraft Health Monitoring"*, Proceedings of First Joint U.S./Japan Conference on Adaptive Structures, Maui, Hawaii, March 19-23; pp. 966-984.

[9] Zhou, S.W., C. Liang, and C. A. Rogers, 1993, *"An In-Situ Sensory Technique for In-Service Monitoring-Measurement of the Complex Young's Modulus of Polymers"*, Proceedings of Smart Sensing, Processing, and Instrumentation, SPIE, Albuquerque, NM, February 1-4, 1993, Vol. 1918; pp. 14-23.

[10] Sun, F. P., C. Liang and C.A. Rogers, 1994, *"Modal Analysis Using Collocated PZT Actuator/Sensor-An Electromechanical Approach"*, Proceedings of Smart Structures and Intelligent Systems, SPIE, Orlando, FL, February 13-18, 1994.

[11] F.dell'Isola, S.Vidoli, "*Continuum Modeling of Electro-mechanical Truss Beams"*, Archive Applied Mechanics 68 (1998)

[12] F.dell'Isola, S.Vidoli, "*Bending-Waves Damping in Truss Beams by Electrical Transmission Line with PZT Actuators"*, Archive Applied Mechanics 68 (1998)

[13] S.Vidoli, F.dell'Isola, *"Modal Coupling in One-Dimensional Electro-Mechanical Structured Continua"*, Acta Mechanica 141, 1-2 (2000)

[14] V.Steffen Jr. and D.J.Inman, *"Optimal design of a Piezoelectric Material for vibration damping in Mechanical Systems"*, Journal of Intelligent Material Systems and Structures, Vol. 10-December 1999

[15] V.Steffen Jr, D.A. Rade, D.J.Inman," Using Passive Techniques for Vibration Damping in Mechanical Systems", Journal of Braz. So. Mechanical Sciences, Vol XXII, No 3,pp. 411-421, 2000

[16] J.J.Hollkamp, *"Multimodal Passive Vibration Suppression with Piezoelectric Materials and Resonant Shunts"*, Journal of Intelligent Material Systems and Structures, Vol. 5-March 1994.

[17] Hagood W. and A. von Flotow, *"Damping of Structural Vibrations with Piezoelectric Materials and Passive Electrical Networks"*, Journal of Sound and Vibrations, 146(2):243-268, 1991.

[18] George A. Lesieutre, *"Vibration Damping and Control Using Shunted Piezoelectric Materials"*, The Shock and Vibrations Digest, Vol. 30, No.3, May 1998, 187-195

[19] R.Senani, "*Alternative Modification of the Classical GIC Structure"*, Electronics Letters, 18th July 1996 Vol.32 No.15

[20] D.J.Ewins, "*Modal Testing: Theory and Practice"*, Research Studies Press LTD., England, 1986

[21] A.Sestieri, "*Dispense del corso di Meccanica delle Vibrazioni"*, 1998

[22] Mario Bye," *Circuiti Rc Attivi: Teoria" e Progetto*,1986

[23] Kaehwan Kim,Yeon-Ho Ryu and Seung-Bok Choi, *"New Shunting Parameter Tuning Method for Piezoelectric Damping Based on Measured Electrical Impedence",* Smart Structures and System Laboratory, Department of Mechanical Engineering, Inha University, Incheon 402-751, South Corea.

[24] Leonard T. Bruton,*"RC-ACTIVE CIRCUITS, Theory and Design"*,Prentice-Hall, Inc., Englewood Cliffs, New Jearsey 07632

[25] S.Vidoli and F. dell'Isola, *"Vibrational control in plates by uniformly distribuited actuators interconnected via electric network"*, European Journal of Mechanics A/Solids, 20, 435-456, (2001)